ISSN 0234-5366

# КРАТКИЕ СООБЩЕНИЯ ОИЯИ

# JINR RAPID COMMUNICATIONS

6[74]-95



Издательский отдел ОИЯИ ДУБНА

JINR Publishing Department DUBNA

Объединенный институт ядерных исследований
Joint Institute for Nuclear Research

6[74]-95

# КРАТКИЕ СООБЩЕНИЯ ОИЯИ

# JINR RAPID COMMUNICATIONS

Дубна 1995

В журнале *«Краткие сообщения ОИЯИ»* публикуются статьи, содержащие оригинальные результаты теоретических, экспериментальных, научно-технических, методических и прикладных исследований. Содержание публикуемых статей определяется тематикой научных исследований в ОИЯИ: теоретическая физика, физика элементарных частиц, релятивистская ядерная физика, физика тяжелых ионов, ядерная физика низких и промежуточных энергий, нейтронная ядерная физика, физика конденсированных сред, радиационная биология и медицина, экспериментальные методы и установки, а также прикладные исследования.

Журнал зарегистрирован в Комитете Российской Федерации по печати, издателем журнала является Объединенный институт ядерных исследований.

Журнал выходит шесть раз в год.

The journal *JINR Rapid Communications* publishes the articles providing information on original results of theoretical, experimental, scientific-technical, methodical and applied investigations. Subject-matter of articles covers the principal fields of research at JINR: theoretical physics, elementary particle physics, relativistic nuclear physics, heavy ion physics, low- and intermediate-energy physics, neutron nuclear physics, condensed matter physics, radiation biology and medicine, experimental instruments and methods and applied research.

The journal is registered in the Committee of the Russian Federation for Press and is published bimonthly by the Joint Institute for Nuclear Research.

References to the articles of the *JINR Rapid Communications* should contain:

— names and initials of authors,
— title of journal, introduced by word "In:",
— year of publication,
— publication index,
— page number.

For example:
Batyunya B.V., Zinchenko A.I. — JINR Rapid Communications, 1995, No.3[71]-95, p.5.

## ОГЛАВЛЕНИЕ
## CONTENTS

УДК 539.17

# ON THE POSSIBILITY OF FUSION REACTIONS IN WATER MOLECULES

*V.B.Belyaev, A.K.Motovilov, W.Sandhas*

The probability of nuclear transitions $p+p+{}^{16}\mathrm{O} \to {}^{18}\mathrm{Ne}\,(4.522,1^-)$ in molecular water is estimated. Due to a practically exact agreement of the energy of the Ne resonance and of the $p+p+{}^{16}\mathrm{O}$ threshold, the transition probability is found to be considerably enhanced. This indicates the possibility of nuclear fusion in rotationally excited $H_2O$ molecules of angular momentum $1^-$.

The investigation has been performed at the Bogoliubov Laboratory of Theoretical Physics, JINR, and Physikalisches Institut, Universität Bonn (Germany).

## О возможности реакций синтеза в молекулах воды

*В.Б.Беляев, А.К.Мотовилов, В.Зандхас*

Оценивается вероятность ядерных переходов $p+p+{}^{16}\mathrm{O} \to {}^{18}\mathrm{Ne}\,(4.522,1^-)$ в молекуле воды. Устанавливается существенное увеличение вероятности таких переходов благодаря практически точному совпадению энергии резонанса Ne и порога $p+p+{}^{16}\mathrm{O}$. Все это указывает на возможность реакции ядерного синтеза во вращательно возбужденных молекулах $H_2O$ с угловым моментом $1^-$.

Работа выполнена в Лаборатории теоретической физики им. Н.Н.Боголюбова ОИЯИ и Физическом институте Боннского университета (Германия).

Nuclear states with binding or resonance energies close to breakup threshold have a large spatial extension due to a long tail of the corresponding wave functions. For instance, the ground state of the nucleus ${}^8\mathrm{B}$, i.e., of the main source of high-energy solar neutrino [1], is separated from the $p+{}^7\mathrm{Be}$ threshold by only 130 keV. Integrations up to 300 fm, hence, are needed [2] when treating the process $p+{}^7\mathrm{Be} \to {}^8\mathrm{B}+\gamma$.

In nuclear reactions, the existence of near-threshold intermediate states leads to a considerable increase of the transition probability. As an example we recall the muon-catalyzed $dt$ fusion in the molecule $(dt\mu)$, which takes place primarily via the mechanism

$$d+t \to {}^5\mathrm{He}\,(3/2^+) \to {}^4\mathrm{He}+n.$$

Since the difference between the energies of the $dt$ threshold and the ${}^5\mathrm{He}\,(3/2^+)$ resonance is only about 50 keV, it is not surprising that the probability of this process exceeds at least by four orders of magnitude the probability of nuclear transitions in the $(dd\mu)$ or $(pd\mu)$ molecules where no such resonances occur [3].

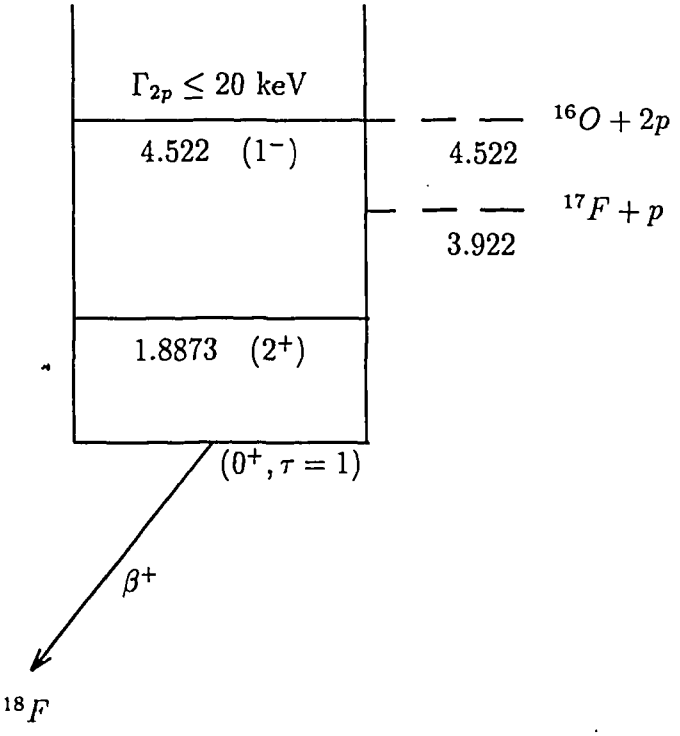


Fragment of the nucleus $^{18}$Ne spectrum

In this note we want to point to an analogous situation, however in an ordinary (electronic) molecule. From the level scheme of the nucleus $^{18}$Ne [4,5] presented in the Figure, we infer that the measured energy $E = 4.522$ MeV of $^{18}$Ne $(1^-)$ coincides up to the last figure with the threshold energy of the three-body channel $p + p + {}^{16}$O. Since the binding energy of the water molecule is only a few eV, this means that the rotational $1^-$ state of $H_2O$ and the $^{18}$Ne $(1^-)$ state are degenerate in energy. Excited molecular water of this angular momentum, thus, is to be considered as a superposition of these pure molecular and nuclear states. In other words, the wave function of real water molecules in the $1^-$ state contains always an admixture of the $^{18}$Ne $(1^-)$ nuclear wave function.

The mixing coefficient of this superposition, and thus the nuclear transition probability in the $H_2O$ molecule, is given by the overlap integral between the «pure» states. Due to the proximity of the resonance and threshold energies, intermediate and large distances (in nuclear scale) contribute considerably to this integral. As a consequence, the nuclear transition probability is enhanced, instead of being suppressed by the usual Coulomb barrier factor [6].

The estimate on which this statement rests is based on the following ansatz for the wave function of the water molecule,

$$\psi_{\rm mol}(X) = \frac{1}{N_{\rm mol}} \frac{F_{5/2}(\eta_0, \kappa\rho)}{\rho^{5/2}} e^{-\kappa\rho} Y_{l\lambda}^{lM}(\hat{x}, \hat{y}). \quad (1)$$

Here we use, instead of the Jacobi variables $\{\vec{x}, \vec{y}\}$ of the $p+p+{}^{16}$O system, the set of hyperspherical variables $X = \{\rho, \omega, \hat{x}, \hat{y}\}$, with $\rho = \sqrt{x^2 + y^2}$ being the hyperradius; and $\omega = \arctan y/x$, the hyperangle. For the five angles in $X$, the notation $\Omega = \{\omega, \hat{x}, \hat{y}\}$ will be used, and the Coulombic potential of our problem is written in the form $V(X) = \mathcal{V}(\Omega)/\rho$. By $F_\nu$ the regular solutions of the hyperradial Schrödinger equation are denoted; and by $Y_{l\lambda}^{JM}(\hat{x}, \hat{y})$, the eigenfunctions of the total angular momentum operator. $N_{\rm mol}$ is a normalization factor, and $\kappa \sim \sqrt{|\varepsilon_{\rm mol}|}$ represents the momentum corresponding to the binding energy $\varepsilon_{\rm mol}$ of the $H_2O$ molecule; $\eta_0 = \mathcal{V}_0/2\kappa$ is a kind of Sommerfeld parameter, where $\mathcal{V}_0$ is obtained by averaging $\mathcal{V}(\Omega)$ with the angular part of $\psi_{\rm mol}(X)$. The ansatz (1) takes correctly into account the Coulomb repuslion between the particles at small distances, as well as the geometric size of the water molecule.

For the description of the ${}^{18}$Ne nuclear resonance state ($1^-$), we use the asymptotic form of the Coulombic three-body break-up function normalized to the nuclear volume,

$$\psi_{\rm res}(X) = \frac{1}{N_{\rm res}} \frac{f^J(\rho, \omega)}{\rho^{5/2}} Y_{l\lambda}^{lM}(\hat{x}, \hat{y}), \quad (2)$$

where

$$f^J(\rho, \omega) = \int d\hat{x}\, d\hat{y} \exp\left\{ iK\rho - i\frac{\mathcal{V}(\Omega)}{2K} \ln(2K\rho) \right\} Y_{l\lambda}^{JM}(\hat{x}, \hat{y}). \quad (3)$$

Here, $K \sim \sqrt{E}$ is the momentum corresponding to the energy $E$ of the outgoing particles $^{16}O + p + p$.

Within the models (1) and (2) we find for the overlap integral the asymptotic estimate

$$I \sim \exp\left\{ -\frac{\pi}{2}\eta_K^0 \right\} \exp\{ i\eta_K^0 S \}, \quad (4)$$

where $\eta_K^0 = \mathcal{V}_{\rm min}/2K$ is another kind of Sommerfeld parameter, with $\mathcal{V}_{\rm min}$ being the minimal value of the angular part $\mathcal{V}(\Omega)$ of the total Coulomb potential. The phase $S$ depends on $\mathcal{V}_{\rm min}$ and a parameter $\xi = K/\kappa$. From its definition follows that $\xi$ can vary between $0 \le \xi \le \sqrt{\Gamma_{2p}/|\varepsilon_{\rm mol}|}$ with $\Gamma_{2p}$ being the width of the ${}^{18}$Ne ($1^-$) level for the decay into the $p+p+{}^{16}$O channel. When studying $S$ as a function of $\xi$ it turns out that there exists a wide subdomain of values of $\xi$ in which $S < 0$ and $|\operatorname{Im} S| > \frac{\pi}{2}$. That is, the overlap integral (4), and thus the transition rate

$$W = \kappa c |I|^2 \tag{5}$$

of the process $H_2O \to {}^{18}Ne\,(1^-)$, increase exponentially with decreasing $K$ (at small energies $E \sim K^2$). This is to be contrasted with the usual opposite behaviour of transitions into short-ranged (non-resonant) nuclear states.

The above estimates imply that molecular water in the $1^-$ state has a non-vanishing probability to go over into the excited state ${}^{18}Ne\,(1^-)$, which then will decay either into the channel ${}^{17}F + p + Q_1$ ($Q_1 \cong 0.6$ MeV) or into the chain ${}^{18}Ne\,(1^-) \to {}^{18}Ne + \gamma + Q_2 \to$ $\to {}^{18}F + e^+ + \nu$ ($Q_2 \cong 4.522$ MeV). Unfortunately, the partial widths of these two transitions are unknown and, therefore, it is impossible by now to estimate the whole energy release in the considered process of «burning» molecular water.

This work was partly supported by the Scientific Division of NATO, grant No.930102. Two of the authors (V.B.B. and A.K.M.) are grateful for financial support to the International Science Foundation and Russian Government, grant No.FRB300.

## References

1. Bahcall J.N., Ulrich R. — Rev. Modern. Phys., 1988, 60, p.297.
2. Kim K.H., Park M.H., Kim B.T. — Phys. Rev. C, 1987, 35, p.363.
3. Breunlich W.H., Kammel P., Cohen J.S., Leon M. — Ann. Rev. Nucl. Part. Sci., 1989, 39, p.311.
   Bogdanova L.N., Markushin V.E. — Muon Catalyzed Fusion., 1990/1991, 5/6. p.189.
   Hale G.M. — Ibid., p.227.
   Szalevicz K., Jeziorski J.H. — Ibid., p.241.
4. Nero A.V., Adelberger E.G., Dietrich F.S. — Phys. Rev. C, 1981, 24, p.1864.
5. Ajzenberg-Selove F., Lauritsen T. — Nucl. Phys. A, 1988, 490, p.1.
6. Wu T.-Y., Ohmura T. — Quantum Theory of Scattering. N.Y.: Prentice-Hall, 1962.
7. Peterkop R.K. — ZhETP, 1962, 43, p.616 (Russian).

Received on December 8, 1995.

УДК 539.12.01 + 539.12...162.8

# AN ANALYSIS OF PION SPECTRA OF THE CHARGE-EXCHANGE REACTION Mg ($t$, $^3$He)

*F.A.Gareev, K.A.Gridnev[1], A.G.Semtchenkov[1], A.V.Pozdniakov[2], Yu.L.Ratis[3]*

We have studied the charge-exchange reaction Mg ($t$, $^3$He) by using the $\pi$–$\rho$–$g'$-model and formalism of effective number. Attempts have been made to find information about the value of the ($NN$ – $N\Delta$)-interaction renormalization in going from vacuum to nuclei. We obtained a good qualitative description of the position of the Δ-peak of the theoretical pion full-energy spectrum by changing the attributes of the nucleon-nucleon interaction in going from vacuum values of effective masses of nucleons, mesons and Δ-isobar to nuclei.

The investigation has been performed at the Bogoliubov Laboratory of Theoretical Physics, JINR.

## Анализ спектров пионов реакции перезарядки Mg ($t$, $^3$He)

*Ф.А.Гареев и др.*

Реакция перезарядки Mg ($t$, $^3$He) изучалась в рамках $\pi$–$\rho$–$g'$-модели и формализма эффективных чисел. Была сделана попытка получить информацию о величине перенормировки ($NN$ – $N\Delta$)-взаимодействия при переходе от вакуума к ядерной материи. Введением фактора изменения эффективных масс нуклонов, мезонов и Δ-изобары при переходе от вакуума к ядру получено хорошее качественное описание положения пика теоретического спектра полной энергии мезонов.

Работа выполнена в Лаборатории теоретической физики им. Н.Н.Боголюбова ОИЯИ.

Interest in the study of the charge-exchange reactions with the Δ-isobar excitation is connected with attempts to find information about the value of the ($NN$ – $N\Delta$)-interaction renormalization in going from vacuum to nuclei. The experimental data analysed and presented in the review [1] show the differences in masses and widths of the Δ-isobars in vacuum and nuclei. The calculations in the framework of the well-known Nambu — Jona–Lasinio model [2] and the model of constituent quarks [3] have qualitatively the same results.

The models predict reduction of meson and nucleon masses in the nuclear matter. We assume that surpluses of quark-quark interactions in the Δ-isobar satisfy the same equations

[1]Institute of Physics of St. Petersburg State University, Russia
[2]Radium V.G.Khlopin Institute, St. Petersburg, Russia
[3]Samara State Aerospace University, Russia

$$\lambda = \frac{M^*}{M} = \frac{M_\rho^*}{M_\rho} = \frac{M_\omega^*}{M_\omega} = \frac{M_\Delta^*}{M_\Delta},$$

where $M^*$ and $M$ are masses of nucleons, mesons and Δ-isobars in the nuclear matter and vacuum, respectively.

In this note, we try to qualitatively describe pion spectra of the charge-exchange reaction Mg ($t$, $^3$He) on the assumption of the influence of the nuclear matter. The π- and ρ-meson diagrams were taken into account. The experimental data have been obtained in the GIBS experiment [4] at the beam momentum 9.15 GeV/c and angle 0°.

We use the manner [5,6] that is based on the π–ρ–$g'$-model and the formalism of effective numbers. The inclusive cross section of the charge-exchange reaction on nuclei is

$$\frac{d\sigma[^{24}\mathrm{Mg}\ (t, {}^3\mathrm{He})_\Delta, X]}{d\Omega\, dE} = 3 * N_{\mathrm{eff}}^* F(t) * \frac{d\sigma(n + n \to p + \Delta^-)}{d\Omega\, dE}\Big|_{\mathrm{free}},$$

where $\frac{d\sigma(n + n \to p + \Delta^-)}{d\Omega\, dE}\Big|_{\mathrm{free}}$ is the cross section of the elementary process on the free nucleon, and $F(t)$ is the form factor.

Calculations have been done for the ($1\pi^-$, $0p$)-topology when only $\pi^-$-mesons were among the products of the reaction. The unperiphery's degree of the process (the influence

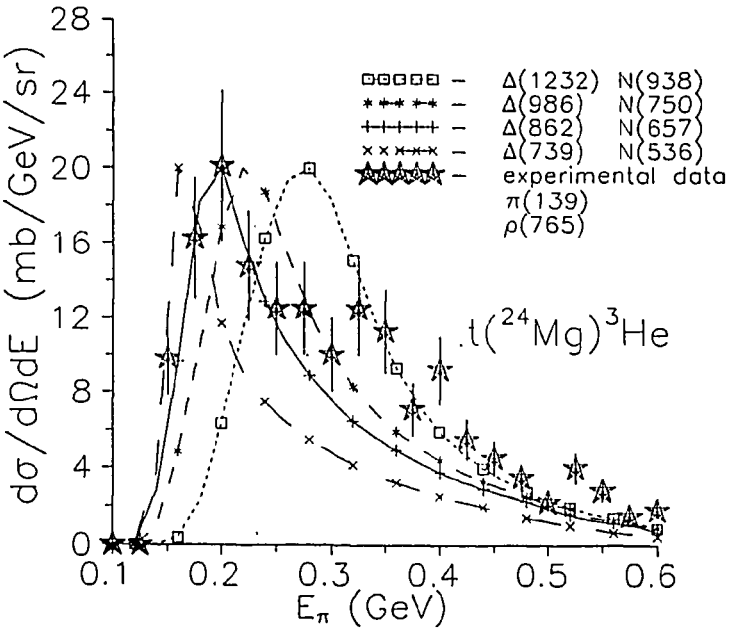


Fig.1. Theoretical spectra of full energy of pions in the topology ($1\pi^-$, $0p$) at different values of the effective masses of the nucleon and Δ-isobar normalized to the maximum of the experimental spectrum

of the nuclear matter) was taken into account by the λ(ρ)-parameter. This parameter describes reducing the effective mass of the nucleons, ρ-mesons and Δ-isobars inside nuclei:

$$\lambda(\rho) = \frac{M^*}{M} = \frac{M_\rho^*}{M_\rho} = \frac{M_\Delta^*}{M_\Delta}.$$

We have calculated the energy spectra of pions with the set of values of λ(ρ): 1, 0.9, 0.8, 0.7, 0.6.

The main results of calculations are shown in Figs.1 and 2.

Figure 1 shows the data of theoretical and experimental energy spectra of pions for the ($1\pi^-$, $0p$)-topology. We did not change the ρ-meson mass in these calculations. It has a vacuum value. All theoretical spectra were normalized to the maximum of the experimental spectrum. The analysis of spectra shows that the experimental spectrum has the peak at 200 MeV. The theoretical spectrum using the vacuum effective mass of the nucleon, ρ-meson and Δ-isobar has the peak at 300 MeV. We used the parameter λ reducing the effective masses of the nucleon, ρ-meson and Δ-isobar thus shifting the theoretical peak towards zero. The theoretical and experimental spectra have the same position of the peaks when the parameter is equal to $\lambda = 0.7$. This fact means that the effective masses of the nucleons and Δ-isobar in the nuclear matter can be estimated as: $M^* = 0.7M$ and $M_\Delta^* = 0.7M_\Delta$. The results of our calculations agree with the data in [2,3].

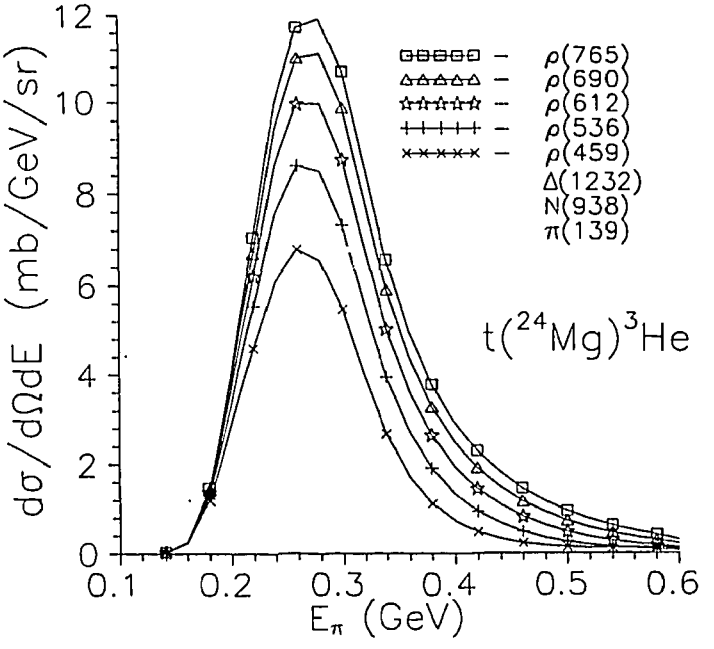


Fig.2. Theoretical spectra of full energy of pions in the topology ($1\pi^-$, $0p$) at different values of the effective masses of the ρ-meson

We also studied the influence of the effective mass of the ρ-meson on the energy spectra of mesons in the ($1\pi^-$, $0p$)-topology (Fig.2). The calculations show that the reducing of the effective mass of the ρ-meson from vacuum value to nuclear matter value by using factor $\lambda(\rho)$ results in contraction and some shift of the peaks towards lower energies. In all the calculations the vacuum value of the π-meson $M_\pi$ = 139 MeV has been used.

So, we obtained a good quality description of the position of the Δ-peaks of the theoretical pion full-energy spectrum by reducing the attributes of the nucleon-nucleon interaction in going from the vacuum effective mass values of nucleons, mesons and Δ-isobar to the nuclear values. This was predicated in the chiral theories.

This work was supported by Grant of the Foundation for Fundamental Research, St. Petersburg.

References

1. Strokovsky E.A., Gareev F.A., Ratis Yu.L. — Phys. Part. Nucl., 1993, 24(3), p.255.
2. Bernard V., Meissner U.-G. — Nucl. Phys., 1988, A489, p.647.
3. Brown G.E. — Nucl. Phys., 1988, A488, p.689.
4. Avramenko S.A. et al. — Relativistic Nuclear Physics & Quantum Chromodynamics, World Science, 1994, p.553.
5. Gareev F.A. et al. — Yad. Phys., 1994, 57, p.1411; Proc. Telluride Int. Conf. on «Spin and Isospin in Nuclear Interactions», 14—17 Mar., 1991, Telluride, Colorado/Ed. by Wissnik S.W., Goodman C.D., Walker G.E., N.Y.; L.: Plenum, 1991, p.445.
6. Gareev F.A., Strokovsky E.A., Ratis Yu.L. — Physics of Elementary Particles and Nuclei, 1994, 25, p.855.

Received on November 13, 1995.

УДК 539.12.01

# SIMULATION OF $e^+e^-$ PAIR PRODUCTION AND DETECTION IN THE ALICE EXPERIMENT

*B.V.Batyunya, N.V.Slavin*

Simulation of $e^+e^-$ pair production in PbPb interactions at LHC energy and of registration in the ALICE detector has been done. An influence of external $\gamma$-conversions on $e^+e^-$ combinatorial background is studied. Some details for selection cuts to improve the signal-to-background ratio are considered.

The investigation has been performed at the Laboratory of High Energies, JINR.

# Моделирование рождения и детектирования $e^+e^-$-пар в эксперименте ALICE

*Б.В.Батюня, Н.В.Славин*

Проведено моделирование рождения $e^+e^-$-пар в PbPb-взаимодействиях при энергии LHC и регистрации их в детекторе установки ALICE. Изучено влияние внешней гамма-конверсии на $e^+e^-$ комбинаторный фон. Рассмотрены некоторые детали выбора критериев, улучшающих отношение сигнал-фон.

Работа выполнена в Лаборатории высоких энергий ОИЯИ.

## 1. Introduction

The important role of leptonic pair investigations in heavy ion collisions is discussed elsewhere. This possibility was considered also for the ALICE experiment and special Monte Carlo study has been done [1] to decide some problems for a selection of the vector meson decays to $e^+e^-$ final states. The most problem is the high combinatorial background which relates to the Dalitz decays or external $\gamma$-conversions and is essentially proportional to the square of number of $e^+e^-$ pairs. This difficulty is made worse by an impossibility to recognize and remove a large part of Dalitz decays and $\gamma$-conversions because of a loss of $e^+$ or $e^-$ from the decay pairs (as a consequence of the detector acceptance, tracking efficiency and particle identification).

In this paper we studied particularly an influence of the external conversions, since only some suppositions about ones have been discussed in the ALICE LoI [1]. Besides, we present some details for the selection cuts which were used in order to improve the signal-to-background ratio ($S/B$).

## 2. Rates of the γ-Conversions

To obtain a rate of γ-conversions, we used the GEANT-based program [2] for simulation of the ITS (Inner Tracking System) of the ALICE. Also, the HIJING code [3] has been chosen to generate an event of PbPb central collision at an energy of 6.3 A TeV. The event contained 79000 particles and gammas in all phase space, with charge particle density of $dN/dy \simeq 5000$ at $y = 0$. We cutted charge particle momenta from $p \geq 0.03$GeV/c and found 11122 γ and $e^+/e^-$ (54 $\epsilon^+e^-$ pairs) from the primary vertex of an interaction in the ITS rapidity region of $-1 \leq y \leq 1$.

The ITS simulation package [2] contains geometry decks with five cylindrical silicon detectors (silicon layers of 300 μm thickness, a mechanical supporting system and a cooling system). Besides, the beam-pipe has been put to the GEANT geometry (Be, a radius of 4 cm, a thickness of 0.2 cm, a radiation length of 0.56% of X0). By requiring a hit at the nearest position from the primary vertex, photon conversions were restricted to the beam-pipe and the first silicon detector (pixels). We note, that the radiation length of the pixel detector has been taken equal to 0.52% of X0 (0.32% for the silicon and 0.2% for the electronics) because a gas coolant and the beam-pipe as a support are assumed in this case. The $e^+/e^-$-tracks at a momentum of $p \geq 0.03$ GeV/c were selected as above.

The simulation result for numbers of the conversions is presented in Table 1. One can see from this that the $e^+/e^-$ conversion number (101) is near the same as one produced in the primary vertex. But, of course, a large rate of conversions can be recognized by the following signs:

- a secondary vertex (conversion point) of the $e^+e^-$ pair,
- a non-zero impact parameter of the single track,
- a double pulse-heigt of the hit as a consequence of double $dE/dx$ for close pairs which do not open up in the weak field (0.2 T).

The most problem for the first and second signs is a very high charge particle space density near the vertex. A rate of the recognized conversions depends on the track reconstruction algorithm and may be assumed reasonably of $(60 \div 80)$%. We found also that a mean distance between $e^+$ and $e^-$ is near 1 mm at the first silicon layer, when a photon converts inside the beam-pipe. It means that the third sign (double $dE/dx$) is realized only when the conversion point is inside the first silicon layer ($\simeq 50$% of the conversions). We note that an additional difficulty of such a method is also an existence of only one hit-point with a double pulse-height for a $e^+(e^-)$-track. According to Table 1, $10 \div 20$ conversion pairs remain unrecognized, $(20 \div 40)$% from the amount of 54 $e^+e^-$-pairs produced in primary vertex.

**Table 1. The conversion number from the simulation**

| γ-conversion pairs | Single $e^+$ from conversion pairs | Single $e^-$ from conversion pairs |
|---|---|---|
| 33 | 17 | 18 |

## 3. Simulation of $e^+e^-$ Pair Production

Next we used the SHAKER code [4] to generate production and $e^+e^-$ mode decays (two-and-three-body decays) of the $\pi^0$, $\eta$, $\rho^0$, $\omega$, $\phi$, $J/\varphi$ and Drell-Yan pairs in central PbPb collision at 6.3 A TeV. The particle numbers and ratios and the weights for particle $p_T$-distributions were taken just the same as in Refs. [1,5]. Also, the special parametrizations [1] of tracking efficiency and pion rejection have been put for the detector simulation (it should be noted that more realistic parametrizations are now under study). The rapidity region, $-1 \leq y \leq 1$, was considered.

Additional Dalitz pairs have been generated instead of $\gamma$-conversions, since an absence of a special conversion generator in the SHAKER code. To justify such a simplification, we emphasize a very small difference between transverse momentum spectra (at $p \geq 0.03$ GeV/c) of the conversions ($\langle p_T \rangle \simeq 0.126$ GeV/c) and Dalitz pairs ($\langle p_T \rangle \simeq 0.130$ GeV/c). Besides, a zero effective mass and very small angle between $e^+$ and $e^-$ have been imitated for the conversion pairs at the step of cut-1 (see below), because of important role of these characteristics for the background rejection. The rates of the conversions were taken from the simulation described in Section 2. We added 10 and 20 conversion pairs per event (to the 52 Dalitz ones) for an oprimistic and pessimistic versions, repectively.

## 4. Results of the SHAKER Simulation

As a result of the SHAKER simulation (100 K events), the $S/B$ values are presented in Tables 2 and 3 for three different variants:

- without the conversion $e^+e^-$ pairs,
- with 10 conversions per event (in addition to 52 Dalitz pairs),
- with 20 conversions per event.

**Table 2. Results of the SHAKER simulation for the $\rho^0$, $\omega$ region of $m_{ee}$**

| | *S/B* | | *S* | |
|---|---|---|---|---|
| | At $m_{ee}$ of 070 ÷ 0.84 GeV/c$^2$ | At $m_{ee}$ of 0.76 ÷ 0.84 GeV/c$^2$ | At $m_{ee}$ of 0.70 ÷ 0.84 GeV/c$^2$ | At $m_{ee}$ of 0.76 ÷ 0.80 GeV/c$^2$ |
| No conversions | 0.0018 | 0.0058 | 1433 | 1100 |
| 10 conversions per event | 0.0013 | 0.0036 | 1433 | 1010 |
| 20 conversions per event | 0.0010 | 0.0027 | 1403 | 1010 |

**Table 3. Results of the SHAKER simulation for the $\phi$ region of $m_{ee}$**

| | *S/B* | | *S* | |
|---|---|---|---|---|
| | At $m_{ee}$ of 0.95 ÷ 1.10 GeV/$c^2$ | At $m_{ee}$ of 1.00 ÷ 1.04 GeV/$c^2$ | At $m_{ee}$ of 0.95 ÷ 1.10 GeV/$c^2$ | At $m_{ee}$ of 1.00 ÷ 1.04 GeV/$c^2$ |
| No conversions | 0.0021 | 0.0073 | 530 | 490 |
| 10 conversions per event | 0.0016 | 0.0054 | 534 | 485 |
| 20 conversions per event | 0.0012 | 0.0040 | 537 | 492 |

**Table 4. The same as in Table 2 (for 20 conversions) with the cuts 1 ÷ 4 (see text)**

| Cuts | *S/B* | | *S* | |
|---|---|---|---|---|
| | At $m_{ee}$ of 0.70 ÷ 0.84 GeV/$c^2$ | At $m_{ee}$ of 0.76 ÷ 0.80 GeV/$c^2$ | At $m_{ee}$ of 0.70 ÷ 0.84 GeV/$c^2$ | At $m_{ee}$ of 0.76 ÷ 0.80 GeV/$c^2$ |
| 1 | 0.005 | 0.0015 | 350 | 246 |
| 2 | 0.008 | 0.0021 | 133 | 97 |
| 3 | 0.004 | 0.0109 | 59 | 42 |
| 4 | 0.059 | 0.158 | 55 | 42 |

**Table 5. The same as in Table 3 (for 20 conversions) with the cuts 1 ÷ 4 (see text)**

| Cuts | *S/B* | | *S* | |
|---|---|---|---|---|
| | At $m_{ee}$ of 0.95 ÷ 1.10 GeV/$c^2$ | At $m_{ee}$ of 1.00 ÷ 1.04 GeV/$c^2$ | At $m_{ee}$ of 0.95 ÷ 1.10 GeV/$c^2$ | At $m_{ee}$ of 1.00 ÷ 1.04 GeV/$c^2$ |
| 1 | 0.006 | 0.022 | 145 | 132 |
| 2 | 0.008 | 0.028 | 67 | 62 |
| 3 | 0.020 | 0.069 | 40 | 37 |
| 4 | 0.038 | 0.132 | 31 | 29 |

The numbers of $e^+e^-$ pairs from $\rho^0$-, $\omega$- and $\phi$-resonances ($S$) are shown also. All results are presented for different regions of $e^+e^-$ effective mass ($m_{ee}$) and after the cuts for the tracking efficiency and pion rejection [1] and for an acceptance restriction ($\theta = 90° \pm 40°$).

One can see from Tables 2 and 3 that ratios are too small and an influence of the conversions is significant enough. In order to improve the $S/B$ ratio we applied a number of successive cuts (step by step) for the $e^+e^-$ effective mass and some kinematic variables of kinematic $e^+$ and $e^-$ from the $e^+e^-$-pairs. First of all, the cuts from the LoI [1] have been used. An order of the cuts is following:

1. All $e^+$ and $e^-$ forming pairs of $m_{ee} \leq 100$ MeV/c$^2$ are discarded if the opening angle between the $e^+$ and $e^-$ is less than 26° ($\cos(\theta) \geq 0.9$).

2. All $e^+$ and $e^-$ with the $m_{ee} \leq 150$ MeV/c$^2$ are removed from the next step.

3. In the next step, we remove $e^+$ and $e^-$ which are outside the fiducial area of $90° \pm 40°$ or have a $p_T$ below 450 MeV/c.

4. Finally, we form the invariant mass of all pairs with $p_T$(pair) $\geq 1$ GeV/c.

The results of the cuts $1 \div 4$ are shown in Tables 4 and 5 for the 100 K SHAKER events with 20 conversions (per event).

**Table 6. The $S/B$ values after the cut 3 (see text) at the $p_T$ cut of 600 MeV/c**

| | At $m_{ee}$ of 0.70 ÷ 0.84 GeV/c$^2$ | At $m_{ee}$ of 0.76 ÷ 0.80 GeV/c$^2$ | At $m_{ee}$ of 0.95 ÷ 1.10 GeV/c$^2$ | At $m_{ee}$ of 1.00 ÷ 1.04 GeV/c$^2$ |
|---|---|---|---|---|
| No conversions | 0.18 | 0.42 | 0.08 | 0.30 |
| 10 conversions per event | 0.13 | 0.40 | 0.07 | 0.32 |
| 20 conversions per event | 0.10 | 0.29 | 0.05 | 0.17 |

**Table 7. The same as in Table 6 at the $p_T$ cut of 750 MeV/c**

| | At $m_{ee}$ of 0.70 ÷ 0.84 GeV/c$^2$ | At $m_{ee}$ of 0.76 ÷ 0.80 GeV/c$^2$ | At $m_{ee}$ of 0.95 ÷ 1.10 GeV/c$^2$ | At $m_{ee}$ of 1.00 ÷ 1.04 GeV/c$^2$ |
|---|---|---|---|---|
| No conversions | 0.36 | 0.96 | 0.20 | 0.77 |
| 10 conversions per event | 0.27 | 0.77 | 0.13 | 0.51 |
| 20 conversions per event | 0.24 | 0.64 | 0.11 | 0.40 |

**Table 8. The same as in Table 2 with the optimized cuts (see text)**

| | *S/B* | | *S* | |
|---|---|---|---|---|
| | At $m_{ee}$ of 0.70 ÷ 0.84 GeV/$c^2$ | At $m_{ee}$ of 0.76 ÷ 0.80 GeV/$c^2$ | At $m_{ee}$ of 0.70 ÷ 0.84 GeV/$c^2$ | At $m_{ee}$ of 0.76 ÷ 0.80 GeV/$c^2$ |
| 10 conversions per event | 0.26 | 0.69 | 45 | 33 |
| 20 conversions per event | 0.21 | 0.60 | 39 | 30 |
| 20 conversions per event for $3 \times 10^6$ events | 0.18 | 0.51 | 1168 | 865 |

**Table 9. The same as in Table 3 with the oprimized cuts (see text)**

| | *S/B* | | *S* | |
|---|---|---|---|---|
| | At $m_{ee}$ of 0.95 ÷ 1.10 GeV/$c^2$ | At $m_{ee}$ of 1.00 ÷ 1.04 GeV/$c^2$ | At $m_{ee}$ of 0.95 ÷ 1.10 GeV/$c^2$ | At $m_{ee}$ of 1.00 ÷ 1.04 GeV/$c^2$ |
| 10 conversions | 0.13 | 0.41 | 27 | 25 |
| 20 conversions per event | 0.10 | 0.31 | 25 | 23 |
| 20 conversions per event for $3 \times 10^6$ events | 0.10 | 0.34 | 744 | 691 |

It is seen from Tables 4 and 5 that the cuts 1 and 3 are the most effective ones (the *S/B* increases by a factor of 5 ÷ 6) and cuts 2 and 4 rather weakly affect the *S/B* value but, however, cut 2 decreases near 2 ÷ 2.5 times the resonance numbers. Next we checked punctually the optimization of cuts 1 ÷ 4. We found that cut 1 is optimized enough, however, because of combinatorial effect an amount of 0.3% of Dalitz pairs remains only after this cut action and practically single $e^+$ and $e^-$ come to the next step (cut 2). This is a main reason of the low efficiency of cut 2, and the situation is not improved by a change of the limit near the value of 150 MeV/$c^2$. Further it was found that the *S/B* ratio is very sensitive to the limit in cut 3. This effect is seen from Tables 6 and 7, where the *S/B* values are presented after an action of cut 3 at the $p_T$ limit of 600 MeV/c and 750 MeV/c, respectively, and for different numbers of the conversion $e^+e^-$ pairs.

The rise of the $p_T$ limit from 450 MeV/c up to 750 MeV/c increases the $S/B$ ratio by a factor of $5 \div 7$. But, it should be noted that the resonance numbers decrease near two times. We note also that cut 4 does not practically change the $S/B$ values in this case. To optimize the $S/B$ ratios and resonance numbers cuts 2 and 4 have been removed and the $p_T$ limit (in cut 3), equal to 750 MeV/c, has been chosen. The final results for the optimized cuts are shown in Tables 8 and 9 for $10^5$ events and $3 \times 10^6$ events (for 20 conversions).

Figure 1 shows the effective mass distribution of pairs $e^+e^-$ (from resonances and background) at the optimized cuts for $3 \times 10^6$ events. Figure 2 shows the contribution, where both $e^+$ and $e^-$ come from one resonance ($\rho^0$, $\omega$, $\phi$). The results of the fits (Gaussian — for the resonances and exponential — for the background) are shown as well.

Table 10 presents extrapolated values of $S$ and $S/\sqrt{B}$ (the significance) to the amount of $5 \times 10^7$ events.

**Table 10. Extrapolated values of $S$ and $S/\sqrt{B}$ (siginficance) to the amount of $5 \times 10^7$ events**

| | $S$ | $S/\sqrt{B}$ |
|---|---|---|
| At $m_{ee}$ of $0.76 \div 0.80$ GeV/c$^2$ | 14420 | 85 |
| At $m_{ee}$ of $1.00 \div 1.04$ GeV/c$^2$ | 11520 | 63 |

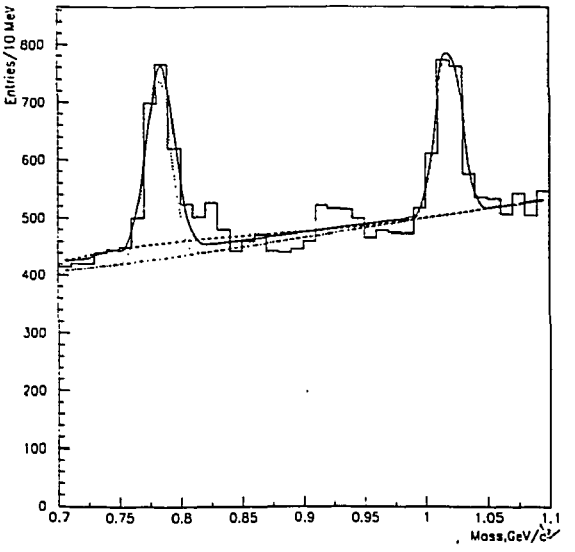


Fig.1. Effective mass distribution of $e^+e^-$ pairs from the $\rho^0$, $\omega$, $\phi$ resonances and background at the optimized cuts (see text). The curves are the results of fits: Gaussian — for the resonances and exponential — for the background

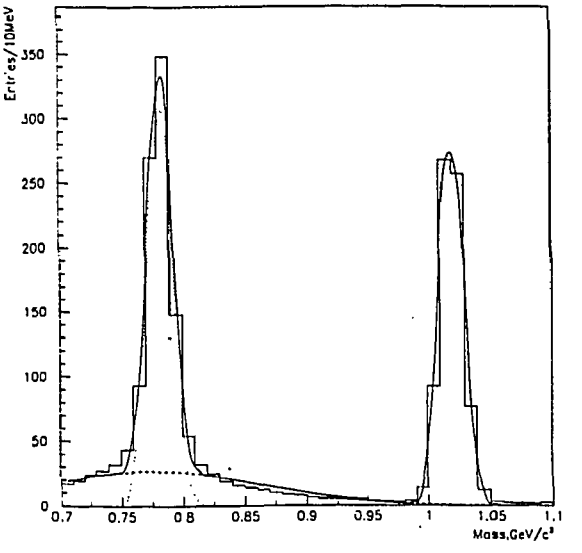


Fig.2. Effective mass distribution of pairs where both $e^+$ and $e^-$ come from one of the resonances ($\rho^0$, $\omega$ or $\phi$). The curves are the results of Gaussian fits

## 5. Conclusion

The results presented in this paper show that the external $\gamma$-conversion decreases the signal-to-background ratio ($S/B$) by a factor of $1.5 \div 2$ for the $\omega$ and $\phi$ resonances. But, on the other hand, the optimization of the selection cuts allows one to increase $S/B$ value by factors of $5 \div 6$. Finally, we obtained the signal-to-background ratio of $S/B \simeq 0.5$ and 0.3 for $\omega$ and $\phi$ mesons, respectively, at the oprimized selection cuts.

## 6. Acknowledgements

We are very grateful to A.A.Baldin, J.Schukraft, A.Vodopianov, A.Zinchenko for useful discussions and suggestions.

## References

1. Letter of Intent for a Large Ion Collider Experiment, CERN/LHCC/93-16, LHCC/I 4, March 1993.
2. Batyunya B., Zinchenko A. — Internal Note/SIM ALICE/94-11, 1994; ALICE/94-31,1994.
3. Wang N.X. et al. — Phys. Rev., 1991, D44, p.3521; Phys. Rev. Lett., 1992, 68, p.1480.
4. Antinori F. — Internal Note/SIM ALICE/93-09, 1993.
5. Bohm J. — Internal Note/SIM ALICE/93-10, 1993.

Received on September 5, 1995.

*Краткие сообщения ОИЯИ №6[74]-995* *JINR Rapid Communications No.6[74]-95*

УДК 539.1.074.23

# КРАЕВЫЕ ЭФФЕКТЫ В МНОГОПРОВОЛОЧНЫХ ПРОПОРЦИОНАЛЬНЫХ КАМЕРАХ

*М.Д.Шафранов*

Применявшиеся до сих пор методы расчета полей и потенциалов в рабочем объеме многопроволочных пропорциональных камер (МППК) выполнены в предположении, что сигнальные проволочки камеры не ограничены как по числу, так и по длине. По этой причине данные о краевых эффектах этих камер не могли быть получены. В настоящей работе на основе специально разработанного метода компьютерного моделирования впервые получены электрические характеристики планарных МППК конечных размеров, в том числе на краях камер. Расчеты позволили определить область камеры, в которой краевые эффекты играют заметную роль.

Работа выполнена в Лаборатории сверхвысоких энергий ОИЯИ.

## Edge Effects in Multiwire Proportional Chambers

*M.D.Shafranov*

Earlier, the methods to calculate the fields and potentials in the working volume of multiwire proportional chambers (MWPC) have been used supposing the number of the sense wires and their length to be unlimited. That is why the data on the edge effects of these chambers could not be obtained. This work shows the electric features of the planar MWPC of the limit sizes including the chamber edges, received with a specially developed method of computer modelling. The calculations allowed one to determine the chamber parts where the edge effects are significant.

The investigation has been performed at the Laboratory of Particle Physics, JINR.

## 1. Введение

Достижения современной физики высоких энергий и элементарных частиц обязаны успехам в развитии методов эксперимента, связанных в первую очередь с использованием позиционно-чувствительных, или координатных, детекторов. В качестве основных координатных детекторов в экспериментальной физике элементарных частиц свыше четверти века применяются многопроволочные пропорциональные камеры (МППК) [1—3]. Многопроволочные камеры, применяемые как детекторы заряженных частиц, успешно используются и для регистрации нейтральных частиц [4]. Функцией координатного детектора является преобразование ионизационного эффекта, создаваемого заряженной частицей, проходящей через активную среду детектора, в электрический сигнал. Требование к детектору — максимально возможная эффективность и минимальные ошибки в получаемой пространственной и временной информации.

Основными составными элементами МППК являются механическая структура, электродная система и газовое наполнение. Электродная система состоит из двух параллельных катодных плоскостей, расположенных на расстоянии $2l$. Между катодными плоскостями эквидистантно размещены сигнальные проволочки, находящиеся на расстоянии $s$ друг от друга. Электродная система обеспечивает дрейф первичных электронов, создаваемых детектируемой частицей за счет ионизации, и работу механизма газового усиления в окрестности конкретной сигнальной (анодной) проволочки камеры. В окрестность сигнальной проволочки из-за структуры электрического поля могут попасть первичные электроны ионизации только из ограниченного пространства, поэтому электрический сигнал несет и координатную пространственную информацию.

Первые исследования планарных МППК и их эксплуатация показала, что с увеличением на камере рабочих напряжений растет число шумовых импульсов на крайних проволочках, возможно и появление искровых разрядов. Чтобы свести такие явления к минимуму, были разработаны различные меры, например, применение охранных рамок, постепенное увеличение диаметров нескольких крайних проволочек к краям камеры. В некоторых случаях применялась изоляция крайних проволочек, которые вследствие этого приобретали плавающий потенциал [5].

Были проведены расчеты конфигурации электрических полей в планарных МППК. Они выполнены в предположении, что камеры не ограничены как по числу сигнальных проволочек, так и по своим размерам вдоль сигнальных проволочек [6]. Расчеты сыграли важную роль в понимании того факта, что каждая проволочка камеры работает как независимый счетчик. Эти же расчеты показали, как изменение диаметра одной из проволочек, смещение проволочки влияет на физические характеристики камер. Они позволили оценить необходимые механические допуски при изготовлении камер. Вместе с тем такие расчеты [6—8] в принципе не могут дать информации о краевых эффектах. На это было указано еще в [9]. К краевым эффектам относится изменение величины и конфигурации электрического поля на краях электродов, образующих катод камеры, как вдоль крайних проволочек камеры, так и на концах всех сигнальных проволочек. Конфигурация и величина электрических полей на краях камеры по сравнению с тем, что имеет место в центральной области, связаны с диэлектрическими свойствами механических структур камеры. К таким механическим структурам относятся диэлектрические рамки. Наибольшие изменения электрического поля вдоль крайних проволочек связаны с увеличением емкости проволочек в указанных выше областях рабочего объема камеры. Это утверждение будет подтверждено результатами моделирования, приведенными ниже.

Моделирование выполнено по специально разработанному для данного случая алгоритму. Он основан на методе изображений, или точнее, на методе решений задач электростатики по граничным условиям [10]. Рассмотрим некоторые результаты компьютерного моделирования электрических полей и потенциалов пропорциональной камеры конечных размеров *с ограниченным числом анодных проволочек.*

Объектом моделирования служила многопроволочная пропорциональная камера, образованная из проволочек диаметром 20 мкм. Расстояние $l$ между плоскостью сигнальных проволочек и катодом составляло 8 мм, а расстояние между проволочками (шаг намотки) $s$ было равно 2 мм. Рабочая площадь камеры из 83 проволочек

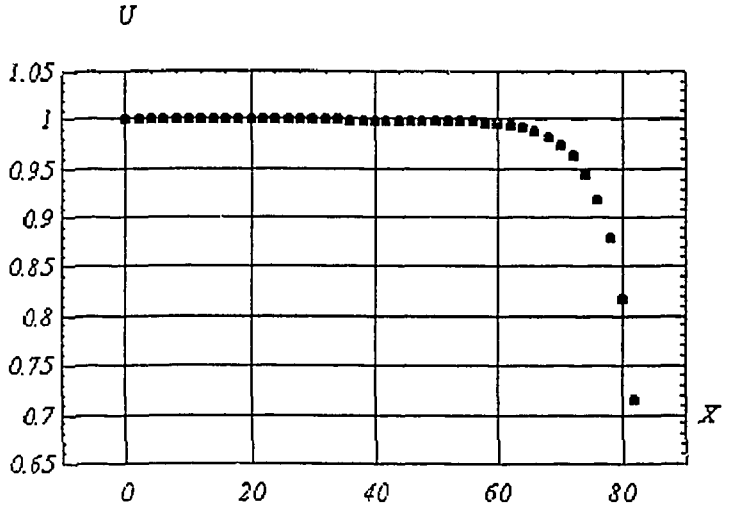


Рис.1. Разность потенциалов $U$ проволочка—катод в зависимости от положения проволочки. Линейные плотности зарядов всех проволочек одинаковы. Диаметры всех проволочек одинаковы и равны 20 мкм. $X = 0$ соответствует центру камеры

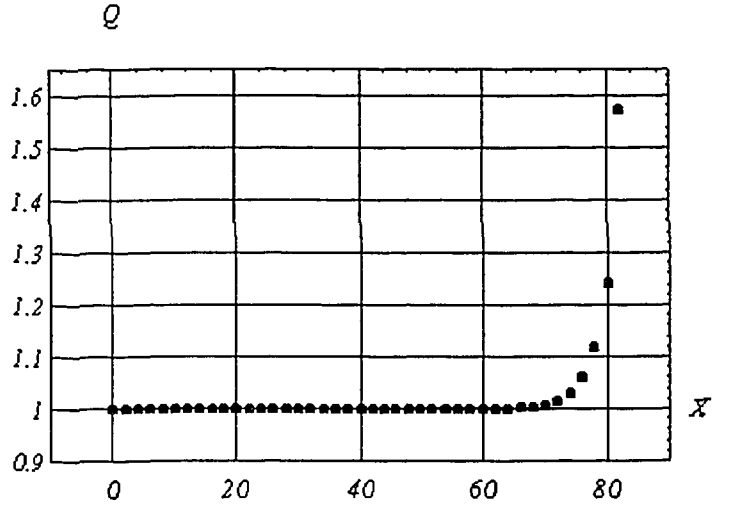


Рис.2. Величина заряда $Q$ на проволочке в зависимости от ее положения. Разность потенциалов проволочка — катод одинакова для всех проволочек. Диаметры всех 83 проволочек одинаковы

$\approx 160 \times 160$ мм. Величины $s$ и $l$ выбраны так, чтобы была возможность сравнить характеристики этой камеры с характеристиками камер, не ограниченных по своим размерам [6,11].

Смоделируем самый простой случай, когда *заряды всех проволочек одинаковы*. Определим разность потенциалов промежутка катодная плоскость — сигнальная проволочка для каждой проволочки камеры. Результат расчета представлен на рис.1. Система координат выбрана следующим образом: ось OX лежит в плоскости проволочек и перпендикулярна им, координата $X = 0$ соответствует центру камеры, через который проходит центральная проволочка. Видно, что чем ближе к одному из краев камеры, тем меньше относительная разность потенциалов промежутка проволочка — катод. Для крайних проволочек она резко падает, доходя до 70% от значения в центральной области камеры. С физической точки зрения интерпретация полученного результата довольно проста. Вспомним соотношение между зарядом на проводнике $q$, его потенциалом $V$ и электроемкостью $C$: $q = CV$. Из этого соотношения следует, что при равенстве зарядов проволочек между собой уменьшение потенциалов крайних проволочек связано только с *увеличением емкости* крайних проволочек. Увеличение емкости крайних проволочек приводит к росту их заряда, к усилению электрического поля в окрестности этих проволочек, отсюда возможные нежелательные последствия усиления поля. Ограничения диапазона рабочих напряжений на камере для уменьшения роли краевых эффектов эквивалентно сокращению области плато по напряжению.

Значения емкостей проволочек можно найти, выполнив вычисления величин зарядов каждой проволочки так, чтобы разность потенциалов $U(i)$ между любой $i$-й проволочкой и катодной плоскостью была постоянна, что и соответствует нормальному рабочему режиму камеры. Результаты вычислений величин зарядов при точности вычислений $U(i) = 1{,}0 \pm 0{,}000002$ представлены на рис.2.

Из рис.2 следует, что наибольшее увеличение зарядов происходит на четырех крайних проволочках. С увеличением зарядов связан рост коэффициента газового усиления $M$. Коэффициент газового усиления $M$ следующим образом зависит от величины линейной плотности заряда $\sigma$ проволочки $M = K \times \exp \sigma$ [11]. Это соотношение позволяет оценить изменение коэффициента газового усиления проволочек по отношению к центральным. Изменение для двух крайних проволочек составляет примерно 80 и 30% соответственно.

## 2. Роль крайних проволочек увеличенного диаметра

На практике эксперимента на краях пропорциональных камер для уменьшения роли краевых эффектов применяются проволочки большего диаметра. Покажем на конкретном примере, что происходит при увеличении диаметров крайних четырех проволочек. В таблице представлены значения диаметров этих проволочек от края к центру камеры в мкм и относительные величины зарядов на них (камера 2). Зная зависимость поля $E$ на поверхности проволочки от ее радиуса $r$, $E \sim \sigma / r$, где $\sigma$ — линейная плотность заряда проволочки, нетрудно убедиться, что величина электрического поля на поверхности четырех крайних проволочек меньше, чем на остальных. Это отражено в последней строке таблицы. Как видно из таблицы, напряженность электрического поля на этих проволочках такова, что исключает возможность появления шумовых импульсов и пробоев.

**Таблица**

| N пров. | Камера 1 | | | | | Камера 2 | | | | |
|---|---|---|---|---|---|---|---|---|---|---|
| | 1 | 2 | 3 | 4 | центр | 1 | 2 | 3 | 4 | центр |
| Диам. | 20 | 20 | 20 | 20 | 20 | 50 | 40 | 30 | 25 | 20 |
| Заряд | 1.57 | 1.24 | 1.12 | 1.06 | 1.0 | 1.79 | 1.32 | 1.14 | 1.06 | 1.0 |
| Поле | 1.57 | 1.24 | 1.12 | 1.06 | 1.0 | 0.70 | 0.66 | 0.76 | 0.85 | 1.0 |

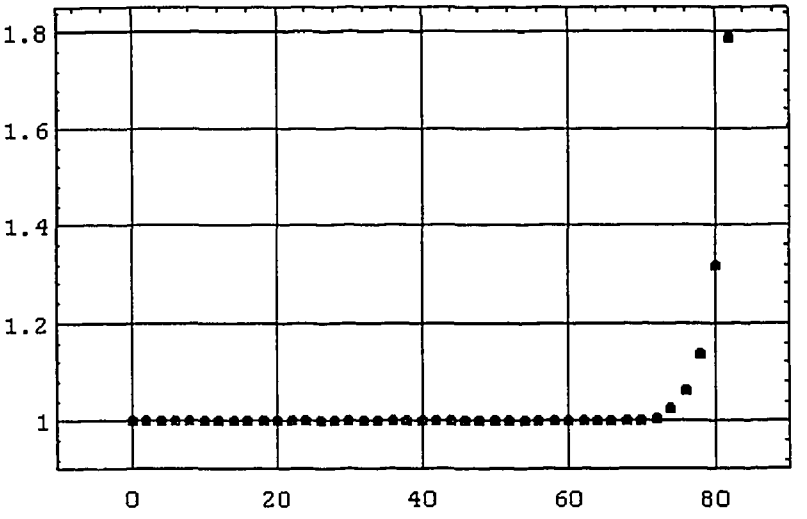


Рис.3. Величина заряда на проволочке в зависимости от ее положения для камеры из 83 проволочек. Диаметры всех проволочек равны 20 мкм за исключением 4-х крайних, равных 25, 30, 40 и 50 мкм

Распределение зарядов для этого случая между проволочками показано на рис.3.

В таблице для сравнения приведены данные для камеры с проволочками одинаковых диаметров (камера 1). Электрическое поле на поверхности 2-х крайних проволочек этой камеры в два раза больше поля на поверхности проволочек увеличенного диаметра (камера 2).

Анализ результатов вычислений, которые представлены на рис.2 и 3, позволяет сделать следующее предположение: уменьшение или увеличение общего числа проволочек при сохранении всех геометрических характерстик камеры не приведет к заметному изменению относительных величин зарядов крайних проволочек.

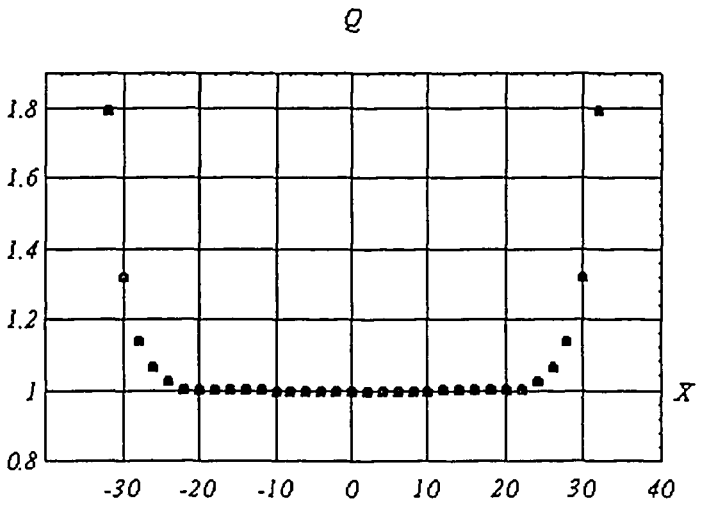


Рис.4. Величина заряда на проволочке в зависимости от ее положения для камеры из 33 проволочек. Диаметры всех проволочек равны 20 мкм за исключением 4-х крайних, равных 25, 30, 40 и 50 мкм

Покажем справедливость этого предположения. На рис.4 дано распределение зарядов для камеры из 33 проволочек. Крайние проволочки камер из 33 и 83 проволочек идентичны, а величины $s$ и $l$ одинаковы для обеих камер. Сравнение результатов расчетов для камер из 83 и 33 проволочек показывает, что разница в величинах зарядов крайних проволочек не превышает $(3 + 4) \times 10^{-6}$. Это происходит несмотря на уменьшение числа проволочек в 2,5 раза. Тем самым подтверждается предположение о том, что изменение величин зарядов крайних проволочек связано только с увеличением их емкости, но не с числом проволочек камеры. Таким образом, краевые эффекты обязаны только 4—5 крайним проволочкам, т.е. *краевые эффекты ограничены областью ~10 мм* вдоль крайних проволочек.

## 3. Изменение конфигурации электрического поля на краях камеры

Если диаметры проволочек одинаковы, то увеличение емкости проволочек к краям камеры происходит только за счет площади катода, которую занимают заряды, индуцируемые зарядами соответствующей проволочки. Величина этой площади будет увеличиваться к краям камеры. Следствием этого явится изменение формы элементарной ячейки камеры. Это справедливо и в случае использования проволочек большего диаметра. Но при этом дополнительное увеличение емкости связано с изменением диаметра проволочек. В центральной области камеры ячейка в сечении является прямоугольником размером $s \times 2l$. Что происходит на краях камеры, показано на рис.5. На нем изображено медианное сечение камеры в районе 8 крайних проволочек (прово-

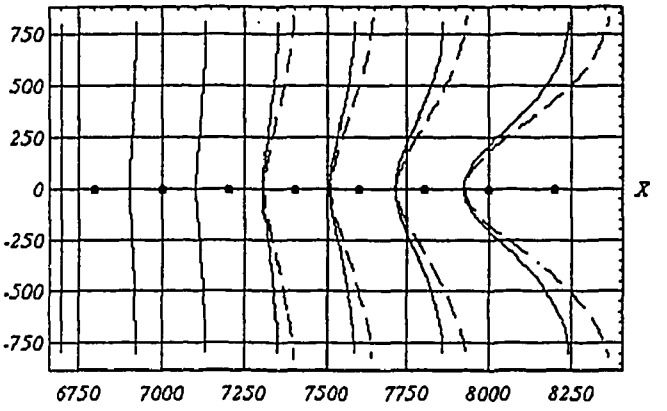


Рис.5. Конфигурация элементарных ячеек камеры из 83 проволочек в медианном сечении на одном из ее краев в районе 8 крайних проволочек. Видно изменение формы прямоугольных ячеек камеры. Сплошными кривыми показаны границы между ячейками для камеры, у которой диаметры 4-х крайних проволочек увеличены. Пунктирные кривые — границы ячеек камеры с проволочками равных диаметров. По каждой из осей X и Y 100 делений соответствуют 1 мм.

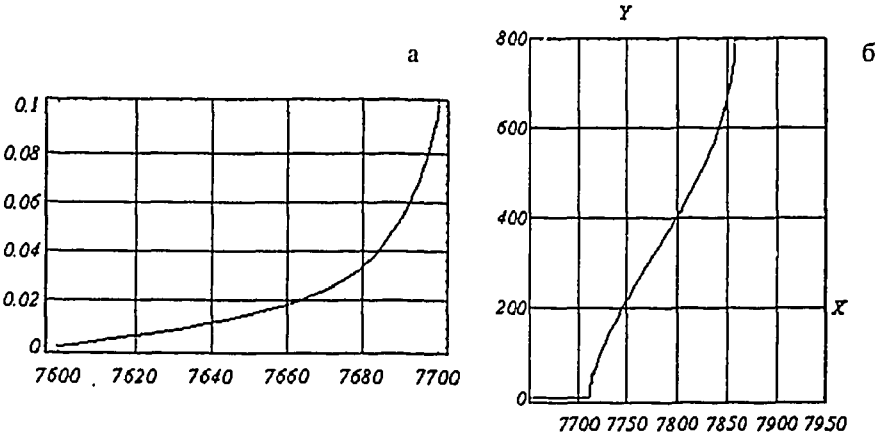


Рис.6. Линия электрического поля в медианной плоскости, начинающаяся на 4-й от края проволочке. Линия проходит через точку, расположенную посредине между 4-й и 3-й крайними проволочками по оси X и смещенную на 1 мкм по оси Y. а — ее начальный участок, б — вся линия поля от проволочки до катодной плоскости.

лочки 76 ÷ 83). Сплошными кривыми обозначены границы элементарных ячеек камеры, у которой диаметр четырех крайних проволочек увеличен (табл.1). Границы ячеек камеры с проволочками одинакового диаметра показаны штрихпунктиром. Из рисунка видно, как деформируется прямоугольная элементарная ячейка к краю камеры. Ее форма приобетает сложный характер. На краях камеры ячейка ограничивается криволинейными поверхностями.

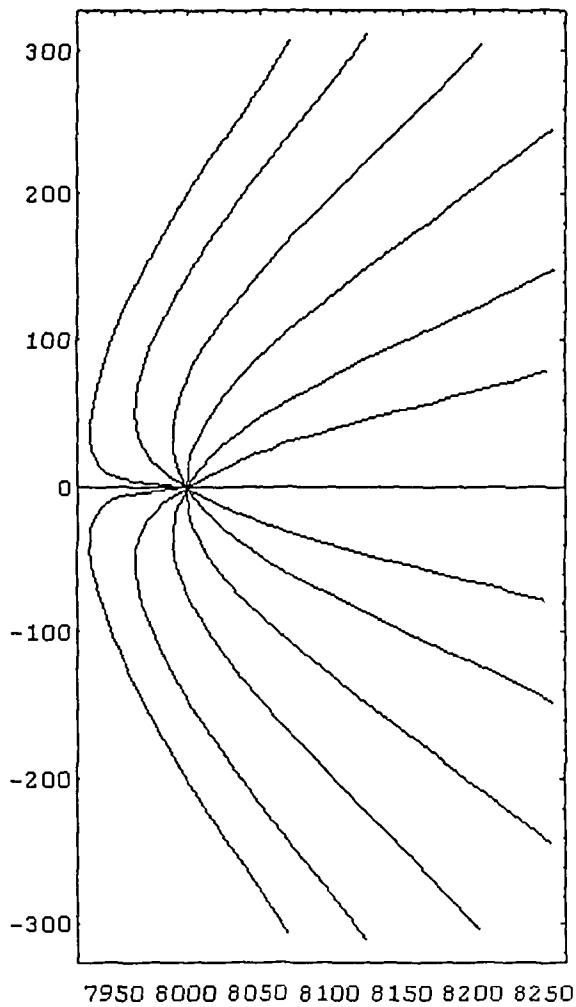


Рис.7. Карта силовых линий поля в медианной плоскости, начинающихся на второй проволочке от края камеры. Все линии деформированы и отклонены в направлении края камеры

Меняется в этой области и сама конфигурация электрического поля. На рис.6 показана одна из линий электрического поля вблизи края камеры. На рис.6а показан ее начальный участок. Система координат для этого случая выбрана следующим образом: координаты $X = 0$, $Y = 0$ соответствуют центру камеры, через который проходит центральная проволочка. Ось OX лежит в плоскости проволочек, ось OY направлена вдоль нормали к плоскости проволочек. Цена одного деления шкал по осям равна 10 мкм (100 делений шкалы соответствуют 1 мм). Таким образом, координата (7600,0) соответствует центру 4-й крайней проволочки. Силовая линия проходит через точку, расположенную на оси OX точно посредине между 4-й и 5-й крайними проволочками, но смещенную вдоль оси OY только на 1 мкм.

В отсутствие краевого эффекта силовая линия проходила бы в дальнейшем параллельно оси OY при значении $X = 7700$, а не так, как это показано на рис.6б. На рис.6б эта линия поля изображена полностью от проволочки до катода. Ее смещение на катоде составляет 1,52 мм. На рис.7 представлена карта силовых линий поля, начинающихся на 82-й проволочке. Все линии поля смещены к краю камеры.

Конфигурация электрического поля элементарной рабочей ячейки камеры определяется линейным зарядом анодной проволочки, принадлежащей этой ячейке, а также линейными зарядами соседних проволочек. Зависимость электрического поля $E$ от расстояния до линейного источника определяется соотношением $E \sim \sigma / r$. Поэтому число линейных зарядов, вносящих заметный вклад в величину поля ячейки, не превышает 8 ÷ 10 с каждой стороны проволочки. Это частично видно на рис.3 и 4. В непосредст-

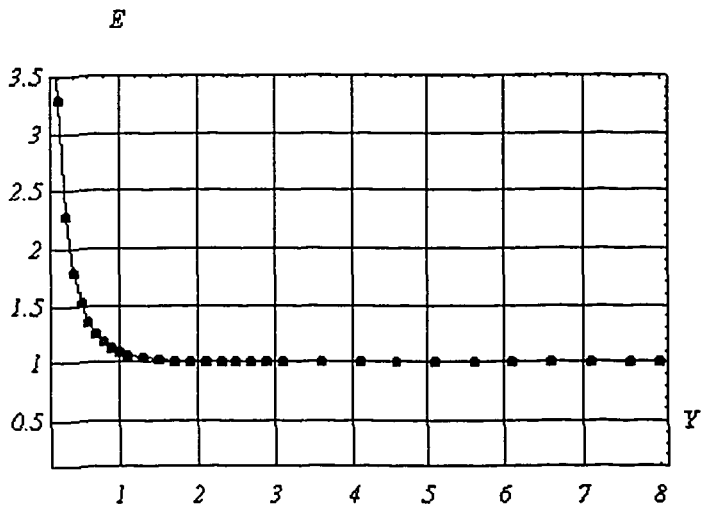


Рис.8. Изменение электрического поля по линии, проходящей через центр одной из проволочек камеры вдоль направления, перпендикулярного плоскости проволочек

венной близости от самой проволочки поле определяется зарядом проволочки. Поэтому распределение поля и потенциала в окрестности проволочки эквивалентно распределению полей и потенциалов круглого цилиндрического счетчика. На некотором расстоянии от проволочки по направлению к катоду составляющие электрического поля вдоль плоскости проволочек (продольные составляющие поля), имеющие противоположные направления, будут взаимно уравновешиваться. Таким образом, фактически остаются только составляющие поля, направленные вдоль нормали к катоду. Эти составляющие в сумме образуют постоянное электрическое поле начиная примерно с 1 мм от проволочки по направлению к катоду (рис.8). Вблизи краев камеры продольные составляющие поля уже не уравновешиваются. Этот дисбаланс увеличивается к краю камеры, так как с одной из сторон число и величина действующих линейных зарядов остается неизменной, а с другой — уменьшается. С разницей в числе и величинах линейных зарядов слева и справа от проволочки ячейки связана деформация элементарной ячейки на краях камеры. Увеличение линейных плотностей проволочек частично компенсирует дисбаланс в зарядах слева и справа. У камеры с одинаковым диаметром крайних проволочек заряды на этих проволочках меньше зарядов проволочек камеры с увеличенными диаметрами проволочек (табл.1). Поэтому деформация элементарных ячеек камеры с проволочками одинаковых диаметров будет выражена сильнее. На рис.5 границы между ячейками для такой камеры показаны штрихпунктирными кривыми. Таким образом, увеличение диаметров крайних проволочек камеры выполняет двоякую роль. Увеличение диаметров проволочек уменьшает электрическое поле на их поверхности. Величина поля на них не превышает поля

остальных проволочек (табл.1), несмотря на увеличение линейного заряда этих проволочек в сравнении с линейным зарядом на проволочках камеры с идентичными проволочками. Увеличение линейного заряда проволочек большего диаметра приводит к уменьшению деформации крайних элементарных ячеек камеры.

## 4. Краевые эффекты у концов проволочек

Во всех расчетах заложено предположение о том, что линейная плотность заряда вдоль проволочки постоянна. Приведенные выше результаты являются указанием на то, что заметное изменение линейной плотности зарядов будет происходить только на концах проволочек, на длине не более $10 \div 15$ мм. Для того чтобы лучше понять, что происходит у концов проволочек, рассмотрим идеализированный прототип камеры с проволочками, которые как бы висят без соединения (подпайки) их концов с системами съема сигнала. Длина проволочек равна расстоянию между первой и последней проволочками. Линейная плотность заряда постоянна вдоль проволочек. Диаметры всех проволочек одинаковы. Результаты расчета потенциала вдоль центральной проволочки приведены на рис.9, они обозначены точками. Сплошной кривой показана зависимость потенциала от проволочки к проволочке, как и на рис.1, линейная плотность заряда проволочек одинакова. По законам электростатики такого согласия результатов и следовало ожидать. На рис.10 приведено подобное распределение потенциала вдоль диагонали камеры. Расчет выполнен при условии, что линейная плотность заряда распределена между проволочками в соответствии с распределением заряда, показанным на рис.2. Некоторое превышение над той же кривой, что и на рис.9, связано с увеличением линейной плотности зарядов на крайних проволочках (см. рис.2).

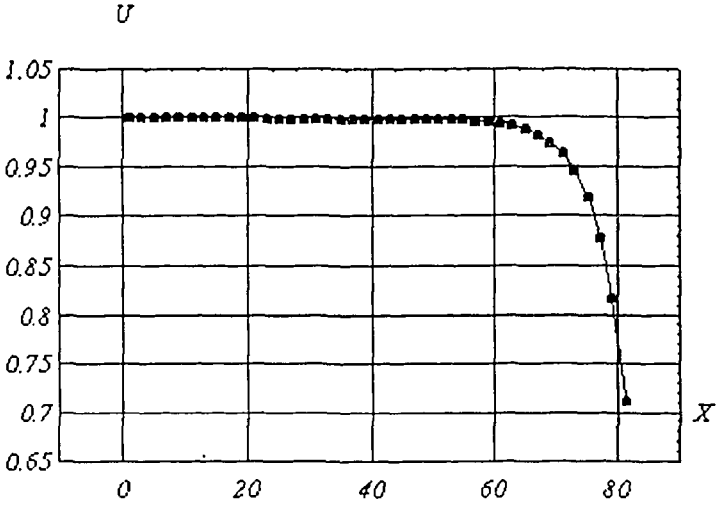


Рис.9. Разность потенциалов $U$ проволочка — катод вдоль центральной проволочки камеры. Линейная плотность заряда вдоль всей проволочки одинакова, линейная плотность заряда на всех проволочках одинакова. $X = 0$ соответствует центру камеры

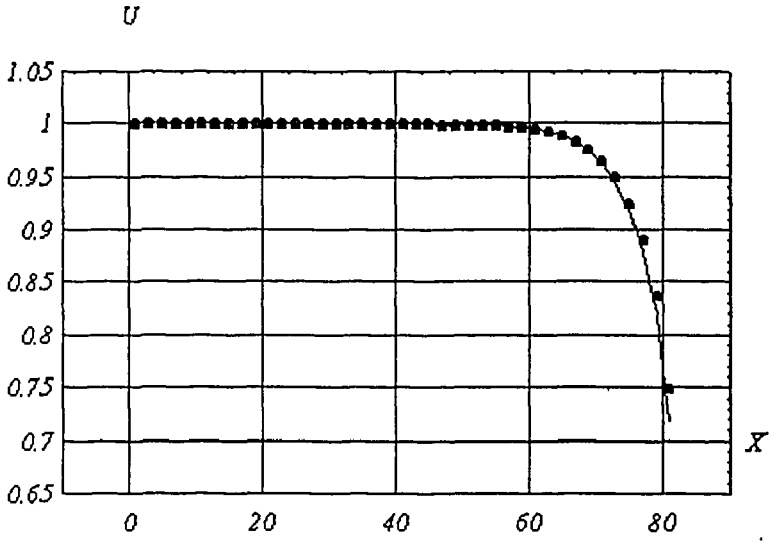


Рис.10. Разность потенциалов $U$ проволочка — катод вдоль диагонали камеры. Линейная плотность заряда вдоль каждой проволочки постоянна, линейная плотность заряда при переходе от проволочки к проволочке соответствует рис.2

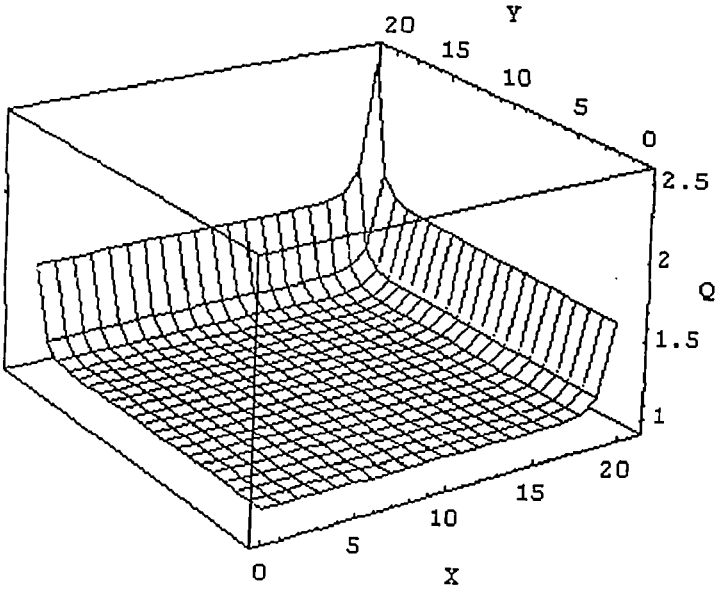


Рис.11. Линейная плотность заряда $Q$ вдоль проволочки и от проволочки к проволочке в одном из квадрантов камеры. Разность потенциалов проволочка — катод для всех проволочек камеры одинакова

Все полученные данные позволяют сделать заключение о том, что линейная плотность заряда вдоль проволочек распределена аналогично распределению плотности от проволочки к проволочке в соответствии с рис.2. При этом заметное изменение, как и предполагалось ранее, приходится на концевые участки проволочек размером 10 ÷ 15 мм. Идеализированное распределение зарядов по проволочкам и вдоль них в одном из квадрантов камеры показано на рис.11. На нем вдоль оси X обозначены номера нечетных проволочек, начиная с центральной, по оси Y — номера точек, взятых через 4 мм вдоль проволочки. Величины зарядов (ось Z) приведены в относительных единицах. Из рисунка следует, что при увеличении напряжений наибольшая вероятность появления разрядов на камере приходится на углы камеры. В области углов наблюдается общее увеличение линейной плотности заряда на крайних проволочках, а также ее увеличение к концам проволочек, если в последнем случае не учитывать влияние диэлектрической рамки.

В практике эксперимента в качестве пучковых используются МППК с проволочками диаметра 10 мкм, шагом намотки, равным 1 мм. Были выполнены расчеты для такой камеры с межкатодным расстоянием, равным 4 мм. Как видно, все геометрические размеры камеры для этого случая уменьшены в 2 раза по сравнению с размером камеры, рассмотренной ранее. На основании принципа подобия при решении задач электростатики можно ожидать совпадения результатов расчета в обоих случаях не только качественно, но и количественно. Действительно, количественные результаты совпадают с точностью выше чем $1 \times 10^{-5}$.

Степень влияния диэлектрических рамок на величину и конфигурацию электрического поля по периметру камеры зависит от конструктивных особенностей камеры. Вместе с тем эта зависимость в принципе носит различный характер, на краях камеры вдоль проволочек, с одной стороны, и вдоль концевых участков сигнальных проволочек — с другой. В первом случае диэлектрическая рамка в той или иной степени усиливает краевой эффект, рассмотренный выше. Во втором случае, наоборот, ослабляет его. Поясним это различие на примере. На рис.12а показано поперечное сечение камеры в районе диэлектрической рамки, находящейся между двумя катодными плоскостями и параллельной сигнальным проволочкам. Крайняя сигнальная проволочка $w$ заряжена положительным зарядом с линейной плотностью $\sigma$. Под действием зарядов проволочки происходит поляризация диэлектрика. На его поверхности, обращенной к

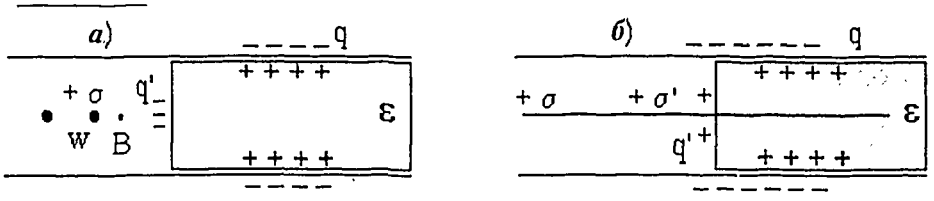


Рис.12. Схема пропорциональной камеры вблизи диэлектрической рамки ε, σ — линейная плотность заряда проволочки, $q$ — поверхностная плотность зарядов катода, $q'$ — поверхностная плотность зарядов рамки за счет поляризации диэлектрика. Сечение камеры плоскостью, перпендикулярной плоскости проволочек (а), $w$ — проволочка. Сечение камеры вдоль проволочки (б), σ′ — линейная плотность заряда проволочки у ее конца

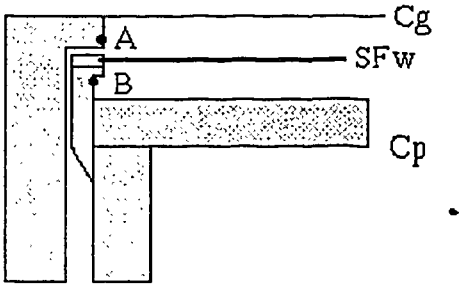


Рис.13. Схема прототипа времяпроекционной камеры. Cg — сеточная поверхность катода, Cp — поверхность катода из медной фольги, SFw — плоскость сигнальных и полевых проволочек детектора, A и B — защитный проволочный электрод. Штриховкой показаны диэлектрические рамки

проволочке, появятся отрицательные заряды $q'$ диполей, образованных из-за поляризации. Направление результирующего поля этих зарядов в точках между проволочкой и рамкой (например, в точке B) будет совпадать с направлением поля заряда проволочки. С увеличением расстояния между проволочкой $w$ и рамкой влияние поляризации диэлектрика уменьшается.

Совсем другая картина наблюдается у концов проволочки. На рис.12б показано сечение камеры вдоль одной из проволочек. Отрицательные заряды катодной плоскости $q$ индуцируют заряды положительного знака с линейной плотностью $\sigma$ вдоль проволочки за исключением ее концов. Вблизи конца проволочки часть зарядов катода, которые индуцировали бы заряды на проволочке в отсутствие диэлектрика, создают поляризацию диэлектрика и связываются положительными зарядами $q'$ на поверхности рамки. Поэтому линейная плотность зарядов $\sigma'$ к концу проволочки уменьшается: $\sigma' < \sigma$. Это ведет к ослаблению краевых эффектов, связанных с увеличением линейной емкости проволочек на ее концах.

Насколько существенно влияние конструктивного решения на характер электрического поля, можно судить по экспериментальным результатам [12]. Эти результаты получены при исследованиях амплитудного распределения сигналов вдоль сигнальной проволочки в прототипе времяпроекционной камеры установки DELPHI [13,14]. Регистрирующим устройством в этом прототипе является пропорциональная камера с тем отличием от рассмотренной выше, что в одной плоскости SFw (рис.13) с сигнальными проволочками между ними размещены полевые проволочки. Их назначение — формирование необходимой конфигурации и величины электрического поля. Одной из катодных плоскостей камеры служила медная фольга Cp, другой плоскостью служила сетка Cg из проволочек, находящихся на расстоянии 1 мм. Расстояние между катодными плоскостями равно 8 мм. Высокое напряжение (+ 1550 В) подавалось на сигнальные проволочки. Катод и полевые проволочки находились под нулевым потенциалом. Коррекция электрического поля у концов сигнальных проволочек осуществлялась подачей напряжения на защитный электрод, которым служили две проволочки *A* и *B* (рис.13). Диаметр проволочек равен 0,8 мм. Без защитного электрода уменьшение амплитуды сигнала более чем на 40% начиналось на расстоянии 4 мм от рамки. Без подачи напряжения на электрод такое уменьшение амплитуды сигнала начиналось на растоянии 1,5 мм от рамки, при отрицательном напряжении, равном 180 В, — только на проволочке *A* и нулевом потенциале на проволочке *B* — на расстоянии 0,3 мм от рамки. Подача напряжения на электрод *B* не приводила к дальнейшим изменениям. При использовании электрода, образованного только проволочкой *A*, эти расстояния увеличивались на 1 мм. Таким образом электрод *A* в большей степени корректировал величину и характер электрического поля, создаваемого катодной сеткой, чем электрод *B*.

## 5. Выводы

Из расчетов конфигурации электрических полей и потенциалов планарных МППК получены следующие результаты, а также сделаны выводы.

— Выявлена причина появления краевых эффектов. Краевые эффекты вызываются изменением линейной плотности заряда крайних проволочек и концевых участков всех проволочек камеры по сравнению с линейной плотностью заряда проволочек центральной области камеры.

— Определена область камеры, в которой краевые эффекты играют заметную роль. Эта область расположена по периметру камеры, она не превышает по ширине $10 \div 15$ мм. Область, в которой краевые эффекты играют заметную роль, не зависит от размеров камеры.

— Показана роль проволочек увеличенного диаметра, используемых в пропорциональных камерах на ее краях. Увеличение диаметра проволочек уменьшает электрическое поле на их поверхности до значения, не превышающего поля остальных проволочек, хотя линейная плотность заряда крайних проволочек увеличенного диаметра больше линейной плотности заряда крайних проволочек одинакового диаметра. Увеличенный заряд крайних проволочек улучшает конфигурацию электрического поля на краях камеры.

## Литература

1. Charpak G. et al. — Nucl. Instr. and Meth., 1968, 62, p.262;
   Charpak G. et al. — Nucl. Instr. and Meth., 1970, 80, p.13.
2. Charpak G. — Ann. Rev. Nucl. Sci., 1970, 20, p.195.
3. Rice-Evans P. — Spark, Streamer, Proportional and Drift Chambers. Richelieu Press, London, 1974.
4. Research on Particle Imaging Detectors (edited by Georges Charpak). Series in 20th Century Physics, vol.6. World Scientific, Singapore, 1995.
5. Glässel P. — Nucl. Instr. and Meth., 1970, 140, p.61.
6. Erskine G.A. — Nucl. Instr. and Meth., 1972, 105, p.565.
7. Tomitani T. — Nucl. Instr. and Meth., 1972, 100, p.179.
8. Symm G.T. — Nucl. Instr. and Meth., 1974, 118, p.605.
9. Veres I., Montvai A. — Nucl. Instr. and Meth., 1978, 156, p.73.
10. Morse P.M. — Methods of Theoretical Physics, Part 2, 1953, New York.
    Buchholz H. — Elektrische und Magnetische Potentialfelder, 1957, Springer, Berlin.
11. Sauli A. — Preprint CERN 77-09, 1977.
12. Brand C. et al. — Nucl. Instr. and Meth., 1985, A237, p.501.
13. Brand C. et al. — The DELPHI time projection chamber. Nucl. Instr. and Meth., 1989, A283, p.567.
14. The DELPHI Collaboration. The DELPHI detector at LEP. — Nucl. Instr. and Meth., 1991, A303, p.233.

Рукопись поступила 6 декабря 1995 года.

УДК 519.254:517.98

# ON STANDARD AND NONSTANDARD APPLICATIONS OF WAVELET ANALYSIS

*M.V.Altaisky*

We review the present status of wavelet analysis, the method of decomposition with respect to representations of the affine group, which is effectively used everywhere in signal and image processing and is receiving a lot of interest in the context of nuclear physics data analysis. Some results of the application of the wavelet decomposition to the experiments carried out at JINR are presented, and some new possible applications are indicated.

The investigation has been performed at the Laboratory of Nuclear Problems, JINR.

## О стандартных и нестандартных приложениях вейлет-анализа

*М.В.Алтайский*

Вейлет-анализ — метод обработки сигналов и изображений — рассматривается как метод разложений по представлениям аффинной группы. Представлены результаты применения вейлет-анализа к экспериментам, проводимым в ОИЯИ, и возможности некоторых новых приложений.

Работа выполнена в Лаборатории ядерных проблем ОИЯИ.

## 1. Wavelets: An Intuitive Description of the Method

The principal shortcoming of common Fourier analysis is its nonlocality. Due to the uncertainty principle, a signal cannot be localized simultaneously in frequency and time with arbitrary precession. From the practical standpoint this nonlocality is always undesirable. This means that we usually want (*i*) to keep the contribution of low and high frequencies separately reasonable and (*ii*) we want the decomposition of a signal to be robust with respect to small perturbation; both are evidently not the case for the Fourier decomposition

$$\hat{f}(\omega) = \frac{1}{\sqrt{2\pi}} \int_{-\infty}^{\infty} e^{i\omega x} f(x)\, dx. \tag{1}$$

To overcome this difficulty the *windowed Fourier transform* [1]

$$\hat{f}(\omega, \tau) = \int_{-\infty}^{\infty} e^{i\omega x} f(x)\, \overline{W}(x-\tau)\, dx \tag{2}$$

was suggested by D.Gabor in 1946 for the purposes of signal processing. Unfortunately, there are some faults with this idea. Transform (2) is evidently poor in resolving wavelengths longer than the window $W(x)$ width. Conversely, the decomposition of short, but high frequency signals requires a broad window with a large number of cycles. The process of reconstruction in this case contains a large number of terms with comparable amplitudes and hence turns out to be numerically unstable.

Conspicuously, what one needs is a scheme with a broad window for low frequency signals and a narrow window for high frequency signals. Such a scheme, independently developed by several authors at the beginning of 1980s [2], is called a wavelet transform. Practically, it is a separate convolution of the signal in question with a family of functions obtained from some basic one — basic wavelet — by shifts and dilatations:

$$T_\psi(a, \tau) f = \int_{-\infty}^{\infty} \overline{\psi}_{a,\tau}(x) f(x)\, dx, \tag{3}$$

where

$$\psi_{a,\tau}(x) = \frac{1}{\sqrt{a}} \psi\left(\frac{\tau - x}{a}\right)$$

are usually referred to as (*affine*) *wavelets*.

## 2. Mathematical Background

Being a quasi-local integral transform, affine wavelet decomposition (3) has found a lot of practical applications to signal processing. In parallel with practical development it has found a profound and abstract theoretical background in the Lie group theory [3]. In the present paper we start with its general properties and only then turn to applications and implementation.

Let us consider a Hilbert space $\mathcal{H}$ with transitive action of a Lie group $G$ on it. Let $U$ be a continuous square-integrable unitary representation of $G$. The vector $\psi \in \mathcal{H}$ is said to be admissible (with respect to $G$), if

$$\int_G |\langle \psi, U(g)\, \psi \rangle|^2 \, d\mu_L(g) < \infty,$$

where $d\mu_L(g)$ is a left-invariant measure on $G$.

The key result which allows decomposition of an arbitrary vector $v \in \mathcal{H}$ with respect to the representation $U(g)$, $g \in G$, is summarized by the following theorem[1] [4].

**Theorem 1.** *Let $U$ be a square-integrable unitary representation of a separable locally compact group $G$ (with left Haar measure $d\mu_L$) on the Hilbert space $\mathcal{H}$, and let $\psi \in \mathcal{H}$ be an admissible vector. Let*

$$C_\psi = \| \psi \|^{-2} \int_G |\langle \psi, U(g)\, \psi \rangle|^2 \, d\mu_L(g) < \infty \tag{4}$$

*($\| \cdot \|$ – $L^2$-norm is implied).*

[1] Here we present the weak form of the theorem. In general, the unitarity is not strictly required.

*Then for all* $v \in \mathcal{H}$ *the following decomposition holds (the integrals converging weakly)*

$$v = C_\psi^{-1} \int_G \langle v, U(g)\,\psi\rangle\, U(g)\,\psi d\mu_L(g). \tag{5}$$

Thus, to acquire good analytical properties, we must require the window integral transform (3) to have the form (5).

Considering a Hilbert space of square integrable functions (of one variable, for simplicity) $L^2(R)$ with transitive action of the affine group

$$G: x \to x' = ax + b, \tag{6}$$

$$(ab) \circ (a',b') = (aa', ab' + b), \tag{7}$$

we define the representation $U(g)$ as

$$[U(a, b)\,\psi](x) = \frac{1}{\sqrt{a}}\,\psi\left(\frac{x-b}{a}\right) \tag{8}$$

and the left invariant measure in the form

$$d\mu_L(a, b) = \frac{da\,db}{a^2},$$

which follows from (7).

For the case of affine group (6), which is in question in the present paper, it is convenient to evaluate the normalization constant $C_\psi$, defined by (4) in Fourier representation[2]; the substitution

$$\psi(x) = \frac{1}{\sqrt{2\pi}} \int e^{-i\omega x}\,\tilde{\psi}(\omega)\,d\omega$$

and (8) into (4) after a straightforward calculation gives

$$C_\psi = 2\pi \int \frac{|\tilde{\psi}(\omega)|^2}{|\omega|}\,d\omega < \infty, \tag{9}$$

while the tranform itself has the form:

$$T_\psi(a, b)\,f = C_\psi^{-1/2} \int \frac{1}{\sqrt{|a|}}\,\psi\left(\frac{b-t}{a}\right) f(t)\,dt, \tag{10}$$

$$f(t) = C_\psi^{-1/2} \int\int \frac{1}{\sqrt{|a|}}\,\psi\left(\frac{t-b}{a}\right) [T_\psi(a, b)\,f]\,\frac{da\,db}{a^2}. \tag{11}$$

[2]Here and after the representation $U(a, b)\,\tilde{\psi}(\omega) = \sqrt{|a|}\,\tilde{\psi}(a,\omega)\exp(i\,\omega b)$ is useful to simplify calculations.

## 3. Basic Properties

The pair of a direct and an inverse wavelet transform (10,11) taken together with the admissibility condition (4) still leaves us considerable freedom in the choice of analysing wavelet $\psi$. Practically, the admissibility condition (4) taken in the Fourier representation (9) means the vanishing behaviour of $\tilde{\psi}(\omega)$ in the neighbourhood of $\omega = 0$; which can be redundantly satisfied if $\psi(0) = 0$ is implied; the latter, in turn, means

$$\int \psi(t)\, dt = 0. \tag{12}$$

The latter equation provides the insensibility of wavelet transform to a constant shift of the function in question

$$[T_\psi(a, b)](f + \text{const}) = [T_\psi(a, b)] f.$$

The simplest choice of analysing wavelet satisfying the condition (12) is the so-called Haar wavelet:

$$\psi(x) = \begin{cases} 1 & \text{for } 0 < x < 1/2 \\ -1 & \text{for } 1/2 \le x < 1 \\ 0 & \text{elsewhere .} \end{cases}$$

The Haar wavelet, being the simplest one for numeric implementation, has got a lot of applications, mainly in image and signal processing, which we consider later in this paper. The next straightforward generalization of the condition (12) is the vanishing momenta requirement

$$\int dx x^m \psi(x) = 0, \quad \forall m, 0 \le m < n; n \in Z.$$

This requirement gives rise to a family of vanishing momenta Gaussian wavelets [5]

$$g_n(x) = (-1)^{n+1} \frac{d^n}{dx^n} e^{-x^2/2}, \quad n > 0. \tag{13}$$

In Fourier space $\hat{g}_n(\omega) = -(i\omega)^n e^{-\omega^2/2}$ has a zero of order $n$ in $\omega = 0$.

In this family the first two wavelets are most popular: $g_1(x) = -x \exp\left(-\frac{x^2}{2}\right)$, which is antisymmetric and thus suitable for some statistical applications to be considered later, and the Maar wavelet $g_2(x) = (1 - x^2) \exp\left(-\frac{x^2}{2}\right)$, often called the «Mexican hat».

The normalization constant $C_{g_n}$, which can be easily calculated in the Fourier space, for the family of vanishing momenta wavelets (13) is

$$C_{g_n} = 2\pi(n-1)!$$

Among the other wavelets, the difference of two Gaussians

$$\psi_b(x) = e^{ibx}e^{-x^2/2} = \sqrt{2}\, e^{-b^2/4}e^{ibx}e^{-x^2},$$

considered in the pioneering work [6] should be mentioned.

Another property of wavelet analysis provided by (8), is that a dilated wavelet has the same energy as the original one

$$\int \left| \frac{1}{\sqrt{a}} \psi\left(\frac{t}{a}\right)\right|^2 dt = \int |\psi(t)|^2 dt.$$

Since the energy is conserved under dilatations, wavelet analysis is equally sensitive to the contributions of low and high frequency bands. It is its great advantage, say in comparison to Gabor expansion. The dilatation parameter $a$ here has a plain interpretation: if $\psi(t)$ is a sound recorded on a tape, then $a^{-1/2}\psi(t/a)$ with $a=2$ is the sound obtained by replaying the tape at half speed.

The (global) energy conservation law also holds:

$$\int |f(t)|^2 dt = \int |T_\psi(a,b)f|^2 \frac{da\, db}{a^2}.$$

Among other properties of the wavelet transform we should indicate its property under scale transform:

$$[T_\psi(a,b)]f(\lambda t) = \lambda^{-1}[T_\psi(\lambda a, \lambda b)]f(t).$$

We should also mention that in numerical implementations the decomposition of a unity

$$\hat{1} C_\psi = \int_G U(g)\,|\psi\rangle\, d\mu_L(g)\, \langle\psi|\, U^*(g),$$

which follows from general formula (5), turns out to be a sum over a discrete frame

$$A\hat{1} \le \sum_j |\psi_j\rangle\langle\psi_j| \le B\hat{1},$$

where $A, B > 0$ are some positive constants. This basis, nonorthogonal and redundant in general, ensures the stability of the wavelet transform: local perturbations of wavelet coefficients cause only local perturbation of the image.

## 4. Applications to Signal Analysis and Synthesis: First View

As was mentioned in previous section, the dilatation of a wavelet with a factor $a \approx 2$ corresponds to the half speed playback of a tape or to one octave down shifts. Evidently, any musical melody remains recognizable after a global shift by an integer number of octaves. This fact makes the wavelet transform a credible tool in acoustics, speech processing and music.

For practical applications it is convenient to use some particular forms of the integral transforms (10), (11). Here we list these transformations following [6].

1. *Voice transform of f* with respect to $\psi$ is a wavelet transformation (10) taken on the logarithmical scale.

$$(Z_\psi^\pm)[f](b, u) = \frac{2^u}{k_\psi} \int \psi(\pm 2^u(b-t))\, f(t)\, dt, \tag{14}$$

where $k_\psi = \frac{\sqrt{2\pi}}{\ln 2} \cdot \int \frac{\tilde{\psi}(\omega)}{|\omega|} d\omega$. The scale factor 2 is chosen for fast numerical implementation.

The voice transform allows an elegant way to represent inverse formula (11) in the form of an octave series

$$f(t) = \int [(Z_\psi^+ f)(t, u) + (Z_\psi^- f)(t, u)]\, du$$

or $f(t) = \sum_{n=-\infty}^{\infty} f_n^+ + f_n^-$, where $f_n^\pm(t) = \int_n^{n+1} (Z_\psi^\pm f)(t, u)\, du$.

2. Another useful representation, which has some advantages being not expensive in memory space, is known as a *cycle-octave representation*

$$(C_\psi^\pm f)(v, u) = \frac{2^{-u}}{k_\psi} \int \psi\,(\pm (v - 2^u t))\, f(t)\, dt.$$

Practically, instead of basic representation (10), (14) the Fourier representation is often used

$$(T_\psi f)(b, a) = C_\psi^{-1/2} |a|^{1/2} \int e^{i\omega b}\, \tilde{\psi}\,(\omega a)\, \tilde{f}(\omega)\, d\omega \tag{15}$$

and

$$(Z_\psi^\pm f)(b, u) = k_\psi^{-1} \int e^{i\omega b}\, \tilde{\psi}(\pm 2^u\, \omega)\, \tilde{f}(\omega)\, d\omega,$$

respectively. This provides a possibility of using FFT and FFT-like algorithms.

## 5. Wavelets and Fractals

The best way to study any physical problem with known symmetry is to build a functional basis with the symmetry as close to that of the problem as possible. For this reason a system of spherical functions is the best one to fit the problem with spherical ($SO_3$) symmetry, while Fourier decomposition is apt to the problems invariant under translations.

The matter turns out to be even more conspicuous when one studies fractals — singular (nondifferentiable) self-similar objects [7]. On the one hand, the invariance under scale transformations (or self-similarity) is the symmetry group the *WT* is based on; on the other, with no requirements of differentiability the wavelet analysis seems to be an ultimate tool to study singular objects. In standard multifractal analysis, the properties of these singular objects are considered in terms of a (singular) measure $\mu$, singularity spectrum of this measure $f(\alpha)$ and the power behaviour of a partition function

$$Z(l, q) = \sum_i (\mu_l)_i^q \sim l^{\tau(q)}; \quad \mu_l(x_0) \sim l^{\alpha(x_0)},$$

where the sum is taken over all disjoint intervals of size $l$, containing the points of the considered fractal set; $(\mu_l)_i$ is the measure of the $i$-th interval. The power behaviour of the partition function is characterized by some function $\tau(q)$ related to $f(\alpha)$ and expressed via fractal dimension

$$D_q = \frac{\tau(q)}{q-1}.$$

For a globally self-similar object (monofractal) $D_q = D_0$ does not depend on $q$

$$\alpha = f(\alpha) = D_q = D_0, \forall_q.$$

To perform wavelet decomposition of a singular measure $\mu(x) = \int_0^x d\mu$ it is convenient to use the vanishing moment wavelet family (13).

The measure $\mu(x)$ can be represented via its wavelet transform

$$\mu(x) = C_g^{-1/2} \int_0^\infty \frac{da\, db}{a^2} \frac{1}{\sqrt{a}} g\left(\frac{x-b}{a}\right) T_g(a, b).$$

An arbitrary function $g(x)$, cannot be used as a basic wavelet — it is required to satisfy the admissibility condition (4). This restriction, however, is rather loose, and allows one to choose a wavelet within a large variety of admissible functions, say from the family (13). This redundancy is undoubtedly of great benefit for the analysis of fractal structure. It provides us with a powerful mathematical microscope with magnification $a^{-1}$ and dispensable optics labelled by $n$.

To illustrate this, we can consider the «devil's staircase» — a singular measure of the triadic Cantor set shown in Fig.1. The maxima of its wavelet transform $T_g(a, x)\,\mu$, shown in Fig.2, exactly resemble the structure of the original set.

Besides the graphic facilities, a number of useful theorems provide a basis for analytical studies of fractal objects via wavelets. Roughly speaking, the analytical treatment is based on the fact that the collection of all wavelet transform maxima contains complete information on the measure in question.

Some useful results are listed below:

- **Theorem 2** (*Holshneider*, [8]). *Let* $\mu$ *be a bounded locally integrable function such that*

$$\mu(x) - \mu(x_0) = 0(|x - x_0|^h), \quad h \in [0, 1]$$

*then*

$$T_g(a, x) = O(a^{h+1/2}) \tag{16}$$

*inside the cone* $|x - x_0| \le \text{const}$.

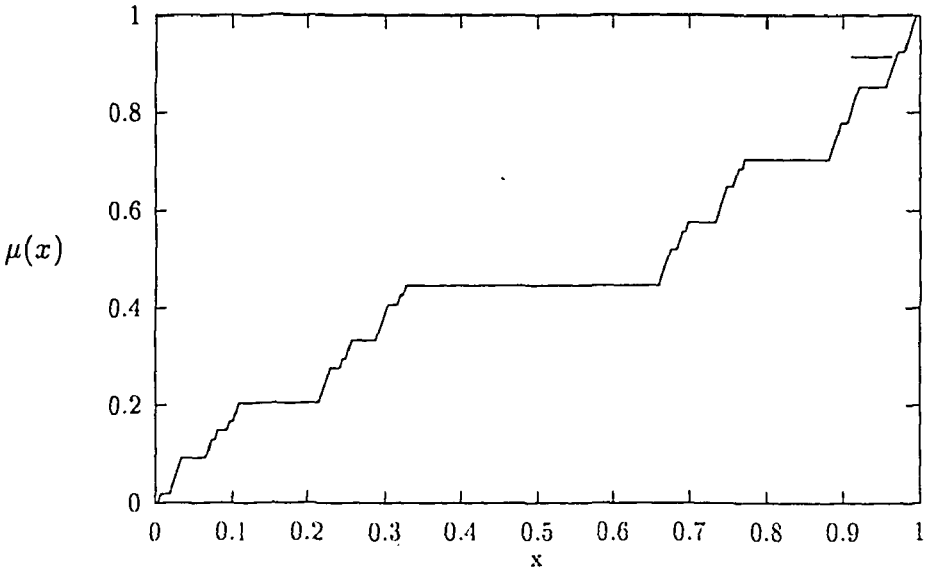


Fig.1. «Devil's staircase» — a singular measure of the triadic Cantor set

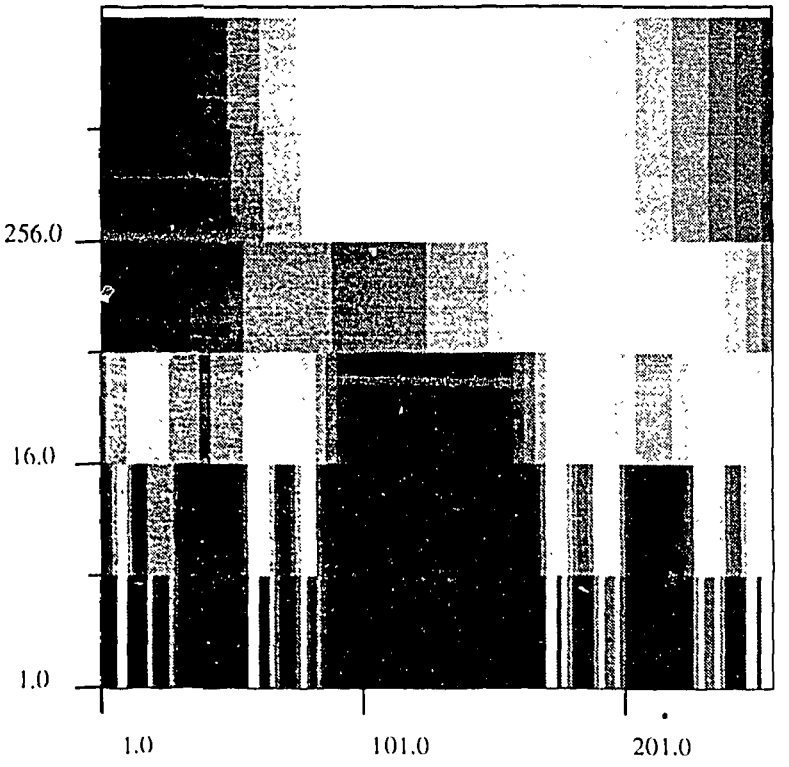


Fig.2. Wavelet coefficients for a «devil's staircase» taken with $g_1$-wavelet

- The partition function can be constructed directly on the set of wavelet coefficients:

$$Z(a, q) = \sum_{\text{over all maxima: } \{x, (a)\}} |T_g(a, x)|^q.$$

The power behaviour of the measure can be derived from this equation like free energy in thermodynamics $\tau(q) = \lim_{a \to 0} \frac{\ln Z(a, q)}{\ln a}$.

## 6. Wavelets in Biology

The analysis of DNA sequences is one of the principal branches of modern cellular biology. It was shown in a number of recent studies that the distribution of nucleotides $A$, $T$, $C$, $G$ in a real DNA chain is a fractal one. Thus, the fractal and multifractal tools can be applied. Wavelet analysis is an indispensible tool in this relation.

In general, the occurrence of a certain nucleotide in a certain position of the DNA chain, labeled by a length parameter $l$, can be described as a random process $X(l, \cdot)$. Thus, for the case of the above-mentioned 4-letter alphabet, we deal with a probability space $(\Omega, \mathcal{U}, P)$, with $\Omega = \{A, T, C, G\}$ and a family of four random processes

$$X_z = \{X_z(l, \omega); l \in R, \omega \in \Omega\},$$

such that

$$X_z(l, \omega) = \begin{cases} 1 & \text{if } \omega = z \\ 0 & \text{otherwise.} \end{cases}$$

Instead of calculating correlations, as was done in [9], we proceed with the integral measures

$$\mu_z(s) = \int_0^s X_z(l, \omega)\, dP(\omega)\, dl \equiv \int_0^s d\mu_z, \tag{17}$$

which count the total number of each of the nucleotides $z = A, T, C, G$ up to the $l$-th position in the chain.

Since the measures in question (17) are supposed to be generally nondifferentiable, we first have to study their scaling behavior $\mu(x) - \mu(x_0) \approx |x - x_0|^h$.

The extraction of the Lipschitz—Hölder exponent $h$ from the experimentally obtained measure is a typical problem in physics of fractals, in DNA study this was performed in the same way, using the scaling theorem [8] for the function $\mu(l)$ (see eq.16). The details of the method can be found in [10]; hereafter we present the main results obtained in [10] with the help of the $g_2$-wavelet.

For the DNA sequence of Chinese Hamster cells [11] with the length of 11838 nucleotides the middle-data section of wavelet coefficients gives the scaling exponents $h$.

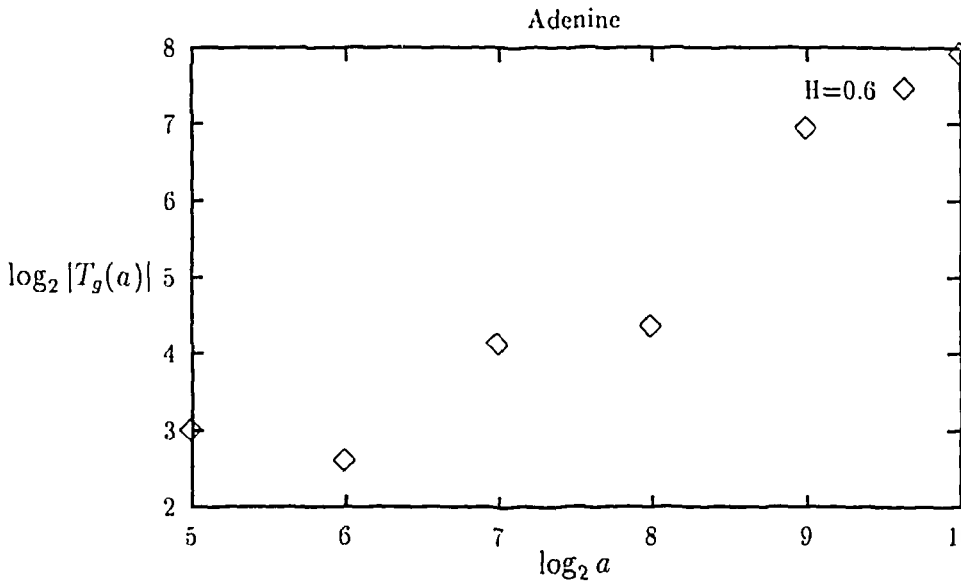


Fig.3

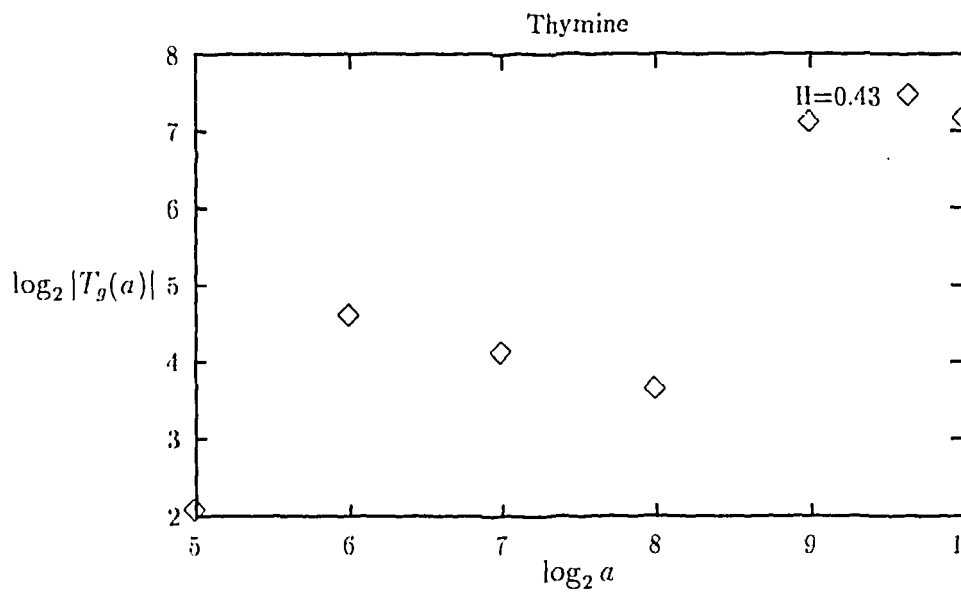


Fig.4

Figs.3—6. The dependence of (binary logarithms of) $g_1$-wavelet coefficients for the measure functions taken at the middle of the data for the adenine, thymine, cytosine and guanine, respectively. The values of the Lipschitz–Hölder exponents presented in the pictures were obtained with the best line approximation

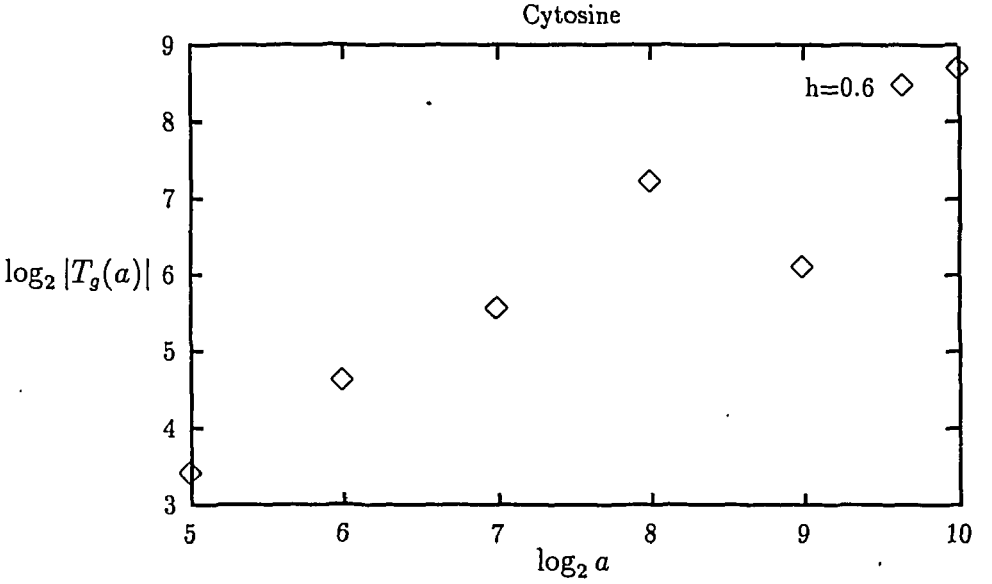


Fig.5

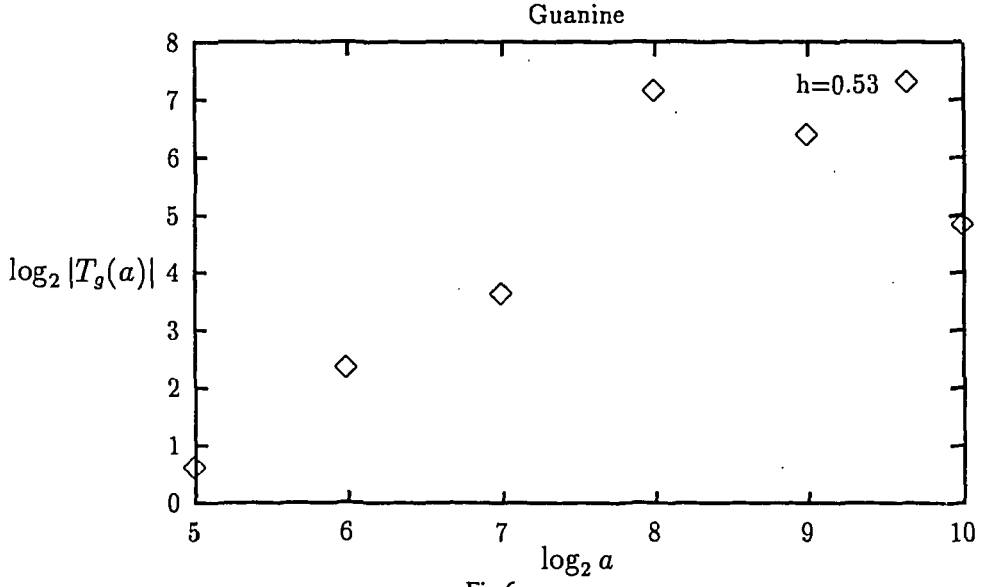


Fig.6

The logarithmic plots $\log_2 |T_g(a,x)|$ for the measures $\mu_a$, $\mu_t$, $\mu_c$, $\mu_g$ are presented in Figs.3—6. The plots were obtained at the middle of the range, $x_m = 4096$; however the behaviour of the sections at other points is not seriously different. The corresponding Lipschitz-Hölder exponents are presented in the table.

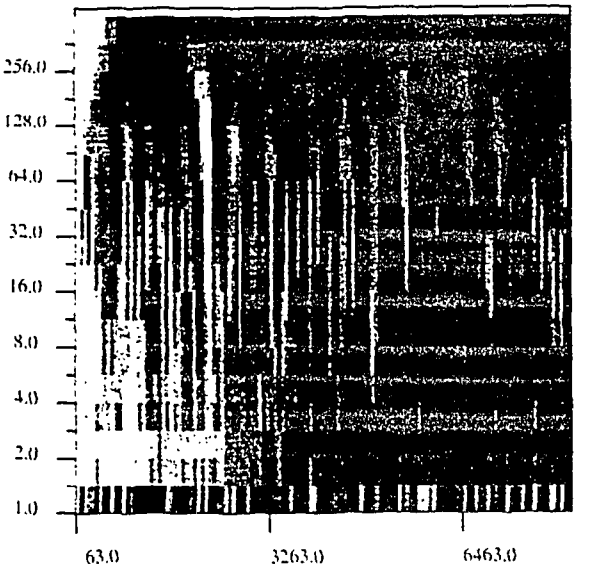


Fig.7

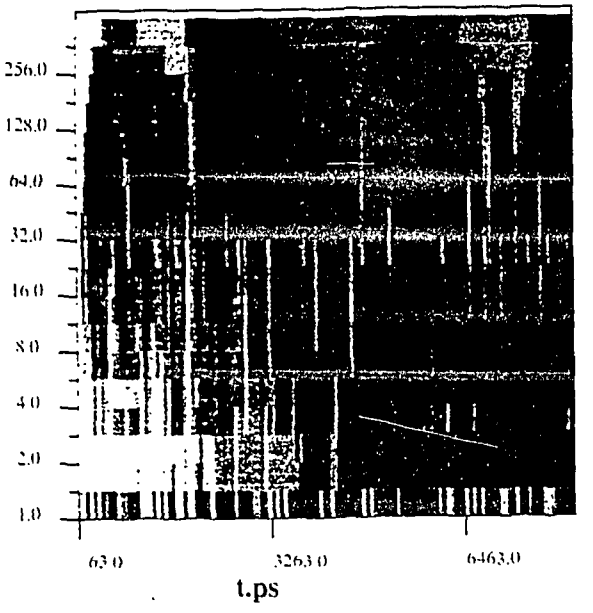


Fig.8

Figs.7—10. The grey density plots of wavelet coefficients (up to $2^{10}$ power scale) for the adenine, thymine, cytosine and guanine, respectively. The fragmentation processes clearly distinguish at $2^6$, $2^7$ and $2^9$ scales

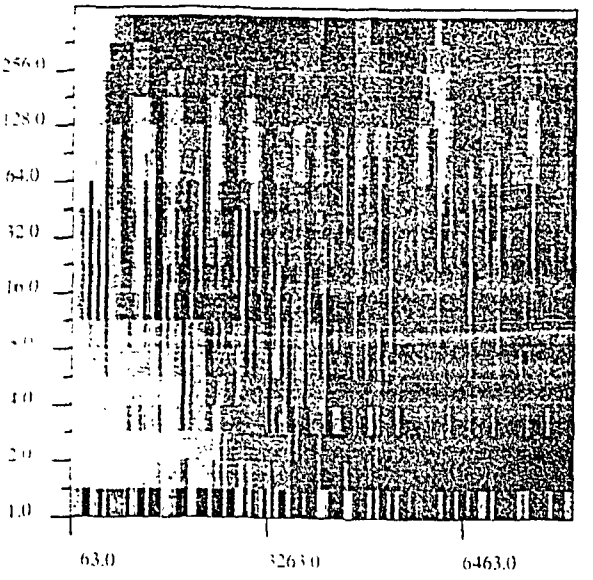


c.ps

Fig.9

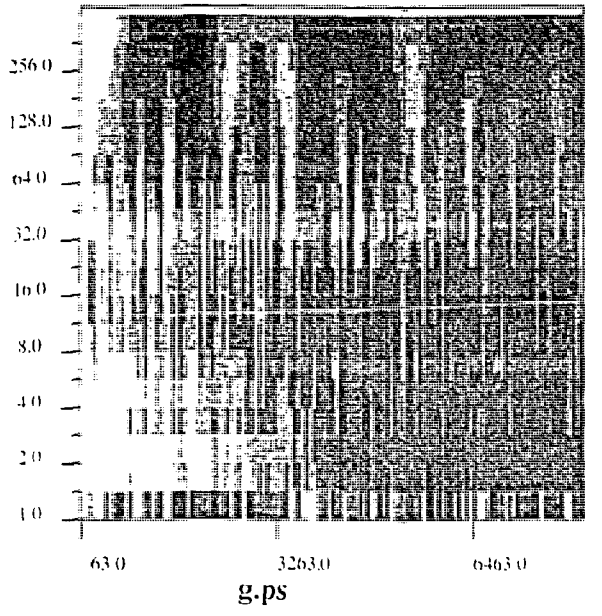


g.ps

Fig.10

| $h_A$ | $h_T$ | $h_C$ | $h_G$ |
|---|---|---|---|
| 0.60 | 0.43 | 0.60 | 0.53. |

These coefficients are conspicuously close to the $h_B = 1/2$ of the Brownian motion, the purely random process. However, the difference $h_z - h_B$, where $z = A, T, C, G$, which has the magnitude of several per cent, cannot be regarded as vanishing. This difference can be caused by branching processes which can be clearly seen in the density plots of wavelet coefficients, at scale approximately equal to $2^7$ or $2^8$, see Figs.7—10.

Thus, we conclude that the scaling in DNA chains does really exist. This scaling is of multifractal nature (see, e.g., [11]) rather than global one.

As an auxiliary result, we can mention that the color-density representation of wavelet coefficients which proved to be a powerful tool for the analysis of general fractals seems to be of great use for identifying branching processes in nucleotide chains as a computer graphic tool.

## 7. Wavelets in Nuclear Physics

Up to now the most common applications of WT belonged to either turbulence data analysis, where scaling is an inherent feature of fluid physics, or to image processing, where the singularity detection and local reconstruction are significant.

Recently a lot of interest was attracted to possible applications of wavelets in both theoretical and experimental nuclear physics. The main merits of wavelets valuable for experimental data processing are:

- Firstly, since the works of Zimin, WT proved to work efficiently in situations where cascade processes play a significant role. Therefore, if the measure $\mu(x)$ describes an event number at a certain point $x$, ($x \in R^3$ in general), then the search for *jet* events can be performed with the aid of WT, in a way similar to the «devil's staircase» singularity reconstruction (See, e.g., [7,10] for details).
- In the simplest one-dimensional case, $x \in [0, 2\pi]$ can be taken for the angular coordinate of the detector; the WT can be regarded as a microscope with variable angle resolution.
- Secondly, if $x$ is regarded as time (or energy), WT works as a tool for studying time (or energy) scaling of the process described by time (or energy) event density $\mu(x)$.
- Thirdly, being local in both $x$ and Fourier space, WT can provide more information in spectral problems, where Fourier methods fail or work insufficiently.
- The contributions of different frequency bands to WT are kept reasonable separated. This separation is achieved with quite insignificant loss of resolution in time variable (if a signal is considered). That's why the reconstruction is «robust» in the sense of being stable under small perturbations, which enables one to distinguish between «useful» low bands (in Fourier space) and contributions of close high frequencies $\omega_1 - \omega_2 \approx 0$ usually generated by noise.

From the theoretical point of view the possible applications of wavelets are even more appealing, since the wavelet transform is based on the scaling symmetry — one of the most important symmetries in physics. Here we mention a few facts related to self-similarity which could be studied with the help of wavelets [12]:

- *Local Parton Hadron Duality* [13], i.e., the similarity between momentum spectra of hadrons and those of partons. This similarity, which is closely related to $n$-parton correlations and multiplicity moments behaviour in phase space, has been studied in [14].
- The fractal behaviour of final multiparton states [16] was studied by several authors. They calculated the fractal dimension directly from multiplicity distribution moments and study the entropy of secondary particles

$$S = -\sum_n P_n \ln P_n ,$$

where $P_n$ is the probability of having «$n$» produced particles in the final state [17]. They found the scaling behaviour, but, as the method was rather rough (see [7] for the shortcomings of the fractal dimension calculations without wavelets), rare, but interesting events could be lost.

- Recently, fractal analysis of multiparticle production in hadron-hadron collisions has been done by other authors [15].

All these studies evidently admit the application of wavelet transform. Recently, the wavelet transform as an image processing method was also applied to separation of secondary particles ($K$-mesons, in particular) in $d$ + Au interactions. Following [12], here we describe the method and results.

## 7.1. Secondary Particle Separation as an Image Recognition Problem

*7.1.1. Problem.* The wavelet method has been applied to the processing of time-of-flight vs. energy data plots obtained from $d + \mathrm{Au} \to \ldots$ — reactions in experiments carried out at the Nuclotron using the internal target at a deuteron momentum of 3.8 GeV/c in March 1994.

In Fig.12 the mass spectrum of the primary data obtained by standard method of comparing the time of flight and the energy

$$\beta = \frac{v}{c} = \frac{l}{tc} = \sqrt{\frac{E^2 - m^2}{E^2}} \qquad (18)$$

is presented.

Due to the presence of both $\pi$-mesons and protons ($E \sim 250$ MeV), which dominate in the central region of the E vs. TOF plot, Fig.11, it is difficult to distinguish other events in this region. Besides, high energy protons ($E > 400$ MeV) due to decreasing energy loss give a contribution mainly to the low energy region about 200 MeV.

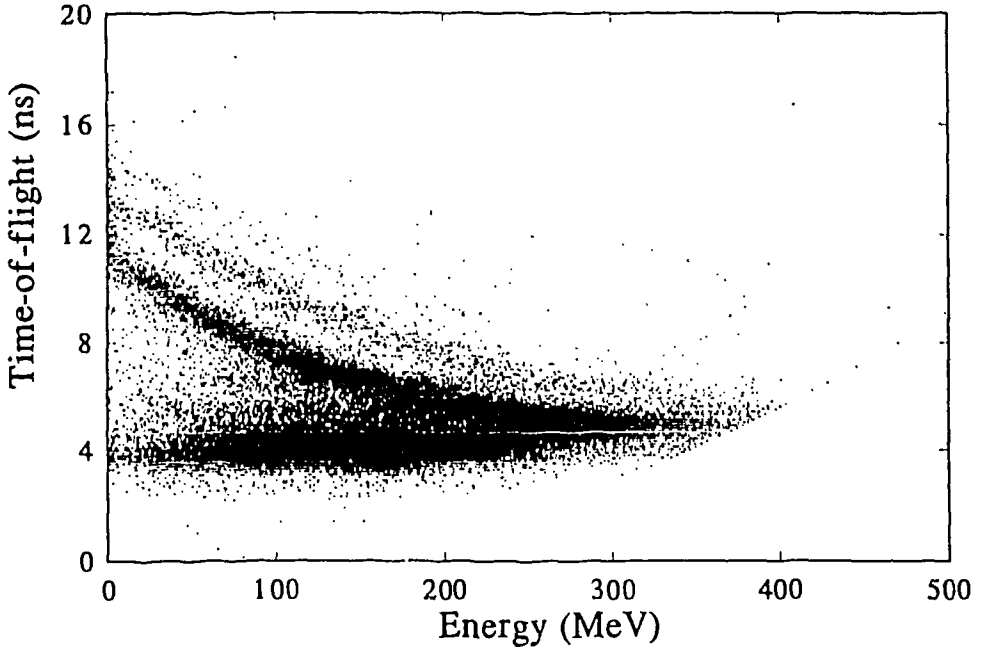


Fig.11. E vs. TOF plot of primary experimental data

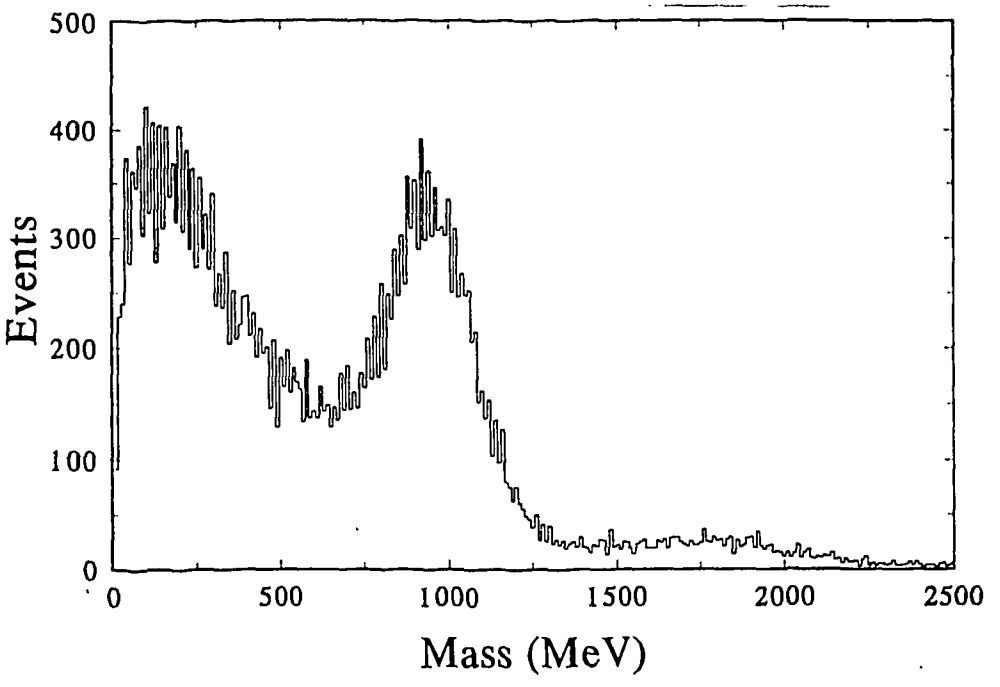


Fig.12. Spectrum of reconstructed mass obtained from primary data

*7.1.2. Algorithm.* The main idea of implying a wavelet analysis to investigation of events in nuclear and high energy physics is to use its good properties in separating events from noise. Using wavelet one can look at experimental data with various resolution. This can be used to search for tracks of particles and different kinds of events, etc.

To use a multiresolution analysis [18] one should choose a family of closed subspaces $V_m \subset L^2(R)$, $m \in Z$, such that

1. $f(x) \in V_m \Leftrightarrow f(2*x) \in V_{m-1}$

2. $\ldots \subset V_2 \subset V_1 \subset V_0 \subset V_{-1} \subset V_{-2} \subset \ldots$,

$\cap V_m = 0, \quad \cup V_m = L^2(R)$

3. there is a $\varphi \in V_0$ such that its linear integer translations $\varphi_n^0(x) = \varphi(x+n)$ constitute a basis in $V_0$ (consequently, functions $\varphi_n^m$ constitute a basis in $V_m$),

4. there exist $0 < A \le B < \infty$, such that for all $(c_n)_{n \in Z} \in l^2(Z)$,

$$A \sum_n |c_n|^2 \le \| \sum_n c_n \varphi_n^m \|^2 \le B \sum_n |c_n|^2.$$

The orthogonal projections of a function which we analyse on a chain of subspaces $V_m$ represent snapshots of this function with different resolution. Choosing an appropriate basic function $\varphi$, one could select different kinds of snapshots.

To make the decomposition close, one should also define a chain of subspaces $W_m$ orthogonal to $V_m$, such that

$$V_{m-1} = V_m \oplus W_m . \tag{19}$$

The coefficients of a projection on $V_m$ and $W_n$ are

$$s_n^m = \int f(x)\, \varphi_n^m(x)\, dx, \quad d_n^m = \int f(x)\, \psi_n^m(x)\, dx, \tag{20}$$

where in a discrete case a sum is implied. For the simplest case of the Haar wavelet the basic functions are:

$$\varphi_k^j(x) = \begin{cases} |I_k^j|^{-1/2} & \text{for } x \in I_{j,k} \\ 0 & \text{elsewhere,} \end{cases} \tag{21}$$

$$\psi_k^j(x) = \begin{cases} 2^{-j/2} & \text{for } 2^j(k-1) < x < 2^j(k-1/2), \\ -2^{-j/2} & \text{for } 2^j(k-1/2) \le x < 2^j k, \\ 0 & \text{elsewhere} \end{cases} \tag{22}$$

$I_k^j$ denotes the supporter of $j$-th level basic functions

$$I_J \equiv I_k^j = [2^j(k-1), 2^j k].$$

The approximate reconstruction formula has the form

$$P_m f = \sum_n s_n^m \varphi_n^m + \sum_n d_n^m \psi_n^m . \tag{23}$$

In our two-dimensional problem we used a pyramidal scheme with a basis taken in the form of a tensor product

$$h_{I\times J} = (\psi_I \oplus \varphi_I) \otimes (\psi_J \oplus \varphi_J),$$

or explicitly, $\{h_1, h_2, h_3\} = \{\psi_I(x)\,\psi_J(y),\ \psi_I(x)\,\varphi_J(y),\ \varphi_I(x)\,\psi_J(y)\}$. The corresponding coefficients can be easily derived from formulae (20):

$$\begin{aligned}
s^{j+1}_{k_x,k_y} &= s^j_{2k_x-1,2k_y-1} + s^j_{2k_x-1,2k_y} + s^j_{2k_x,2k_y-1} + s^j_{2k_x,2k_y}\\
d^{j+1}_{(1);k_x,k_y} &= s^j_{2k_x-1,2k_y-1} - s^j_{2k_x-1,2k_y} + s^j_{2k_x,2k_y-1} - s^j_{2k_x,2k_y}\\
d^{j+1}_{(2);k_x,k_y} &= s^j_{2k_x-1,2k_y-1} - s^j_{2k_x,2k_y-1} + s^j_{2k_x-1,2k_y} - s^j_{2k_x,2k_y}\\
d^{j+1}_{(3);k_x,k_y} &= s^j_{2k_x-1,2k_y-1} + s^j_{2k_x,2k_y-1} - s^j_{2k_x-1,2k_y} - s^j_{2k_x,2k_y},
\end{aligned}$$

where $s^0$ stand for the primary data.

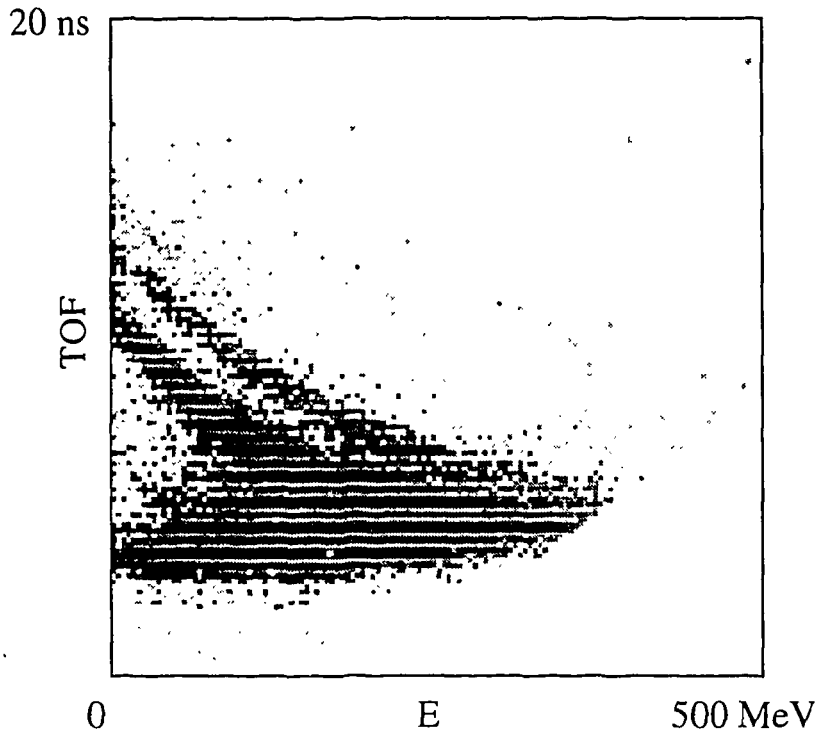


Fig.13. $s^{(1)}$ coefficients plot for the data set of Fig.11

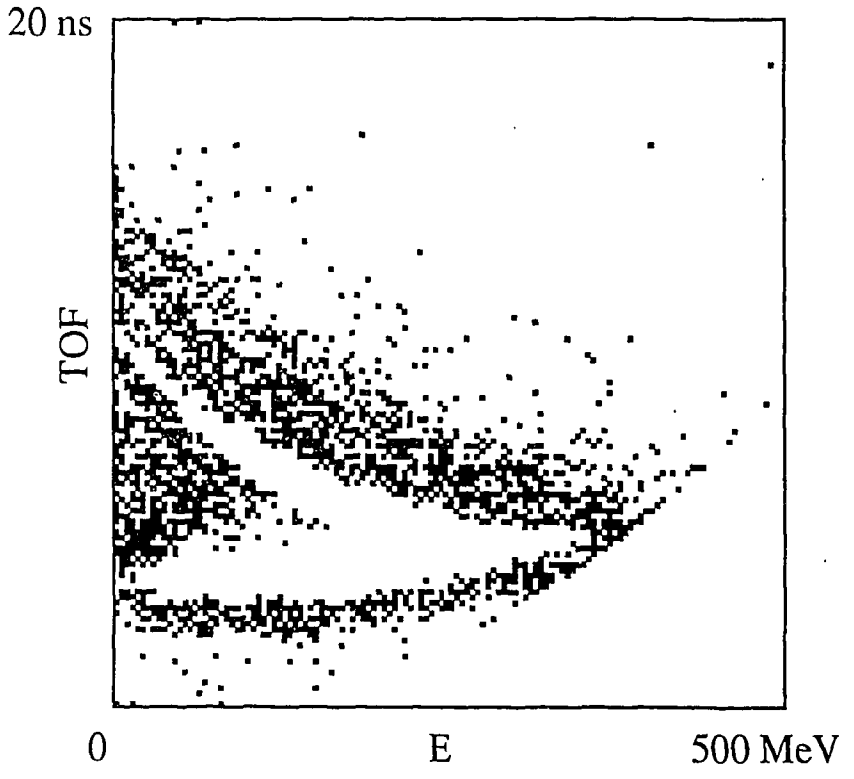


Fig.14. $|d^{(1)}|$ coefficients plot for the data set of Fig.11

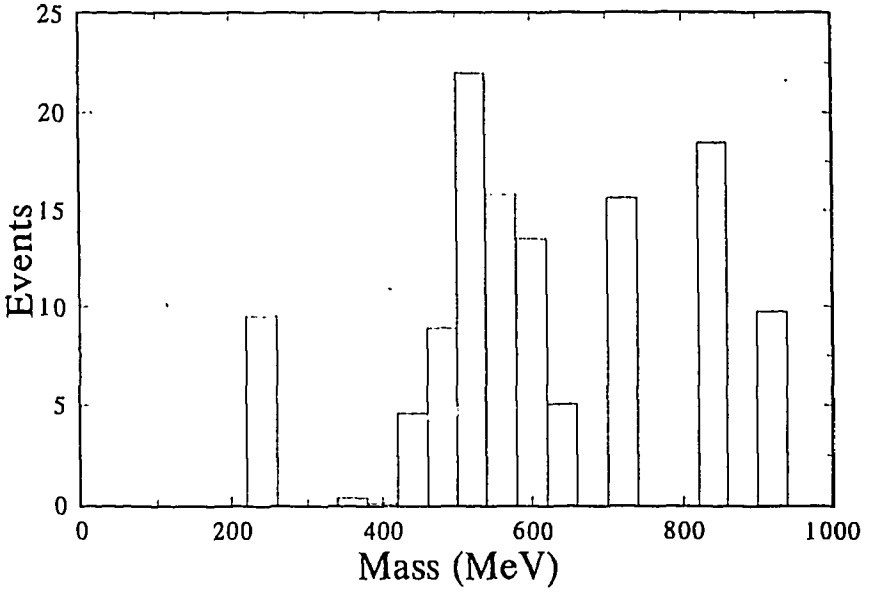


Fig.15. Mass spectrum obtained after filtering

*7.1.3. Results.* The primary data *E—dt*—plot is shown in Fig.11. The *X*-axis corresponds to ADC channel numbers, *Y*-axis to TDC ones. (Both axes are scaled by factor 4). In this plot, against a noisy background we can distinguish two contrast regions: the upper one, which corresponds to secondary protons, and the lower one, which corresponds to π-mesons.

To clear out the contribution of the dominating processes we performed the wavelet analysis. Having calculated the wavelet image (the Haar wavelet was used) of the initial data plot we substracted the central domain, in which $d^{(2)}$ coefficients (See Fig.14) practically vanish.

The resulting mass spectrum is presented in Fig.15. We identify the central peak near 500 MeV, clearly distinguished in mass histogram,with the K-meson contribution.

Besides, sequentially scaling the picture, we can clearly distinguish 4 regions:

- upper right region: secondary deuterons
- two above-mentioned regions
- a *K*-meson branch.

## 7.2. Fitting Distributions with Wavelets

*7.2.1. Problem.* A typical problem of experimental nuclear physics is that of separating several Gaussians which contribute to the same experimentally obtained spectrum. Usually, to cope with this problem, some parametric methods evolving numerical minimization are used. Wavelet decomposition provides a nonparametric method to separate the contributions of several Gaussians [20].

Let us consider an approximation of an experimental data distribution, e.g., a number of particles per channel vs. energy, by the sum of finite number of Gaussian sources

$$f_{\exp}(x) = \sum_k \frac{N_k}{\sqrt{2\pi\sigma_k^2}} \exp\left( -\frac{(x - x_m^k)^2}{2\sigma_k^2} \right), \tag{24}$$

where $\sum_k N_k = N$ is the total number of registered particles.

If we suppose that $f_{\exp}(x)$ is a square-integrable function, the solution of the equation

$$f_{\exp}(x) - \sum_k \frac{N_k}{\sqrt{2\pi\sigma_k^2}} \exp\left( -\frac{(x - x_m^k)^2}{2\sigma_k^2} \right) = 0$$

can be found analytically. Let us start with a single gauss distribution

$$f_{\text{gauss}}(x) = \frac{N}{\sqrt{2\pi\sigma_k^2}} \exp\left( -\frac{x^2}{2\sigma_k^2} \right), \tag{25}$$

where, without loss of generality, we set $x_m^1 = \bar{x} = 0$.

Instead of calculating different moments of the probability distribution we perform wavelet decomposition of the spectrum in question. Since we are going to analyse Gauss distributions, it is natural to choose the analysing function $g$ — the basic wavelet — from the family of vanishing momenta wavelets (13).

It should be mentioned, that $g_0(x)$ does not fit the problem, since $c_{g_0} = \infty$ and the inverse transform (11) is not defined for this case. This fact hints that the direct decomposition of $f_{\exp}$ into the sum of Gaussians is not unique, and hence the problem requires more general system of basic functions.

Prior to study distribution functions with the family of wavelets (13), let us recall some useful formulae

1. The Fourier transform of the $g_n$ family is

$$\tilde{g}_n(k) = -(ik)^n e^{-k^2/2}.$$

2. We can define a formal generating function for the wavelet family $g_n$

$$\tilde{g}(s, k) = \exp(iks - k^2/2), \tag{26}$$

such that

$$\tilde{g}_n(k) = -\left(\frac{d}{ds}\right)^n \tilde{g}(s, k)\Big|_{s=0}. \tag{27}$$

For a single Gaussian distribution (25), to calculate the convolution (10) for an arbitrary basic function from the family $g_n$ we use the generation function (26):

$$(T_{g_n} f_{\text{gauss}})(a, b) = -\left(\frac{d}{ds}\right)^n (T_{g_s} f_{\text{gauss}})(a, b)\Big|_{s=0}, \tag{28}$$

where $g_s$ stands for $g(s, \cdot)$. Substituting (15) into the latter equation, we obtain

$$(T_{g_s} g_{\text{gauss}})(a, b) = N\sqrt{\frac{a}{2\pi c_{g_s}}} \int dk \exp\left(ik(b + as) - \frac{k^2}{2}(a^2 + \sigma^2)\right) =$$

$$= N\sqrt{\frac{a}{c_{g_s}}} \frac{\exp\left(-\dfrac{(b + as)^2}{2(a^2 + \sigma^2)}\right)}{\sqrt{a^2 + \sigma^2}}. \tag{29}$$

The formal normalization constant $c_{g_s}$ should be replaced by concrete $c_{g_n}$ after taking the derivatives.

*7.2.2. Single Source Distribution.* The simplest way to find the distribution parameters for the case of a single Gaussian source is to use the coefficients of its $g_2$ decomposition. Eq. (29) for $n = 2$ leads to

$$(T_{g_2} f_{\text{gauss}})(a, b) = N\sqrt{\frac{a^2}{2\pi}}\left(\frac{a}{a^2+\sigma^2}\right)^{3/2}\left[1-\frac{b^2}{a^2+\sigma^2}\right]\exp\left(-\frac{b^2}{2(a^2+\sigma^2)}\right). \quad (30)$$

Taking the derivative $\partial/\partial_a$ of equation (30) at the central point $b=0$ we find the extremum of the $g_2$ coefficient at a scale

$$a_m = \sqrt{5}\sigma. \quad (31)$$

The value of wavelet coefficient at the extremal point is

$$(T_{g_2} f_{\text{gauss}})(a_m, 0) = \frac{N}{\sqrt{2\pi}\sigma} 5^{5/4} 6^{-3/2} = \frac{N}{\sqrt{2\pi a_m}}\left(\frac{5}{6}\right)^{3/2}. \quad (32)$$

Thus, performing the convolution (10) numerically and finding the maximum of the $g_2$ wavelet coefficient we obtain the dispersion and amplitude of original distribution.

*7.2.3. The Distribution with Two Sources.* If the distribution is a sum of two Gaussians and the localization at least of one of them is known, we can find the other with the help of $g_1$ wavelet.

Without loss of generality we write the analysed function in the form

$$f(x) = \frac{N_0}{\sqrt{2\pi\sigma_0^2}}\exp\left(-\frac{x^2}{2\sigma_0^2}\right) + \frac{N_1}{\sqrt{2\pi\sigma_1^2}}\exp\left(-\frac{(x-x_m)^2)}{2\sigma_1^2}\right). \quad (33)$$

Let us consider the $g_1$-wavelet coefficient at $x=0$. Since the first term of r.h.s. of (33) is symmetric, whether $g_1(x)$ is antisymmetric under the reflection $x \to -x$, the coefficient $(T_{g_1} f)(a, 0)$ depends on the second term of (33) only.

Explicitly,

$$(T_{g_1} f)(a, 0) = N_1 \frac{x_m}{\sqrt{2\pi}}\left(\frac{a}{a^2+\sigma_1^2}\right)^{3/2}\exp\left(-\frac{x_m^2}{2(a^2+\sigma_1^2)}\right). \quad (34)$$

Thus, knowing $(T_{g_1} f)(a, 0)$ we can determine $N_1$, $\sigma_1$, $x_m$.

The transformation with the $g_1$ basic wavelet is practically useful when we are looking for a Gaussian distribution with a center located apart from a certain point $x_0$. In this case, since $g_1(x)$ is antisymmetric, the local Gaussian fluctuations located at $x_0$ give no contribution to $(T_{g_1} f)(a, x_0)$. The extremal condition with respect to the scale variable $a$

$$\frac{\partial(T_{g_1} f)(a, 0)}{\partial a} = 0,$$

can be easily derived from (34), where $x_0 = 0$ without loss of generality. This leads to the biquadratic equation

$$3a^4 - 2x^2a^2 - 3\sigma^2 = 0,$$

which has a real positive solution

$$a_{extr} = x\sqrt{\frac{1+\sqrt{1+9(\sigma/x)^4}}{3}}. \qquad (35)$$

*7.2.4. Practical Application.* Practically, the method was applied to test the energy spectrum of plastic scintillators produced in Dubna for the NEMO experiment [21]. The electron energy resolution was measured with radioactive source $^{207}$Bi emitting 569 keV and 1063 keV $\gamma$-quanta and the corresponding internal conversion ($K$) electrons with the energy 481 keV and 978 keV.

A typical data sample, produced by a standard source with the coincidence measure method, is shown in Fig.16. The spectrum (the total intensity) contains the contributions of $K$, $L$, $M$, $N$ electron lines, and an unknown background.

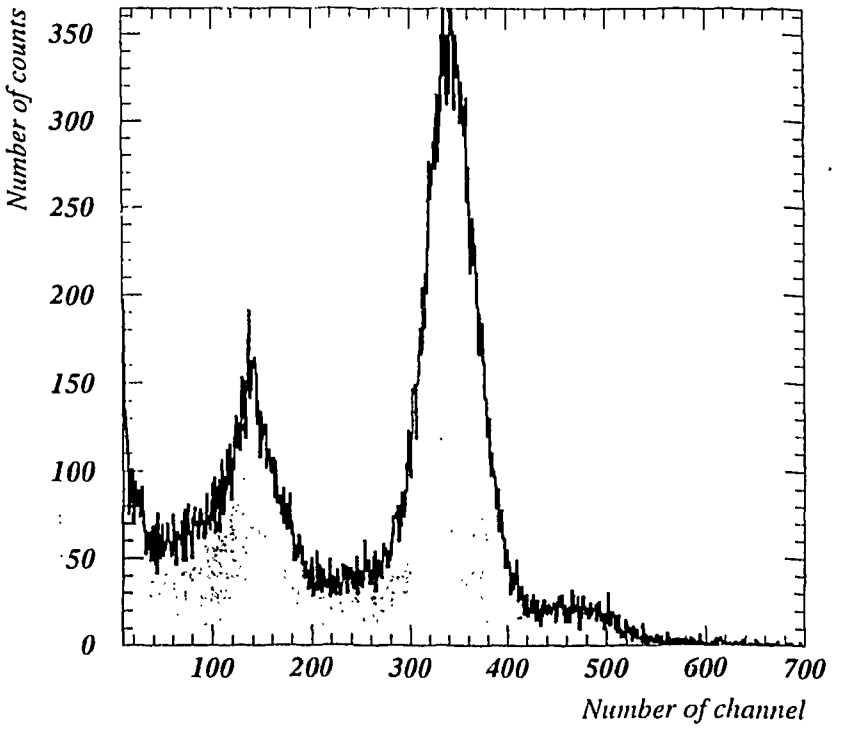


Fig.16. NEMO experiment. The electron energy spectrum registered in plastic scintillator test

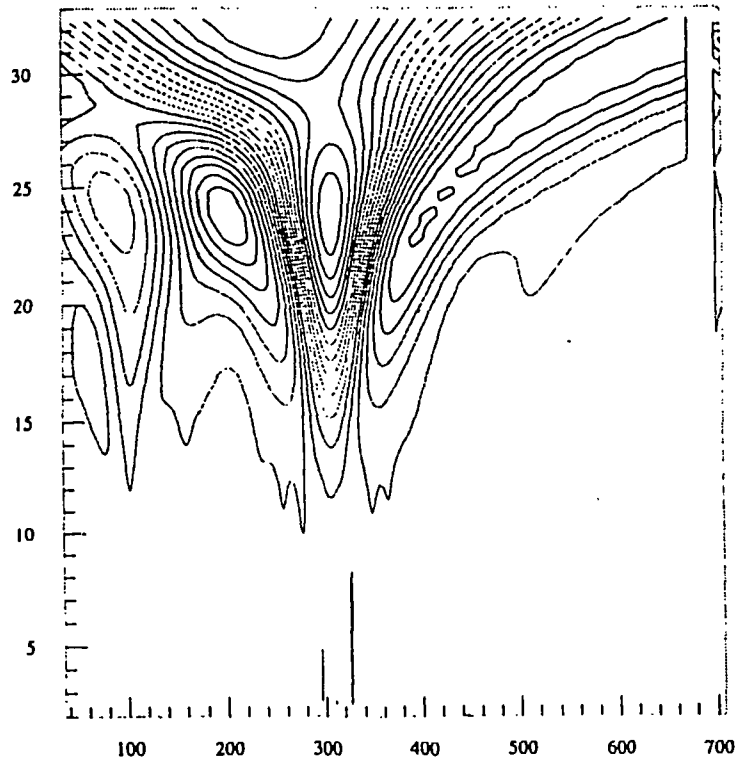


Fig.17. $q_2$ wavelet coefficient for the energy spectrum

Visualizing the wavelet image of the raw data we obtain a clear picture of the whole process with distinguished local maxima on the scale-versus-coordinate plane. For sufficiently distinguished peaks relation (31) provides a direct method of calculating without any numerical fit. For more complicated noisy data the method provides visualization of local maxima — possible sources of Gaussian distributions. The main advantage of wavelets, appearing even for the case of visually unseparable Gaussian peaks, is that we can see the same picture at different scales simultaneously and look for the sources according to the scale behaviour of wavelet coefficients. Besides, using two different wavelets, symmetric and antisymmetric, say $g_2$ and $g_1$, we can make a recurrent procedure based on formulae (32,34).

The plot of the wavelet image of these data is shown in Fig.17. The $X$-axis corresponds to the electron energy (in channels); the $Y$-axis corresponds to the $2^{1/4}$ based scale.

All the local maxima can be clearly seen on the plots. For the sufficiently separated peaks the energetic resolution ($\sigma$) of the peak can be directly determined from equation (31).

Since the statistics is not high enough, it requires both experimental knowledge and efficient data processing methods to get statistically valuable results from the existing data.

## 8. Conclusion

Wavelet analysis, which has been proved to be an efficient tool in all kinds of signal processing, seems to be even more promising in nuclear physics. There are several reasons for that:

- Being a robust integral transform, wavelet analysis does not require differentiability of the function in question and is stable under local perturbations. That is why it directly (without any preliminary smoothing) provides information about singularities and self-similarity, if they are present in experimental data.
- It is natural to define wavelet transform directly on probability space (and consider differentiable functions as a particular case) — thus we have a nonparametric statistical method [22].
- Wavelet analysis can be used in theoretical nuclear physics and provides a self-similar basis in Hilbert space of state vectors [23]. Thus we have a new bridge between observed statistical properties of quantum systems and their immanent quantum properties.

## Acknowledgement

The author is thankful to professor E.B.Zhidkov for stimulating discusion and to Mrs.Y.Padma, the secretary of B.M.Birla Science Centre (India), for typing some parts of this manuscript.

## References

1. Gabor D. — Journal of IEE, 1946, 93, p.429.
2. Morlet J. — In: Proc. 51st Annu. Meet. Soc. Explor. Geophys., Los-Angeles, 1981; Zimin V.D. — Izv. Atmos. Ocean. Phys., 1981, 17, p.941.
3. Grossman A., Paul T. — In: Lecture Notes in Physics, vol.211, Springer, Berlin, 1984; Grossman A., Morlet J., Paul T. — J. Math. Phys., 1985, 27, p.2473; Grossman A., Morlet J., Paul T. — Ann. Inst. H.Poincare, 1986, 45, p.293.
4. Carey A.L. — Bull. Austr. Math. Soc., 1976, 15, p.1; Duflo M., Moore C.C. — J. Func. Anal., 1976, 21, p.209.
5. Combes J.M., Grossmann A., Tchamitchan P. — Eds., Wavelets, Springer, Berlin, 1988.
6. Goupillaud P., Grossman A.; Morlet J. — Geoexploration, 1984/85, 23, p.85.
7. Muzy J.F., Bacry E., Arneodo A. — Phys. Rev. Lett., 1991, 67, p.3515; Muzy J.F. et al. — Phys. Rev., 1993, E47, p.875.
8. Holshneider M., Tchamitchan P. — In: Les Ondeletes, ed. by Lemarie P.G., Springer, Berlin, 1990.
9. Peng C.-K. et al. — Nature, 1992, 356, p.168; Voss R.F. — Phys. Rev. Lett., 1992, 25, p.3805.

10. Altaiski M., Mornev O., Polozov R. — B.M.Birla Science Centre Technical Report BSC-CAMCS-95-06-2, To appear in Genetic Analysis: Techniques and Applications.
11. Gale J.M. et al. — J. Mol. Biol., 1992, 224, p.343.
12. Afanasiev S.V., Altaisky M.V., Zhestkov Yu.G. — Nuovo Cim., 1995, A108, p.919.
13. Azimov Ya.I., Dokshitzer Yu.L., Khoze V.A., Troyan S.I. — Z. Phys., 1985, 27, p.65; ibid, 1986, C31, p.231.
14. Ochs W., Wosiek J. — Phys. Lett., 1993, B305, p.144.
15. Boca G., a.o. — Nuovo Cim., 1992, A105, p.865.
16. Gustafson G., Nilson A. — Z. Phys., 1991, C52, p.533.
17. Mikhopadhyay A., Jain P.L., Singh G. — Phys. Rev., 1993, C47, p.410.
18. Daubechies I. — Comm. Pure. Apl. Math., 1988, 16, p.909.
19. Beylkin G., Cifman R., Rokhlin V. — Comm. Pure. Apl. Math., 1991, 44, p.141.
20. Altaiski M., Kochetov O., Kovalenko V. — To appear in Engineering Simulation.
21. NEMO collaboration. — Nuclear Instruments and Methods in Physics Research, 1995, A354, p.338.
22. Frazier M.W. — In: Wavelets: Mathematics and Application, ed. by Benedetto J.J., CRC Press Inc, 1994.
23. Kaiser G. — Phys. Lett., 1992, A168, p.28.
Altaisky M.V. — Preprint ICTP, IC/94/281, Trieste, 1994.

Received on November 28, 1995.

*Краткие сообщения ОИЯИ №6[74]-95* *JINR Rapid Communications No.6[74]-95*

УДК 539.1.074.3;
51-72: 539.12

# DESIGN AND STUDY OF LIGHT READOUT SYSTEM FOR SCINTILLATOR SHOWER MAXIMUM DETECTOR FOR THE ENDCAP ELECTROMAGNETIC CALORIMETER FOR THE STAR EXPERIMENT AT RHIC

*G.Averichev, N.Moroz, Yu.Panebratsev, E.Potrebenikova, S.Razin, G.Škoro, V.Yurevich, I.Tsvetkov*

The possibility of using a strip/fiber-type shower maximum detector (SMD) in the endcap EMC for *pp*, *p*Au and AuAu collisions was investigated by simulation. It is shown that strip-type SMD is a good option for *pp* and *p*Au collisions, but is not suitable for AuAu. The compact module of 16 tiny Russian photomultipliers with one HV power supply channel is realized as a unit of a light readout system of the SMD.

The investigation has been perfomed at the Laboratory of High Energies, JINR.

## Разработка и исследование системы светосбора сцинтилляционного детектора максимума ливня торцевого электромагнитного калориметра установки STAR на ускорителе RHIC

*Г.Аверичев и др.*

Путем моделирования *pp*-, *p*Au- и AuAu-столкновений исследована возможность использования детектора максимума ливня стрипового типа в торцевом электромагнитном калориметре. Показано, что детектор максимума ливня стрипового типа может быть использован для pp- и *p*Au-столкновений, но не пригоден для AuAu-столкновений. Для светосбора с детектора максимума ливня разработан и создан компактный модуль, состоящий из 16 миниатюрных русских фотоумножителей с единым высоковольтным питанием.

Работа выполнена в Лаборатории высоких энергий ОИЯИ.

## 1. Introduction

The investigation performed by the IHEP group indicates that scintillator strip/fiber-type shower maximum detector (SMD) [1] is a good option for the barrel electromagnetic calorimeter for the STAR experiment [2]. There [1] has been tested only one photoreceiver — Russian photomultiplier FEU85. We have continued investigations in this direction with the goal to find a new compact module type sheme of light readout based on low-current tiny Russian photomultipliers. In this case only one HV channel of a standard power supply source should be enough to feed one light receivers module.

We would like also to reply on the question whether it is possible or not to use a scintillator strip type endcap SMD not only in investigations of polarized proton collisions at *RHIC* but in study of *p*Au and AuAu collisions as well. For this purpose we have carried out Monte Carlo simulation.

The proposed endcap EMC is a lead-scintillator sampling calorimeter. The inner and outer edges of the endcap EMC subtend polar angles of $\Theta = 15.4°$ and $\Theta = 38.3°$, respectively, and it will cover the rapidity range from 1.0 to about 2.0. The space available for the endcap EMC and its electronics ranges from $Z = 2712$ to $Z = 3087$ mm, with $Z$ along the beam direction, and covers radial range from $r = 774.8$ to $r = 2460$ mm, respectively.

It is proposed that the SMD will be placed into the endcap EMC at a depth of $5 + 7X_0$ into 2.5 mm gap. It will consist of $\Delta\varphi = 30°$ sections each of which includes two sets of scintillator strips, placed perpendicularly each to another and oriented at 45° angle to the center line of the section. The light readout from each strip will be done by means of wavelength-shifting (WLS) fiber, mounted in a groove of the strip and connected by clear fiber (about 3m) to a photoreceiver (PMT or avalanche photodiode).

## 2. Monte Carlo Simulation

The Monte Carlo program GEANT 3.15 with a 1 MeV cut for γ's and electrons was used to study EM showers, and HIJING model event generator has been used to describe proton-nucleus and nucleus-nucleus collisions.

Figure 1 shows rapidity distribution of γ's and hadrons in *pp*, *p*Au and AuAu collisions at an energy of 200 GeV/nucleon. The distributions of energies of direct gammas and gammas from $\pi^0$ decays in acceptance of endcap EMC are presented, too. It is seen, that main background in SMD is related with $\pi^0$ channel of γ production. The number of γ's in the SMD acceptance is about 800 in central AuAu collision and about 10 in central *p*Au collision.

The γ-initiated showers are symmetrical with respect to the line of flight of the primary γ. In Fig.2 are shown transverse profiles of 15 GeV γ shower in the first and the second plane of SMD, placed into endcap EMC at the depth of $5X_0$'s about the position where the maximum development of shower occurs. To identify the single shower the scintillator strips must have the width not larger than 12 mm. The IHEP group data confirm our results [2]. We use 1 cm width scintillator strip in our investigations.

In Fig.3a are shown the charged particles multiplicity distribution on the first SMD plate for the central *p*Au and AuAu collisions. Referring to Fig.3b, where is presented the energy deposited in SMD scintillator vs. distance from the center of SMD, one can see that about 75% of the showers are in the central area 75 cm $< R <$ 160 cm. This area contains about 600 γ's (AuAu collision case). In Fig.4 is shown the energy deposited in the central 5 cm wide ring of SMD vs. azimuthal angle for 6°, 3° and 1°/ per bin. The one 3° bin contains ~3 strips and covers an area of about 40 cm. This area contains only one shower. It is seen that using 3° azimuthal bin the showers could be separated. The 75 cm $< R <$ 160 cm

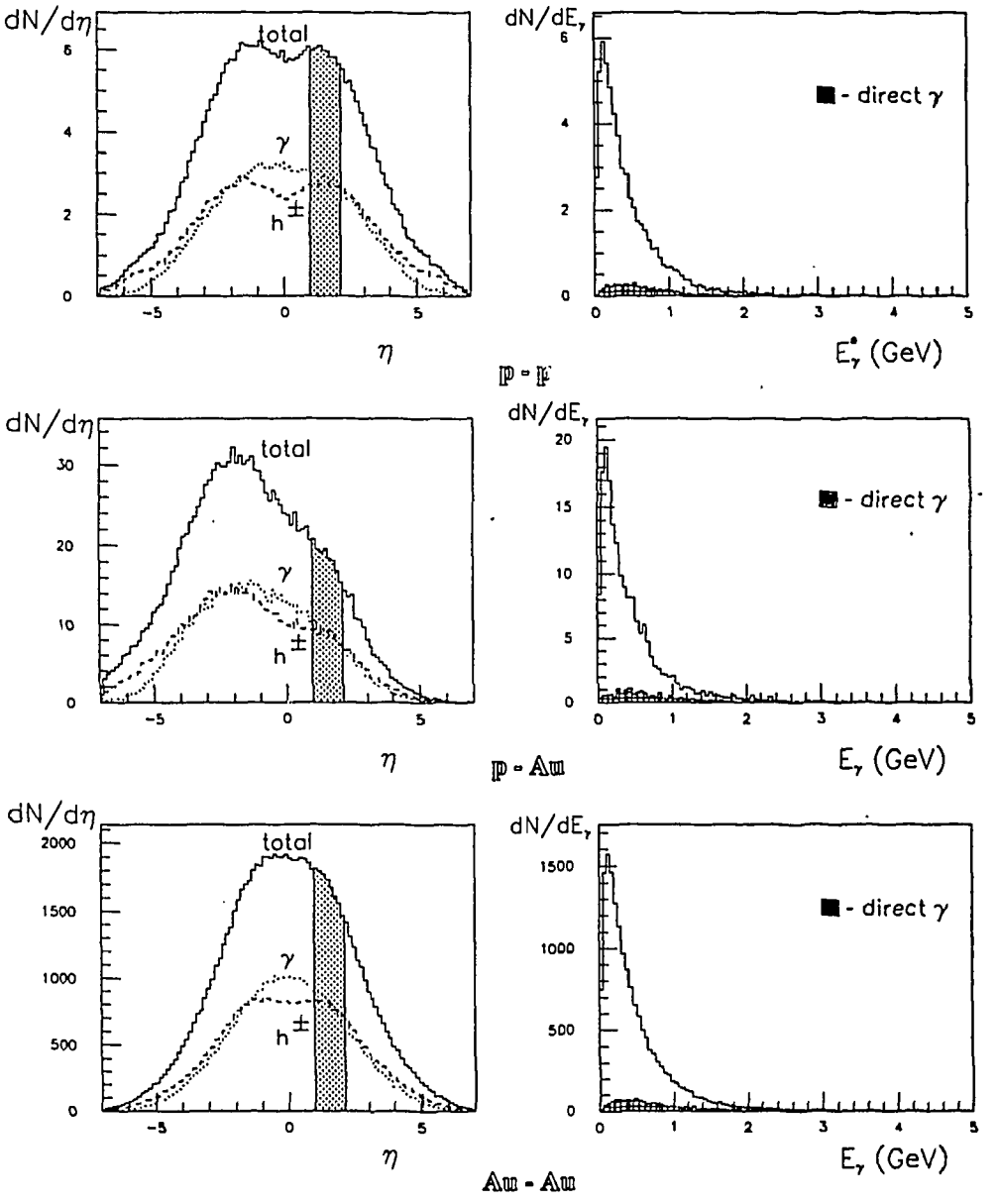


Fig.1. The pseudorapidity distribution of γ's and charged hadrons in *pp*, *p*Au and AuAu collisions at 200 GeV/nucleon

ring contains about 100 strips per 30° sector, so we have ~1.5 γ's per three strips. Then, we can conclude that the strip-type SMD is not suitable for separating the showers from AuAu collisions.

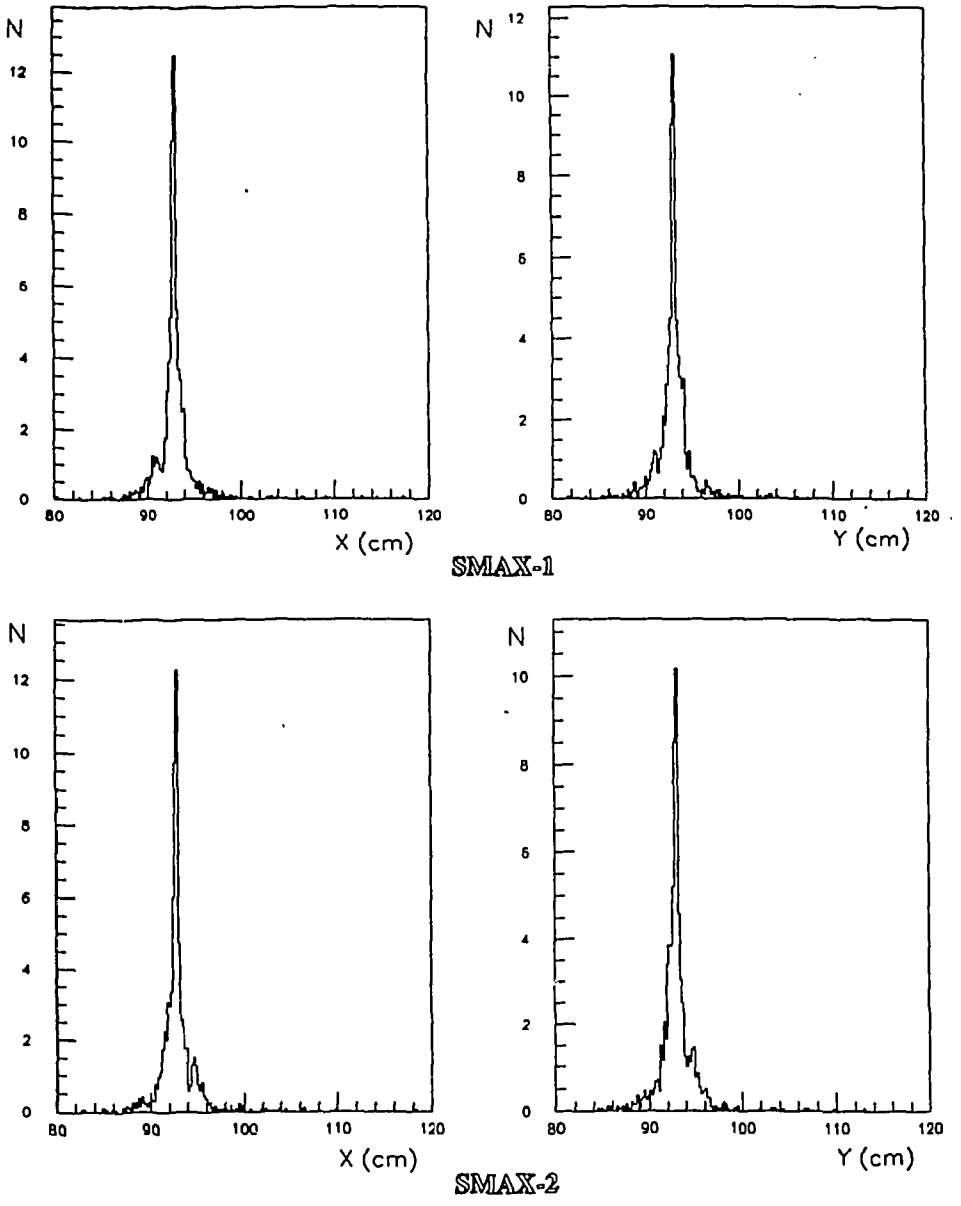


Fig.2. The transverse profiles of shower, induced by 15 GeV gamma

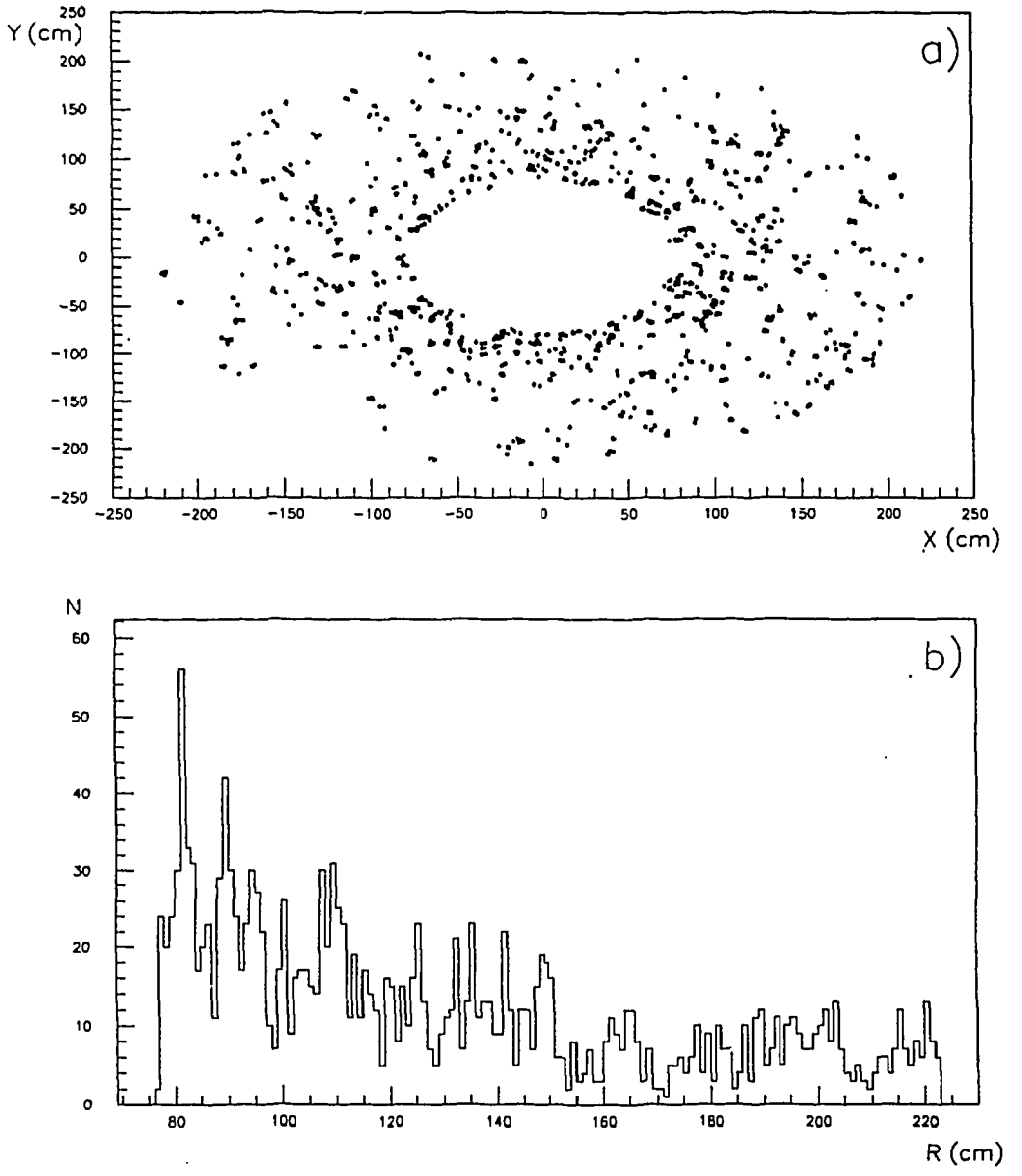


Fig.3. (a) Scatter plot of shower charged particles distribution on the first SMD layer; b) The number of shower charge particles vs. the distance from the SMD centre

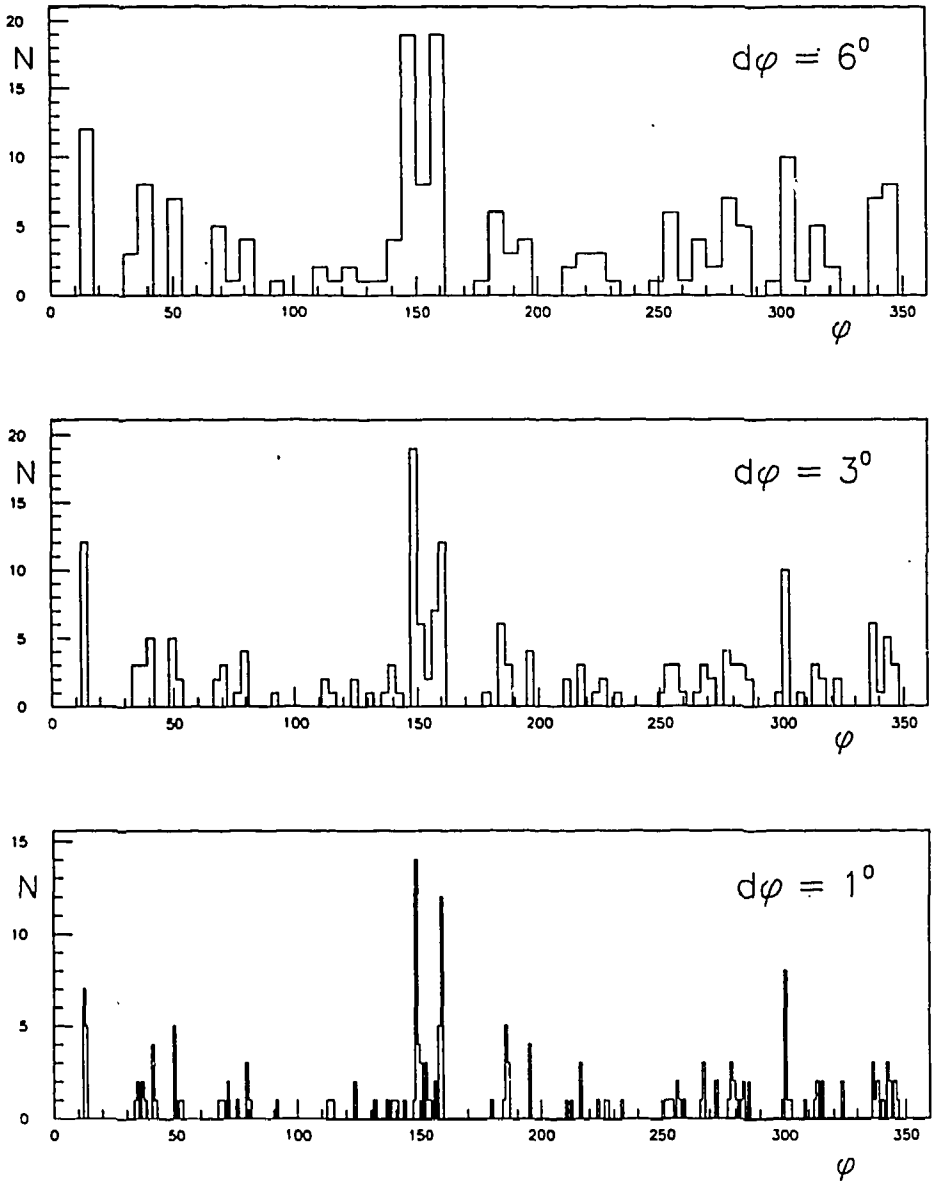


Fig.4. The energy deposited in the central 5 cm wide ring of SMD vs. azimuthal angle for 6°, 3° and 1° per bin for the central AuAu collisions

## 3. SMD Prototype Design

Following by results of our simulations and experimental study [2,3] the optimal thickness of scintillator strip is $4 \div 6$ mm and its width is $10 \div 12$ mm in order to obtain needed position resolution. We used a scintillator strip of 10 mm width and 4 mm thickness in our studies. In this case the full SMD will contain about 5300 strips. The SMD strips were read-out with wavelength-shifting fibers. The light collected by WLS fiber is transported via a long clear fiber to photodetector. The scintillator and the WLS fiber were wrapped with an aluminum foil. The hodoscope's scintillator plane of prototype contains 16 strips. Our investigations, the results of which are given in the next chapter, show that compact Russian photomultipliers like FEU-162, FEU-96 and FEU-60 with the gain more than $10^5$ and quantum efficiency of photocathode about 15% can be used in SMD as photodetector. The high resistance dividers of the PMTs with about 100 μA current are used. The tested photomultiplier's specifications are given in Table 1. It allows us to use only one 2mA high voltage power supply channel for 16 phototubes module of the SMD and significantly reduce the cost of production of the HV power system. The two stage amplifier with the total gain about $10^3$ is used for getting the suitable PMT pulse height. As an amplifier unit we used the Russian charge amplifier chip «Garantija» with the maximum gain about $10^2$. The electronics components of the first amplifier cascade is placed just at the PMT divider board to reduce a noise. The photomultipliers operate at the nominal anode voltage ~1000V (FEU-60, FEU-68, FEU-85) and ~1500 V ( FEU-96, FEU-162).

The prototype module of 16 photomultipliers has the size $12 \times 12 \times 30$ cm. The total number of modules (324 units) for the hole SMD will have the size $216 \times 216 \times 30$ cm. The prototype module is shown in Fig.5.

**Table 1**

| Parameters | FEU-85 | FEU-162 | FEU-96 | FEU-60 | FEU-68 |
|---|---|---|---|---|---|
| Diameter, mm | 30 | 22.5 | 22.5 | 15 | 15 |
| Length, mm | 107 | 75.0 | 75.0 | 70 | 70 |
| Photocatode type | Sb-Cs | Sb-Na-K-Cs | Sb-K-Sc | Sb-Cs | Sb-Na-K-Cs |
| Quantum efficiency ($\lambda = 480$ nm), % | 10 | 15 | 15 | 10 | 15 |
| Gain | $\sim 10^6$ | $\sim 10^5$ | $\sim 10^5$ | $\sim 10^5$ | $\sim 10^4$ |
| Current divider, μA | 100 | 100 | 100 | 100 | 100 |

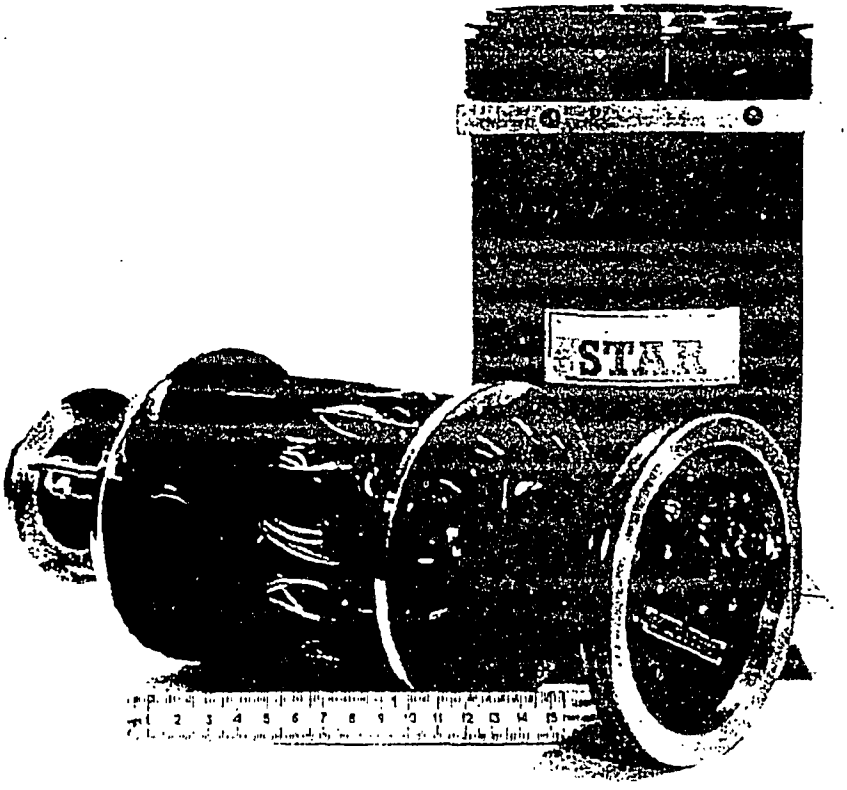


Fig.5. The phototype SMD module of 16 photomultiplier

## 4. The PMT Test Experimental Set-Up

A number of tests have been performed with Russian photomultiplier FEU-60, FEU-68, FEU-85 and FEU-162. Figure 6 shows a schematic view of the experimental set-up and logic of the measurements.

A WLS fiber BCF-91A with diameter of 1 mm, ($\lambda = 480$ mm) was used. A clean fiber BCF-91B had length ~1 m. The thickness and the width of the scintillation strip were 4 mm and 10 mm, respectively. Data were taken with Ce-144 source. The gate of ACD was ~60 ns and have been produced by coincidence of Monitoring Counter (FEU-87) and Coinciding Counter (FEU-87) signals. The threshold of Monitoring Counter was about 400 keV and defined the low level of scintillator light.

The Coinciding Counter threshold was as low as possible in order to detect all electrons passed through scintillator strip.

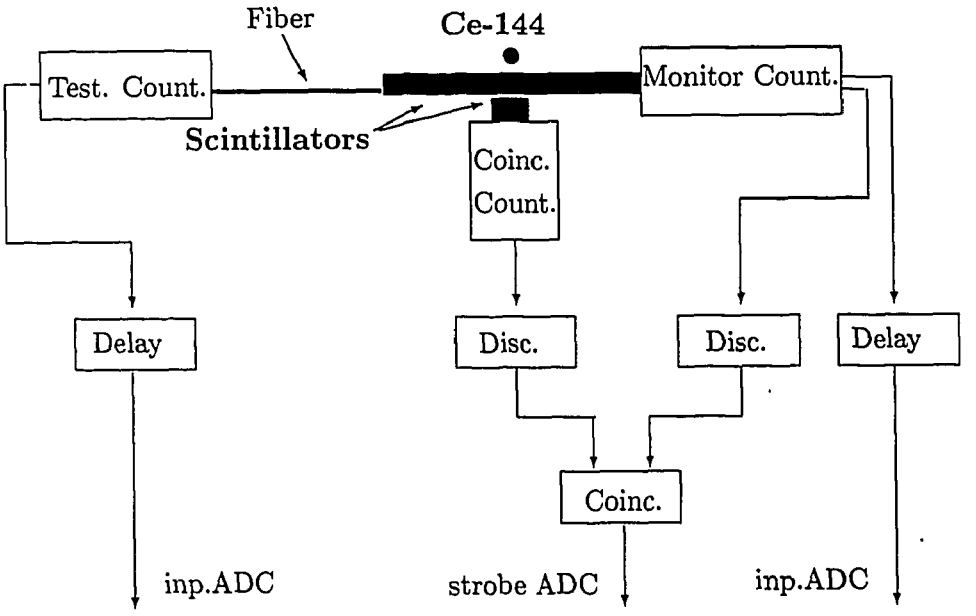


Fig.6. The experimental set-up and logic of the test measurements

The testing PMT were placed one by one in turn into Experimental Counter area so they have the equal optical conditions.

## 5. Results

At first, we have repeated the IHEP test of EU-85. Pulse heights measured with FEU-85 are shown in Fig.7. One can see that our results are in good agreement with IHEP data and we can conclude that our optical chain works right.

For PMT FEU-85, which has a gain of about $10^6$, we obtain ~2.5 photoelectrons per MIP. Figures 8a, 8b and 8c show the results of test for FEU-162, FEU-96 and FEU-60, respectively. They have a gain of ~$10^5$. The total gain of read-out electronics was 120 (FEU-162), 80 (FEU-96) and 80 (FEU-60). In the case of PMT FEU-85 it was ~20. The ADC pulse heights distribution for FEU-68 is shown in Fig.8d.

The results of our PMT tests are summarized in Table 2.

One can see that the photomultipliers with gain more than $10^5$ are suited for using as photoreceiver in SMD.

**Table 2**

| PMT | PMT gain | read-out gain | $N_{p.e.}$/MIP |
|---|---|---|---|
| FEU-85 | $\sim 10^6$ | 20 | y2.5 |
| FEU-162 | $\sim 10^5$ | 120 | ~1 |
| FEU-96 | $\sim 10^5$ | 80 | ~1 |
| FEU-60 | $\sim 10^5$ | 80 | ~1 |
| FEU-68 | $\sim 10^4$ | 450 | ~0.7 |

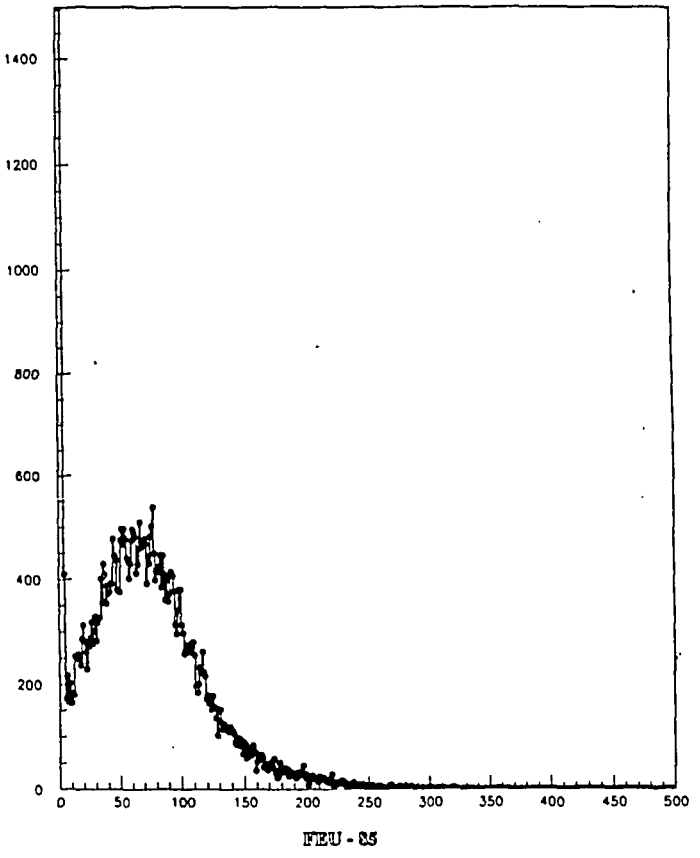


Fig.7. The ADC pulse heights distribution measured with FEU-85

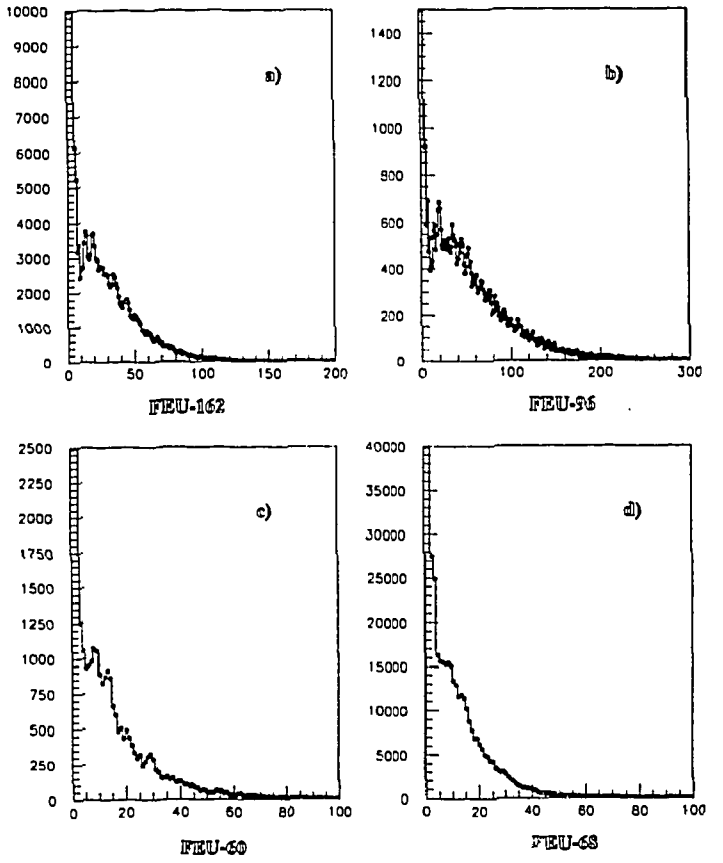


Fig.8. The same as in Fig.7 for the FEU-162, FEU-96, FEU-60 and FEU-68

## 6. Conclusions

The possibility of using a strip/fiber-type shower maximum detector (SMD) in the endcap EMC for the STAR experiment at RHIC for *pp*, *p*Au and AuAu collisions was investigate by simulation. It is shown that strip-type SMD is a good option for *pp* and *p*Au collisions, but is not suitable for AuAu. The compact $12 \times 12 \times 30$ cm module of 16 tiny Russian photomultipliers with one HV power supply channel is realized as a unit of light readout system of the SMD.

## 7. Acknowledgements

The authors are grateful for support by the Russian Fundamental Science Foundation under grant 95-02-05061 and the RHIC Department at BNL under contract 776746.

## References

1. Akimenko S.A. et al. — IHEP Preprint 94-94, Serpukhov, 1994.
2. Conceptual Design Report for the Solenoidal Tracker at RHIC, the STAR collaboration, PUB-5347 (1992).
3. Solenoidal Detector Collaboration, Technical design Report. SDC-92-201, SSCL-SR-1215, 1 April 1992.

Received on December 1, 1995.

*Краткие сообщения ОИЯИ №6[74]-95* *JINR Rapid Communications No.6[74]-95*

УДК 539.17.015

# A STUDY OF MULTIPARTICLE AZIMUTHAL CORRELATIONS IN HIGH ENERGY INTERACTIONS

*V.V.Belaga, G.M.Chernov*

Genuine multiparticle azimuthal correlations between secondary charged particles produced in hadron-nucleon and hadron-nucleus collisions at $p_0$ = 200–400 GeV/c and in nucleus-nucleus collisions at $p_0$ = (2.5–4.5)$A$ GeV/c have been studied using a new formalism. These correlations are observed for all types of charged secondaries and in all types of interactions. The meaning of obtained results and capabilities of suggested technique are also discussed at a semi-quantitative level.

The investigation has been performed at the Laboratory of High Energies, JINR.

## Изучение многочастичных азимутальных корреляций в соударениях с большой энергией

*В.В.Белага, Г.М.Чернов*

С помощью нового формализма изучались истинные многочастичные азимутальные корреляции между вторичными заряженными частицами в адрон-нуклонных и адрон-ядерных соударениях при $p_0$ = 200–400 ГэВ/с и в ядро-ядерных соударениях при $p_0$ = (2,5–4,5)$A$ ГэВ/с. Такие корреляции обнаружены для всех типов вторичных заряженных частиц и всех типов взаимодействий. На полуколичественном уровне обсуждены значимость полученных результатов и возможности предложенной техники анализа.

Работа выполнена в Лаборатории высоких энергий ОИЯИ.

## 1. Introduction

The necessity of studying the correlation and fluctuation properties of secondary particles created in multiple particle production reactions at high energies arises from the fact that their simplest characteristics, such as multiplicities or one-particle distributions, reveal a low sensitivity to the choice between various theoretical approaches to the theory of strong interactions. This topic has become very popular, mainly due to the advances that have recently been made in understanding the internal dynamics of multiparticle processes. This has come about with the analysis of various kinds of correlations and fluctuations [1] and also because of its obvious relation with the very important problem of the search for and study of the new hypothetical collective phenomena in particle and nuclear physics.

Correlations between «longitudinal» characteristics (such as rapidities, pseudorapidities, etc.) of secondary particles are considered most often in theoretical and experimental

works devoted to this problem. At the same time, the study of azimuthal correlations has a great advantage in that they do not depend on strong pseudocorrelation effects caused by nonuniformity of the events forming the inclusive or semi-inclusive sets under study [2].

Strictly speaking, at present, only the production of resonances, quantum effects associated with the identity of particle, and jets arising in hard QCD processes are well-established dynamic factors that lead to correlations among particles produced in multiple processes. At the same time, although a number of additional interesting physical phenomena have long been discussed in the literature, the questions concerning the existence and properties of these effects remain unanswered. Among them, for instance, «heavy» unstable intermediate objects (that cannot be reduced to known resonances), effects of a «collective flow» type and some other collective properties of quark-gluon, hadron or nuclear matter may be mentioned. One of the reasons behind this situation is that the number of works devoted to the search for genuine multiparticle correlations is obviously unsufficient.

In this report, we present the first results obtained by applying some general methods for analyzing genuine multiparticle azimuthal correlations between secondary particles from hadron-nucleon (*hN*), hadron-nucleus (*hA*) and nucleus-nucleus (*AA*) collisions at high energies. We will not be concerned with the usual two-particle azimuthal correlations based on the relative azimuthal angles

$$\varepsilon_{ij} = \arccos\left(\mathbf{p}_{T_i}\mathbf{p}_{T_j}/p_{T_i}p_{T_j}\right) = \arccos\left(\varphi_i - \varphi_j\right)$$

(here $\mathbf{p}_T$ and $\varphi$ are the transverse momentum and azimuthal angle of the particle, respectively) and their characteristics, nor with the so-called global variables of the events (such as sphericity, coplanarity, directivity, etc.) that give only indirect information on the character of azimuthal correlations between the particles. Tests of the above-mentioned methods show that they may turn out to be an efficient tool for studying final multiparticle states of multiple production reactions and nuclear multifragmentation at high energies.

## 2. Methodological Aspects

Recently, the following random variables characterizing the azimuthal correlations of arbitrary order were suggested:

(i) the minimum length of the azimuthal interval containing an arbitrary number $k(2 \le k \le n)$ of ordered azimuthal angles, i.e., the differences (or «spacings») [3,4]

$$\psi_{k-1}^{(n)} = \begin{cases} \varphi_{i+k-1} - \varphi_i, & 1 \le i \le n-k+1, \\ 2\pi + \varphi_{i+k-1-n} - \varphi_i, & n-k+1 < i \le n \end{cases} \tag{2}$$

of the order $(k-1)$;

(ii) the dispersion of the $\varphi$-distribution of the same subgroups of charged particles [5,4]

$$\sigma_k^{(n)^2} = \begin{cases} \sum_{l=i}^{i+k-1} (\varphi_l - \overline{\varphi}_k^{(n)})^2/(k-1), & 1 \le i \le n-k+1, \\ [\sum_{l=i}^{n} (\varphi_l - \overline{\varphi}_k^{(n)})^2 + & \\ + \sum_{l=1}^{i+k-1-n} (2\pi + \varphi_l - \overline{\varphi}_k^{(n)})^2]/(k-1), & n-k+1 < i \le n \end{cases} \tag{3}$$

where $\overline{\varphi}_k^{(n)} = \sum_{l=i}^{i+k-1} \varphi_l/k$, etc. The second terms in Eq.(2) and Eq.(3) are introduced for symmetrization over the full azimuthal circle;

(iii) the geometric average of the relative angles (Eq.(1)) for the subgroups containing $k$ nonordered particles [6,7]

$$\varepsilon_k^{(n)} = \left( \prod_{i<j}^{M} \varepsilon_{ij} \right)^{1/M}, \quad M = k(k-1)/2. \tag{4}$$

All the statistical characteristics of the mentioned variables can be found for independent emission of the particles (or in zero approximation, when all correlations are absent). For instance, for the first of them, $\psi_{k-1}^{(n)}$ [3]: the distribution density is

$$f(\psi_{k-1}^{(n)}) = (2\pi)^{1-n} \frac{(n-1)!}{(k-1)!\,(n-k-1)!} \psi^{k-1}(2\pi - \psi)^{n-k-1},$$

the moment generating function is

$$m(t) = \Phi(k, n, 2\pi t)$$

(where $\Phi$ is the hypergeometric function), and the moments of arbitrary order $r$ are

$$\nu_r = \left. \frac{d^r m(t)}{dt^r} \right|_{t=0} = (2\pi)^r \frac{(k+r-1)!\,(n-1)!}{(k-1)!\,(n+r-1)!}.$$

The simplest of the moments are: a) the expectation value

$$\langle \psi_{k-1}^{(n)} \rangle = \nu_1 = 2\pi(k-1)/n \tag{5}$$

and b) the standard deviation of the $\psi_{k-1}^{(n)}$-distribution

$$\sigma_0(\psi_{k-1}^{(n)}) \equiv (\nu_2 - \nu_1^2)^{1/2} = (2\pi/n) \left[ \frac{k(n-k)}{n+1} \right]^{1/2}. \tag{6}$$

Eq.(5) is trivial because we have $\sum (\psi_{k-1}^{(n)}) = 2(k-1)\,\pi$ in any case. $\sigma(\psi_{k-1}^{(n)})$ can be used, however, as a measure of multiparticle azimuthal correlations since any deviation from the value given by Eq.(6) means that the statistical independence of the angles $\varphi$ has been violated, i.e., there are correlations between them. The zero approximation expectation value and standard deviation of the second variable, $\sigma_k^{(n)^2}$, are equal to

$$\langle \sigma_k^{(n)^2} \rangle = \pi^2(k+1)(k+2)/[3n(n+1)] \tag{7}$$

and

$$\sigma_0(\sigma_k^{(n)^2}) = (\pi^2/3)\left[\frac{(k+1)(k+2)}{k(k-1)\,n(n+1)} \times \right.$$

$$\left. \times \left( \frac{(k+3)(k+4)(5k^2-k+6)}{5(n+2)(n+3)} - \frac{(k-1)k(k+1)(k+2)}{n(n+1)} \right) \right]^{1/2}, \tag{8}$$

respectively [5], etc.

The formulas presented above are written for fixed $n$. They can be easily generalized for inclusive sets of events by using normalized quantities. For example, instead of $\psi_{k-1}^{(n)}$, we considered

$$\Phi_{k-1}^{(n)} = (\psi_{k-1}^{(n)} - \langle \psi_{k-1}^{(n)} \rangle)/\sigma(\psi_{k-1}^{(n)}). \tag{9}$$

The expectation value and standard deviation of $\Phi_{k-1}^{(n)}$ are exactly equal to 0 and 1, respectively, in the case of the independent emission of the particles under study. Therefore, any deviations from these values mean the existence of some kind of correlation.

## 3. Experimental Data and Results

As a first approbation of the above methodology, we carried out a search for multiparticle azimuthal correlations in six inlcusive sets of hadron-nucleon ($hN$) and hadron-nucleus ($hA$) collisions at primary momenta of 200 and 400 GeV/c and in four sets of nucleus-nucleus interactions at primary momenta of 2.5—4.5 GeV/c per nucleon. All the experiments were carried out under identical conditions with the help of the emulsion technique. The data on the statistics of the events in these sets are presented in the Table below, which also gives references to the papers containing detailed information on the

**Table**

| Projectile | Target | $p_0/A$, GeV/c | Accelerator | Numb. of events | Refs. |
|---|---|---|---|---|---|
| $p$ | $N$ | 200 | Fermilab. | 1293 | [8] |
| $p$ | $Em$ | 200 | Fermilab. | 1626 | [8] |
| $\pi^-$ | $N$ | 200 | Fermilab. | 1397 | [9] |
| $\pi^-$ | $Em$ | 200 | Fermilab. | 5116 | [9] |
| $p$ | $N$ | 400 | Fermilab. | 1061 | [10] |
| $p$ | $Em$ | 400 | Fermilab. | 3484 | [11] |
| $^{12}C$ | $Em$ | 4.4 | JINR | 1717 | [12] |
| $^{14}N$ | $Em$ | 2.9 | LBNL | 1027 | [13] |
| $^{22}Ne$ | $Em$ | 4.1 | JINR | 4070 | [14] |
| $^{56}Fe$ | $Em$ | 2.5 | LBNL | 1890 | [15] |

experimental conditions and various general characteristics of the events (multiplicities, single-particle distributions, etc.).

A search for multiparticle correlations was carried out for relativistic charged ($s$) particles from $hN$ and $hA$ collisions and for all types of charged secondaries — shower ($s$), «gray» ($g$) and «black» ($b$) particles from nucleus-nucleus interactions. Division of the charged particles into mentioned types was made according to usual emulsion criteria.

*3.1. hN and hA Collisions at* $p_0$ = 200–400 *GeV/c*. Figure 1 shows, as an example, the values of the standard deviation $\sigma(\psi^{(n)}_{k-1})$ of the distribution in the normalized minimum length of the interval containing $k$ neighbouring (with respect to the azimuth) secondary relativistic charged particles produced in $hN$ and $hA$ collisions at 200 and 400 GeV/c. Here and below we only use the first of above methods, because the application of others gives the same results.

The next necessary step in the correlation analysis is to quantitatively take into account trivial kinematic correlations that are due to the effects of conservation laws. For this purpose we generated inclusive ensembles of random events following the phasespace ($PS$) model, taking into account the presence of neutral secondary particles. Their number, $n_0$, was simulated for each $n$ = 2, 4,... in accordance with the available experimental data on neutral particle production (including strange ones) in $pp$ collisions at $E_0$ = 200–400 GeV.

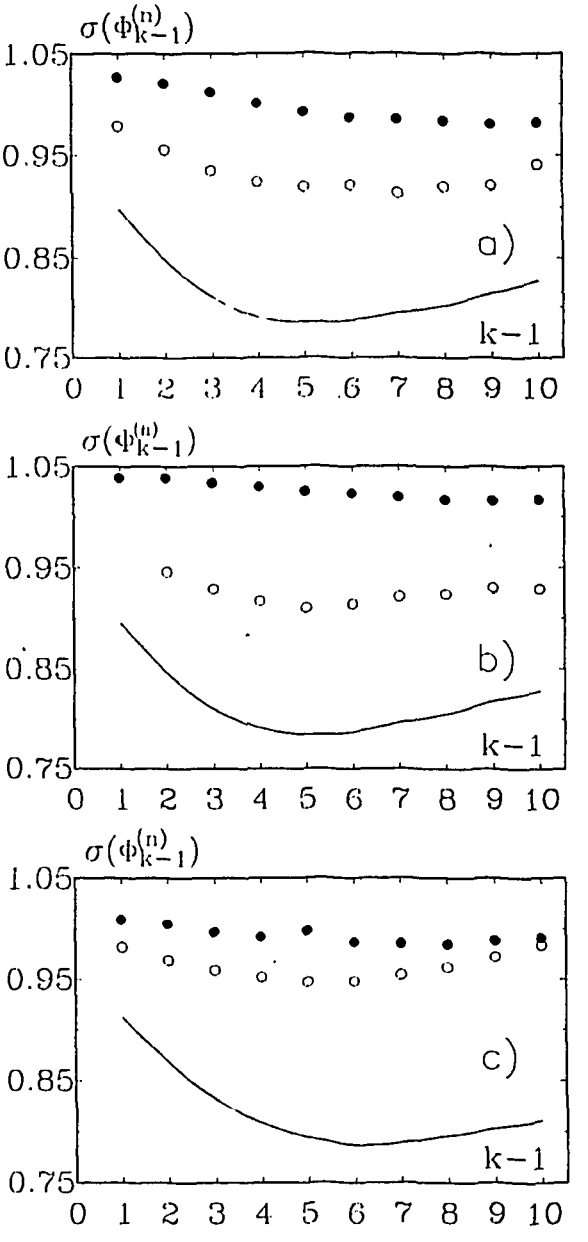


Fig.1. The $\sigma(\Phi^{(n)}_{k-1})$ *vs.* $k$ for $hN$ (open circles) and $hA$ (full circles) collisions: a) $pN$ and $pA$ at 200 GeV/c, b) $\pi^-N$ and $\pi^-A$ at 200 GeV/c, c) $pN$ and $pA$ at 400 GeV/c. The curves are calculated for $hN$ collisions according to the phasespace model

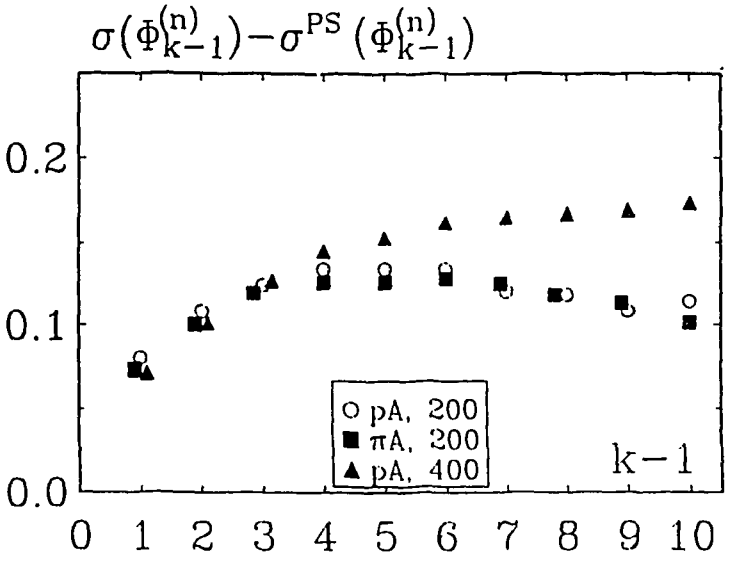


Fig.2. The differences of $\sigma(\Phi^{(n)}_{k-1}) - \sigma^{PS}(\Phi^{(n)}_{k-1})$ *vs.* $k$ for $hN$ collisions at 200—400 GeV/c

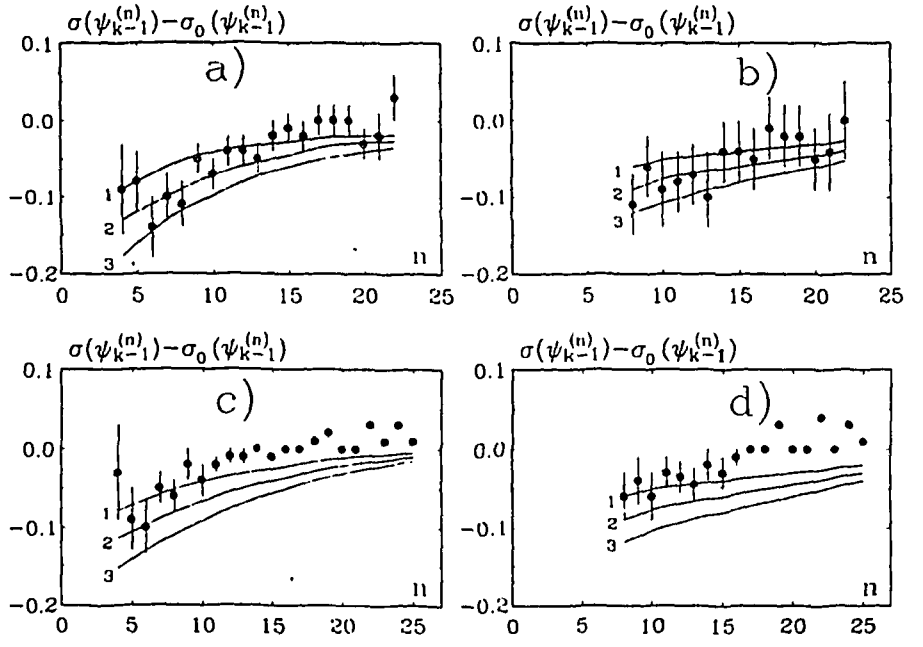


Fig.3. The differences of $\sigma(\psi^{(n)}_{k-1}) - \sigma_0(\psi^{(n)}_{k-1})$ *vs.* $n$ in comparison with the results (curves) of calculations according to the model with two-particle resonances for the fraction (1) 50, (2) 75, and (3) 100% of secondaries produced in their decays. The examples are given: for $hN$ collisions at $k = 4$ (a) and 6 (b); and for $hA$ collisions at $k = 4$ (c) and 6 (d)

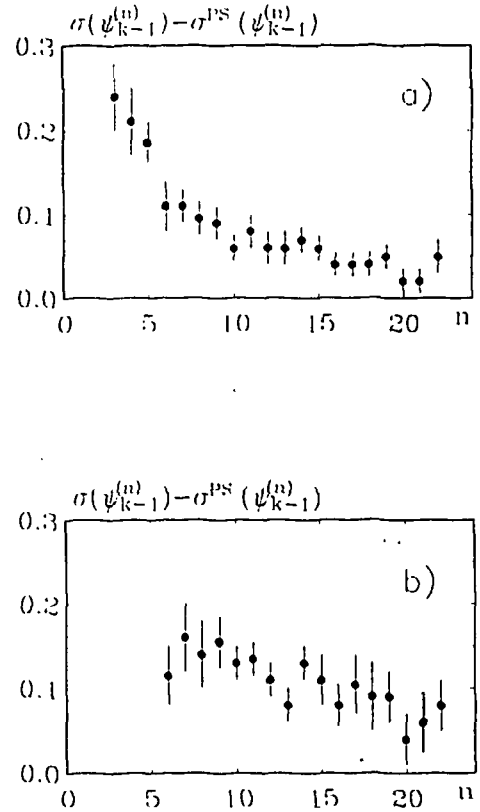


Fig.4. The differences of $(\psi^{(n)}_{k-1}) - \sigma^{PS}(\psi^{(n)}_{k-1})$ *vs.* $n$ at $k = 3$ (a) and $k = 5$ (b) for $pN$ collisions at 200—400 GeV/c

The charged particle multiplicity spectra for the real and simulated ensembles were exactly the same. The values of $\sigma(\Phi^{(n)}_{k-1})$ calculated in the *PS* model for *hN* collisions are shown by solid curves in Fig.1. Figure 2 presents the differences between $\sigma(\Phi^{(n)}_{k-1})$ in real and Monte Carlo ensembles of *hN* collisions *vs.* $k$ of the correlations. The following conclusions can be drawn from the inclusive data displayed in Figs.1, 2:

(i) There are genuine multiparticle azimuthal correlations of non-kinematic origin in *hN* collisions at 200—400 GeV/c;

(ii) These correlations are different for *hN* and *hA* interactions;

(iii) They do not depend on the type of primary hadron but depend on the primary momentum;

(iv) The «strength» of the correlations increases at first with increasing $k$ and then reaches a maximum value at a value of $k$ which depends on primary momentum.

Let us consider the semi-inclusive data. For simplicity, we combined events with fixed $n$ from all the ensembles of *hN* collisions ($pN$, 200 GeV/c + $\pi^-N$, 200 GeV/c + $pN$, 400 GeV/c) as well as from the ensembles of *hA* collisions. All the results of our analysis turned out to be a *posteriori* independent of this unification. Examples of these data are presented in Fig.3; it should be noted that we used non-normalized quantities of $\psi^{(n)}_{k-1}$ in the semi-inclusive case.

Finally, Fig.4 shows the differences $\sigma(\psi^{(n)}_{k-1}) - \sigma^{PS}(\psi^{(n)}_{k-1})$ for *hN* collisions at $k = 3$ and 5. One can see that the correlations in actual events differ from those caused by kinematic law for all values of $n$ up to the maximum values. We note that, at large $n$, the existence of the dynamical correlations is manifested only for high-order correlations and, apparently, was never observed before. It is important to note, also, that the correlations for the same $n$ are different for *hN* and *hA* collisions. This makes it possible to conclude that purely collective models of particle production in *hA* collisions are inadequate in the energy range under consideration.

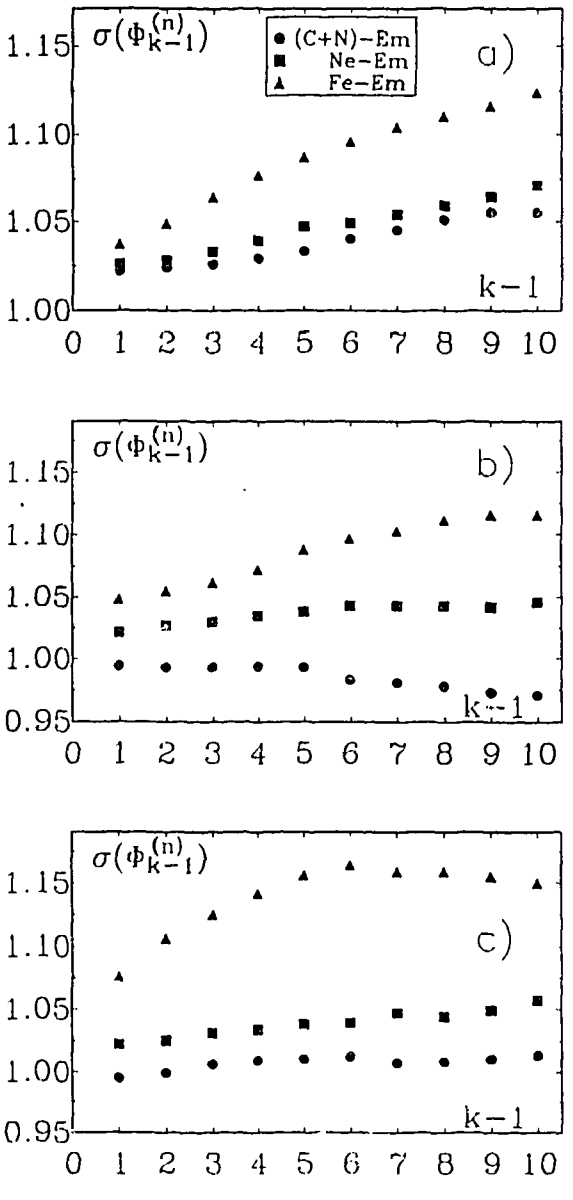


Fig.5. The $\sigma(\Phi^{(n)}_{k-1})$ *vs.* $k$ for *s*-particles (a), *g*-particles (b) and *b*-particles (c) from nucleus-nucleus collisions. The spectator fragments of projectile nuclei are excluded from relativistic secondaries

The production of a large number of resonances (ρ, Δ, *f*, etc.) is a well-established fact and it is one of the widely discussed physical mechanisms that can generate correlations between secondaries. According to various estimates, the number of particles produced in the decays of these resonances can be as large as 50—90% of their total number.

We considered the behaviour of the suggested characteristics of multiparticle correlations in the production of particles via the decays of two-particle resonances. It was shown that, for all $k$, these characteristics are sensitive to this phenomenon; so, the study of multiparticle correlations is a direct way to obtain answers to the questions concerning the existence of «heavy» intermediate objects that cannot be reduced to known resonances. It should be emphasized that preference should be given to the study of high-order correlations. An example of such analysis of the experimental data is shown in Fig.3.

We can state that the model with resonances can qualitatively describe the data for $n_s \leq 15$ if the fraction of the resonances is taken to be 50—75% for *hN* collisions and ≤ 50% for *hA* collisions. This model cannot, however, describe the data for larger $n_s$ and the inclusive data of Fig.2, especially the difference between the 200 and 400 GeV data.

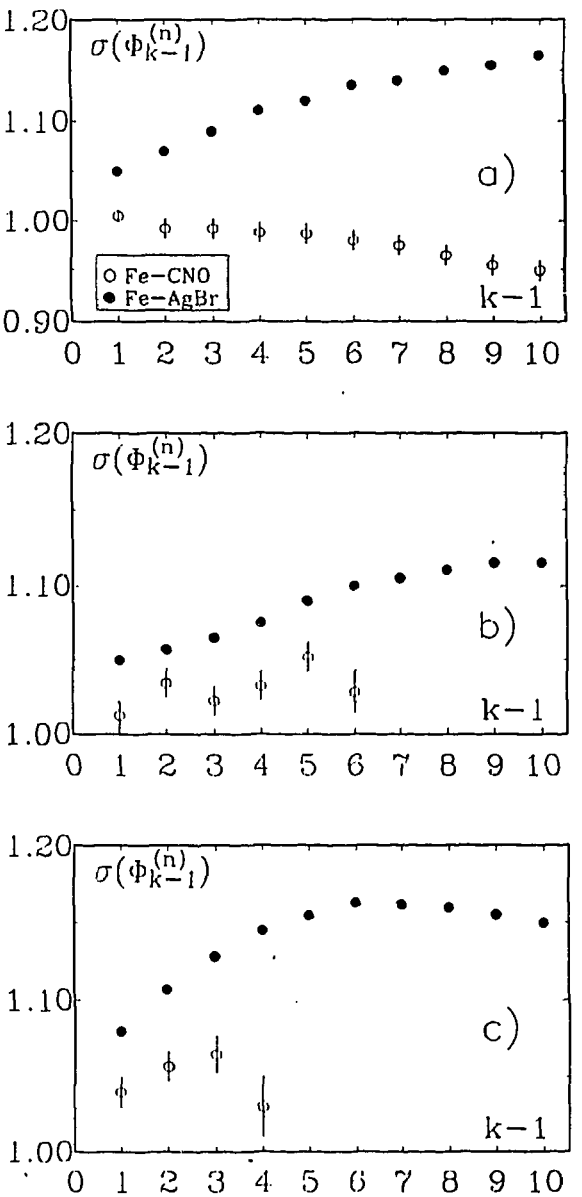


Fig.6. The same as in Fig.5 for Fe—CNO (open circles) and Fe—AgBr (full circles) collisions at 2.5 GeV/c per nucleon

Of course, we should not attach much importance to our conclusions at this point, because we only want to illustrate the capabilities of this new technique, based on the analysis of multiparticle correlations, and to present some qualitative estimates. We hope that we succeeded in doing this to a certain extent.

*3.2. Nucleus-Nucleus Collisions at* $p_0 = (2.5–4.5)A$ *GeV/c.* Finally, we would like to present briefly a preliminary analysis of the data on multiparticle azimuthal correlations in the nucleus-nucleus interactions at the energies realized at the Dubna and Bevalac accelerators (see the Table above). Typical examples of the dependences of $\sigma(\Phi_{k-1}^{(n)})$ on $k$ for all types of charged secondaries are presented in Fig.5. The data for $^{12}C$ and $^{14}N$ projectiles were combined; this unification is justified both a *priori* and a *posteriori*.

The following conclusions can be drawn:

(i) There are genuine multiparticle azimuthal correlations among all the types of charged secondaries from nucleus-nucleus collisions (except, may be, for target fragments from the collisions of light projectiles);

(ii) The «strength» of the correlations increases with increasing $k$, although this effect depends on the type of secondary particles and on some characteristics of nucleus-nucleus collisions;

(iii) The observed correlations depend on the atomic numbers of the projectile (see Fig.5) and target nuclei (see Fig.6): the larger the $A_{proj}$ (or $A_{target}$), the stronger the correlations;

(iv) They also depend on the impact parameter of the nucleus-nucleus collisions (not illustrated): the larger the «centrality», the stronger the correlations;

(v) There is evidence of prompt connections between the observed multiparticle azimuthal correlations and the widely discussed effects of collective flow («bounce off», «splash-side», «squeeze-out», etc.) in nucleus-nucleus collisions. Therefore, the suggested and discussed methodology is of great interest in the search for and study of such phenomena;

(vi) The semi-inclusive analysis showed, in addition, that the data are in agreement with the picture of independent emission of $s$-particles at $n_s \geq 6$—8. Besides, for any fixed $n_s$

$$\text{correlations } (AA) < \text{correlations } (hA) < \text{correlations } (hN).$$

Therefore, all the purely collective mechanisms of particle production (the simplest versions of hydrodynamical theory, the so-called «collective tube» model, etc.) in nuclear collisions are inconsistent with the experimental data at the energies under study.

In conclusion, the most general result of this work can be stated as follows: the study of multiparticle azimuthal correlations is a very powerful tool for investigations in high-energy and nuclear physics.

It will be reasonable to make a remark: in the case of very high multiplicities, it is useful to apply the above-mentioned methods to particles from different bins of rapidity. In this way very interesting possibilities are opened, but that is a topic for another paper.

References

1. De Wolf E., Dremin I.M., Kittel W. — Usp. Fiz. Nauk., 1993, 163, p.3.
2. Azimov S.A., Chernov G.M. — Statistical Methods in High Energy Physics, Tashkent, FAN, 1970.
3. Belaga V.V., Chernov G.M. — Dokl. AN Uzbekistana, 1991, No.6, p.20.
4. Belaga V.V., Chernov G.M. — Phys. At. Nucl., 1994, 57, p.1443.
5. Belaga V.V., Chernov G.M. — Dokl. AN Uzbekistana, 1992, No.1, p.16.
6. Jiang J. et al. — Phys. Rev. Lett., 1992, 68, p.2739.
7. Lauret J. et al. — Phys. Lett., 1994, B339, p.22.
8. Anzon Z.V. et al. — Yad. Fiz., 1975, 22, p.736.
9. Anzon Z.V. et al. — Nucl. Phys., 1977, B129, p.205.
10. Boos E.G. et al. — Yad. Fiz., 1979, 30, p.407.
11. Boos E.G. et al. — Nucl. Phys., 1978, B143, p.232.
12. Bondarenko R.A. et al. — Yad. Fiz., 1983, 38, p.1483.
13. Chernov G.M. et al. — Nucl. Phys., 1977, A280, p.478.
14. Andreeva N.P. et al. — Yad. Fiz., 1987, 45, p.123.
15. Chernov G.M. et al. — Nucl. Phys., 1984, A412, p.534.

Received on November 23, 1995.

УДК 539.172.177

# COHERENT MULTIFRAGMENTATION OF RELATIVISTIC NUCLEI

*G.M.Chernov*

Reactions of coherent multifragmentation have been predicted and observed for relativistic projectile nuclei. At the first stage of studying such reactions, we considered the coherent break-up of $^{12}C \to 3\alpha$ and $^{16}O \to 4\alpha$ at 4.5*A* GeV/c. Their study points to the most favourable conditions for the investigation of nuclear structure and the search for various quasi-nuclear resonances.

The investigation has been performed at the Laboratory of High Energies, JINR.

## Когерентная мультифрагментация релятивистских ядер

*Г.М.Чернов*

Были предсказаны и наблюдались реакции когерентной мультифрагментации релятивистских ядер-снарядов. На первой стадии изучения реакций этого типа рассматривалась когерентная диссоциация $^{12}C \to 3\alpha$ и $^{16}O \to 4\alpha$ при 4,5*A* ГэВ/с.Изучение подобных реакций указывает на наиболее благоприятные условия для исследования ядерной структуры и поиска квазиядерных резонансов.

Работа выполнена в Лаборатории высоких энергий ОИЯИ.

## 1. Introduction

As early as 1953, a new type of high-energy hadron-nucleus interaction — the reactions of the coherent generation of particles in strong or Coulomb fields of nuclei — has been predicted by Pomeranchuk and Feinberg [1]. Coherently influencing the bombarding object, the target nucleus is proved to be a single, structureless whole in these reactions and remains, as a rule, in the ground state. The coherence condition, $1/q \geq R$ ($R$ is the radius of target nucleus, $q$ is the transferred momentum), leads to very small values of momentum transfer and to high values of the energy thresholds of such reactions. The first of them, $\pi^- + A \to \pi^-\pi^-\pi^+ + A$, was experimentally observed in 1961, and since that time, this class of inelastic interactions with nuclei has become an object of intensive study in many laboratories.

Recently [2], this idea has been spread to the multifragmentation reactions of relativistic projectile nuclei. The events of coherent multifragmentation (Fig.1)

$$A + B \to B + \sum_i F_i, \tag{1}$$

as well as their analogues in the case of hadron-nucleus collisions, are characterized by very small energy-momentum transfers, which are the consequences of the coherence conditions, and by the high values of the energy thresholds. The considerable interest in such reactions is for a number of objective reasons, among which are the relative simplicity of their theoretical description, the presence of very favourable conditions for the search for and study of various quasi-nuclear resonances, the possibility of studying the interactions between these resonances and intranuclear matter, etc.

## 2. Some Kinematics

Figure 1 presents the simplest diagrams for the diffractive and the Coulomb mechanisms of the projectile nucleus coherent decay. Assuming, for instance, the diffractive mechanism of dissociation, we can formulate its global features as follows:

(i) The angular distribution of the summary momentum $\sum_i \mathbf{p}_i$ of fragments $F_i$ is the same as for elastic diffractive scattering;

(ii) The so-called intrinsic quantum numbers of the fragment system are the same as for the projectile nucleus;

(iii) The momentum transfer (to the target nucleus) is very small:

$$1/q \geq R_B. \tag{2}$$

From the energy-momentum conservation law one can easily find

$$q_L = \frac{M^{*2} - M_A^2}{2p_A} + \frac{E_A + M_B}{2M_B p_A} q^2 \approx \frac{M^{*2} - M_A^2}{2p_A} \tag{3}$$

(the approximation is correct at very high energies). So, the longitudinal ($q_L$) and transverse ($q_T$) momentum transfers are approximately independent and $q_L$ depends only on $M^*$.

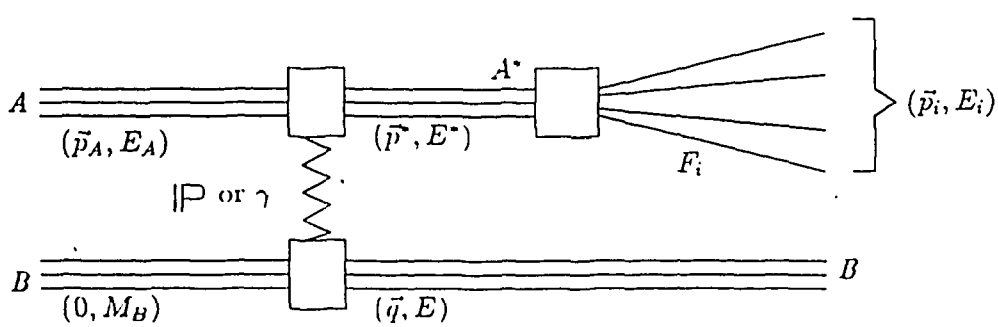


Fig. 1. The simplest diagrams for nuclear coherent dissociation

The four-momentum transfer is

$$d\sigma/dt' \sim \exp(-a|t'|), \qquad |t'| = |t - t^{\min}(\sum_i m_i)| \equiv q_T^2, \tag{4}$$

where $a = (R_A + R_B)^2/4$. Therefore, the distribution on $q_T$ has a Rayleigh form

$$d\sigma/dq_T^2 \sim \exp(-aq_T^2), \qquad \langle q_T \rangle \equiv (\pi/4a)^{1/2}. \tag{5}$$

The minimum value of $q_L$ is realized at $M^*_{\min} = \sum_i m_i$ and $q_T = 0$, i.e.,

$$q_L^{\min} \equiv \frac{(\sum_i m_i)^2 - M_A^2}{2p_A} \equiv \frac{M_A}{p_A}\Delta, \tag{6}$$

where $\Delta$ is the «mass detect» of the channel under consideration,

$$\Delta = \sum_{i=1}^{n} m_i - M_A \tag{7}$$

($m_i$ is the mass of $i$-th fragment). It is clear that $|t|^{\min} = (q_L^{\min})^2$ and

$$(M^{*2})^{\max} \equiv M_A^2 + 2p_A\,\mu B^{-1/3}. \tag{8}$$

Rough estimates of upper limits for $q_L$ and $q_T$ are given [1] by

$$q_L \le \mu/B^{1/3}, \qquad q_T \le \mu, \tag{9}$$

where $\mu$ is the pion mass and $B$ is the target mass number. Finally, Eqs.(3) nad (9) immediately give an estimation of the coherent reaction threshold

$$p_A^{\min} \equiv \frac{M^{*2} - M_A^2}{2\mu} B^{1/3} \equiv \frac{M_0 B^{1/3}}{\mu}\Delta. \tag{10}$$

For instance, for the reaction $^{16}O \to 4\alpha$ (see below) on a target with mass number $B \approx 100$, the threshold takes up about ~ 0.5 GeV/c per nucleon.

## 3. Some Experimental Results

The variety of exclusive channels for coherent reactions at high energies is very great. For example, the coherent emission of protons: $^AX_Z \to {}^{A-m}Y_{Z-m} + mp$ ($m = 1, 2, \ldots$), neutrons: $^AX_Z \to {}^{A-m}Y_Z + mn$, $\alpha$-particles: $^AX_Z \to {}^{A-4m}Y_{Z-2m} + m\alpha$, etc., by the projectile nucleus can be considered.

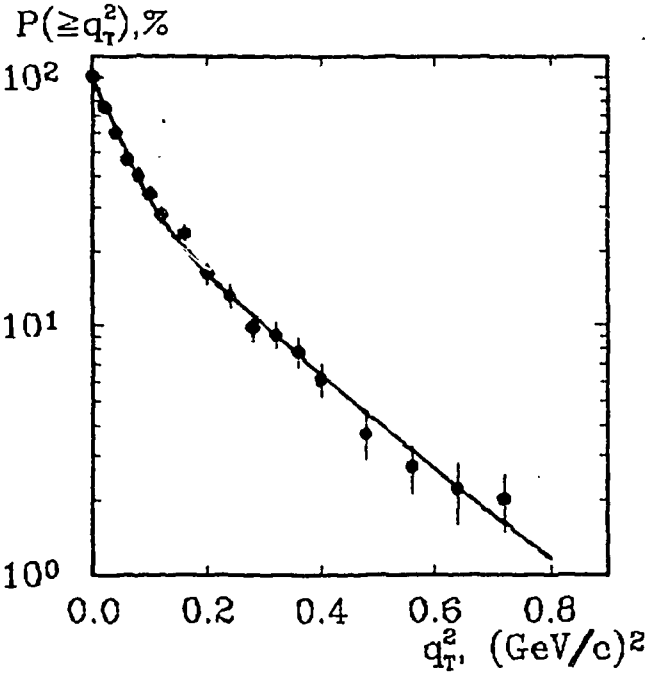


Fig.2. Integral distribution on $q_T^2$ for reaction (12) at 4.5*A* GeV/c. The curve is a fit by the sum of two Rayleigh distributions

The first experimental data, which confirmed the existence of coherent nuclear fragmentation reactions, have been obtained for channels

$$^{12}C \rightarrow 3\alpha, \tag{11}$$

using the usual nuclear photoemulsions, emulsions enriched by Pb and the 2m propane bubble chamber of LHE (JINR), and

$$^{16}O \rightarrow 4\alpha, \tag{12}$$

using the usual nuclear emulsion at $p_0 = (4.2 - 4.5)A$ GeV/c. For details for these experiments see Refs.[3,4, 5,6,7]; here we present only a short review.

The distributions of the four-momentum transfer (4) for the investigated channels (11), (12) have a typical form, reducing to the sum of two exponents corresponding to dissociation on a nucleon and on a nucleus as a whole. An example of such distribution is given in Fig.2.

Comparison of the data on various target nuclei also permits one to conclude that the diffraction mechanism probably dominates for the light nuclei; and the Coulomb one, for heavy targets. The mean free path for the coherent $^{12}C \rightarrow 3\alpha$ events in the emulsion enriched by Pb

was found to be twice as large as in the usual emulsion, although the averaged target mass numbers in both of the mentioned stacks were approximately the same [6].

The statistical theory of fragmentation [8] allows one to estimate the «temperature» $kT$ (or the average excitation energy per nucleon) of the fragmentating nucleus,

$$kT = \frac{A}{A-1}(\sigma_N^2/m_N), \tag{13}$$

where $m_N$ is the nucleon mass, $\sigma_N^2$ is the dispersion of the intrinsic momentum distribution of nucleons that can be calculated using the so-called «parabolic law»,

$$\sigma_\alpha^2 = \sigma_N^2 A_\alpha(A - A_\alpha)/(A-1). \tag{14}$$

Here $A$ is the mass number of the projectile nucleus, $A_\alpha = 4$ is the same for $\alpha$ and $\sigma_\alpha^2 = \langle p_T^2 \rangle/2$, where $\langle p_T^2 \rangle$ can be experimentally measured in the rest system of fragmentating nuclei. We obtain $kT \cong (3 - 3.5)$ MeV for coherent reactions (11), (12) which is considerably (several times!) less than in the reactions of usual multifragmentation at relativistic energies measured in inclusive experiments.

In Figs.3, 4 we show examples of distributions on $p_T^2$ and $\varepsilon_{ij} = \arccos(\mathbf{p}_{T_i}\mathbf{p}_{T_j}/p_{T_i}p_{T_j})$ for the secondary $\alpha$ in the c.m.s. of fragmentating nuclei. Neither of these distributions can be described using the statistical theory of prompt decay. The remarkable features of these spectra are the high-momentum «tail» in $p_T$ and the considerable trend to the coplanarity of $\mathbf{p}_T$ in the transverse plane of the reactions.

Further, it was found that the coplanarity of $\mathbf{p}_T$ depends on the excitation energy of the dissociated nuclei. In Fig.5 we show the dependence of the coplanarity coefficient,

$$C = (N_{\varepsilon_{ij} \le \pi/4} + N_{\varepsilon_{ij} \ge 3\pi/4} - N_{\pi/4 < \varepsilon_{ij} < 3\pi/4})/N_{0 \le \varepsilon_{ij} \le \pi} \tag{15}$$

on $kT$ for reaction (11) at $4.2A$ GeV/c measured in the 2m propane bubble chamber. The coherent channel of (11) only takes place at $kT \le 10$ MeV. In this region, the coplanarity of the transverse momenta of $\alpha$ decreases with increasing $kT$. Then, it reaches its minimum value $C_0 = 0.16$, which corresponds to the case of prompt decay of $^{12}C$ into three alphas, and begins to increase with increasing $kT$ in the incoherent region of high temperatures.

At the same time, the distributions on the relative angles and effective masses of $\alpha$ pairs in reactions (11), (12) display two peaks which can be associated with the decay of the short-lived intermediate states of the $^8Be$ nucleus in the ground ($0^+$) and first excited ($2^+$) states. The relative probabilities of prompt and cascade decay modes also depend on the temperature of the fragmentating nucleus (see an example in Fig.6). The character of the dependencies of the momentum and correlation characteristics of $\alpha$-particles on the nuclear excitation energy agrees with the picture of the transition from the mechanism of

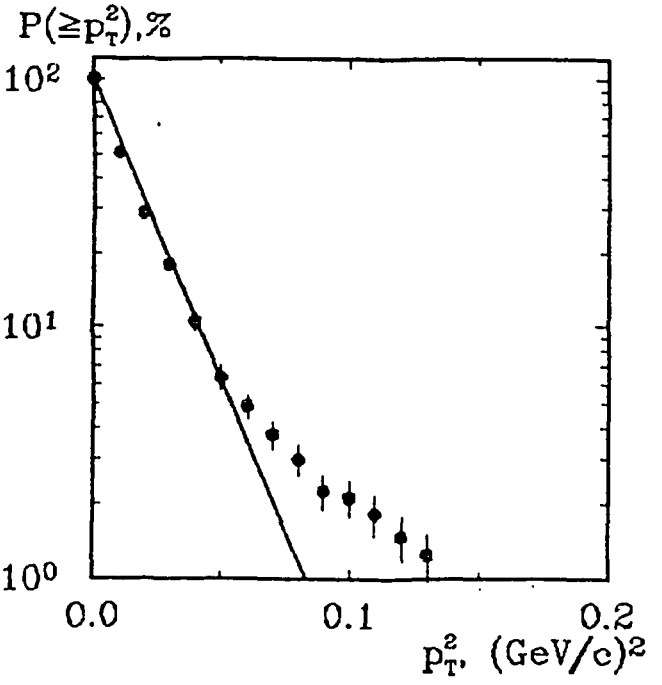


Fig.3. Integral distribution on $p_T^2$ for α from reaction (12). The line is a single Rayleigh distribution with $\langle p_T^2 \rangle = \langle p_T^2 \rangle_{exp}$

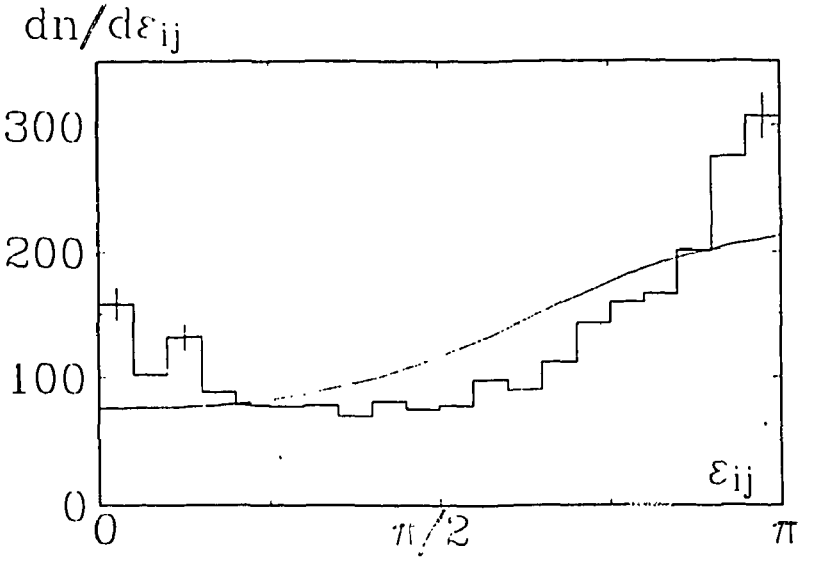


Fig.4. Experimental and calculated (see text) distributions on $\varepsilon_{ij}$ for reaction (12)

sequential binary fission to prompt multifragmentation with a further growth of angular momenta acquired by the fragmentating system during collision with increasing nuclear «temperature».

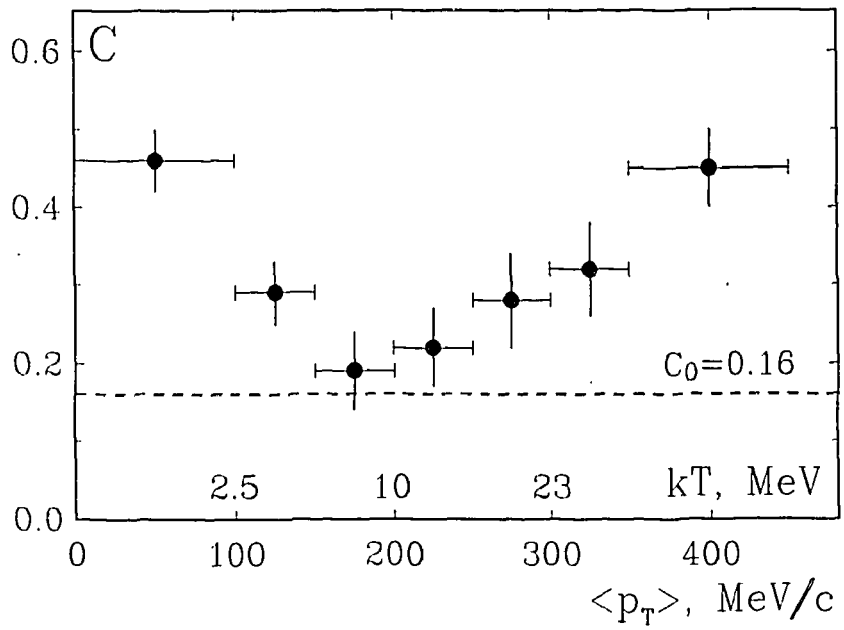


Fig.5. The coplanarity coefficient *vs.* $kT$ for reaction (11) at 4.2$A$ GeV/c

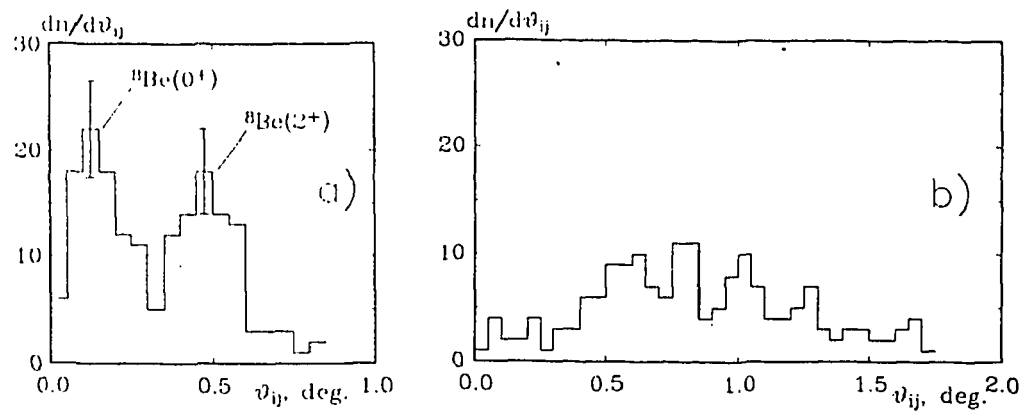


Fig.6. The relative angle distributions for events of coherent reaction (11) with $kT < 2.5$ MeV (a) and $kT > 2.5$ MeV (b)

The whole complex of results of the study of coherent reactions (11) and (12) points to the most favourable conditions for realizing the reactions of coherent multifragmentation of relativistic nuclei for the investigation of nuclear structure and the shape of the nuclear equation of state at small excitation energies, and the study of quasi-nuclear resonances and their interactions with nucleons and nuclei.

The obvious extension of this work is to a directed search for and study of various resonance-like peculiarities in the spectra of relative angles and/or effective masses of fragments — *pp*, *pd*, *pt*, *dd*, *dt*, *pα*, *dα*, etc. — the spectator products of relativistic projectile nuclei. The abundant formation of such «nuclear resonances» in coherent multifragmentation reactions at very small excitation energies augurs well for the future.

## 4. Acknowledgements

I am much indebted to Dr. V.V.Belaga for help during all stages of this work.

## References

1. Pomeranchuk I.Ya., Feinberg E.L. — DAN USSR, 1953, 93, p.439.
2. Chernov G.M. — Proc. XII Int. Sem. on High Energy Phys. Probl., Dubna, Sept.12—17, 1994 and references therein.
3. Chernov G.M. (ABDDEKMPTT-collaboration). — Rad. Measurements, 1995, 25, p.269.
4. Belaga V.V. et al. — ibid., 1995, 25, p.271.
5. Belaga V.V. et al. — JETP Lett., 1995, 62, p.385.
6. Belaga V.V. et al. — Yad. Fiz., 1995, 58, No.11.
7. Avetyan F.A. et al. (ABDDEKMPTT-collaboration). — ibid., 1996, 59, No.1.
8. Goldhaber A.S. — Phys. Lett., 1974, B53, p.306.

Received on November 23, 1995.

*Краткие сообщения ОИЯИ №6[74]-95* *JINR Rapid Communications No.6[74]-95*

УДК 539.123

# SUPERPOSITION OF NEUTRINO EIGENSTATES AND NEUTRINO OSCILLATION

*O.A.Zaimidoroga**

The possibility exists that the weak interaction between neutrino and antineutrino produces states which are superpositions of left-handed neutrino and right-handed antineutrino. This new states do not have well-defined lepton number. The peculiar properties of neutrinos and their oscillation in this case most probable are indicative of the Majorana nature of neutrinos.

The investigation has been performed at the Laboratory of Particle Physics, JINR

## Суперпозиция собственных состояний нейтрино и осцилляции нейтрино

*О.А.Займидорога*

Показано, что в результате слабого взаимодействия между нейтрино и антинейтрино возможно существование таких состояний, которые являются суперпозицией левого нейтрино и правого антинейтрино. Эти новые состояния не имеют определенного лептонного числа. Свойства этих нейтрино и их осцилляции наиболее вероятно свидетельствуют о майорановской природе нейтрино.

Работа выполнена в Лаборатории сверхвысоких энергий ОИЯИ.

One of the fundamental questions in modern physics is: under what conditions can neutrino oscillation occur in the vacuum?

The phenomenon of neutrino oscillation arises from a mismatch between the weak eigenstates and the eigenstates of neutrino mass [1]. In the case of possibly massive neutrinos the relative phase change between the mass eigenstates with time can show an oscillation pattern [2]. This oscillation is extremely sensitive to the mass of the neutrino and the mixing angle.

In this paper the study of neutrino oscillation is made taking into consideration the superposition of neutrino and antineutrino eigenstates. Analogously to $K$-meson mixing, this oscillation is not sensitive to the mass of neutrino but to the mass difference of the new states produced and not having a well-defined lepton number.

Let's consider a two-state quantum-mechanical system having identical quantum numbers, characterized by a Hamiltonian $H$. The initial states $S_1$ and $S_2$ will develop in time following the evolution equation:

$$ih\frac{\partial S_1}{\partial t} = H_1 S_1 \quad \text{and} \quad ih\frac{\partial S_2}{\partial t} = H_2 S_2.$$

The solutions of these equations are:

*e-mail: zaimidoroga@mi.infn.it and oleg@ljap5.jinr.dubna.su

$$S_1 = k_1 \exp(-iH_1 t/h), \qquad S_2 = k_2 \exp(-iH_2 t/h).$$

Each of those states would phase-rotate in its own eigenstate. Let's now assume an interaction term in the Hamiltonian in the form:

$$ih\frac{\partial S_1}{\partial t} = HS_1 + aS_2 \quad \text{and} \quad ih\frac{\partial S_2}{\partial t} = HS_2 + aS_1.$$

The amplitudes of states $S_1$ and $S_2$ starting from a state $S_1(t=0)$ are given by: $S_1(t) = \exp(-iHt/h)\cos(at/h)$; $S_2(t) = \exp(-iHt/h)\sin(at/h)$. The new states $(S_1 + S_2)$ and $(S_1 - S_2)$ will have different eigenvalues $(H + a, H - a)$. This system will permanently move from state $S_1$ to $S_2$ and back.

Let's now consider two states having different quantum numbers. If an interaction exists between these states, the time evolution of the system will be described by a linear superposition of states and will not have a well-defined relevant quantum number. A more familiar example is that of $K^0$ and $\overline{K}^0$-oscillation [4]. Under the action of weak interaction the original strong interaction eigenstates of $K^0$ and $\overline{K}^0$-mesons are mixed. The weak eigenstates in this case are the linear superpositions of $K^0$, $\overline{K}^0(K_1, K_2)$. If both $K_1$ and $K_2$ mesons were stable particles, then $K_1$ and $K_2$ would each evolve with respect to its own Hamiltonian and after time $t$ the relative phase $K_1$ and $K_2$ (present in the original $K^0$, $\overline{K}^0$-states) would have changed. The new states would thus be the new linear combination of $K^0$, $\overline{K}^0$ and these states would also not have well-defined strangeness. The relative phase change of $K_1$, $K_2$ with time will be the result of this oscillation. In reality the weak interaction also causes the decay of $K_1$, $K_2$. Due to the action of the weak interaction $K_1$, $K_2$ mix and CP-violation occurs. Owing to the decays of $K_1$, $K_2$ the relative amplitude of $K_1$, $K_2$ present in the original $K^0$, $\overline{K}^0$-mesons would change with time. So not only the relative phase but also amplitude of $K_1$, $K_2$ in $K^0$, $\overline{K}^0$ mesons change with time. Under the weak fermion interaction a pair of $s$-quarks converts into a pair of d-quarks and back. The CP-noninvariant interaction gives rise to $K_1$, $K_2$ mixing, while the CP-invariant part of this interaction contributes to the mass difference.

An important aspect of the phenomenon is that the interaction connecting two neutral states with different quantum numbers violates the conservation laws involved and, due to that the superposition transition can appear. The mixing may not take place if interaction is forbidden. For instance, conservation of electrical charge forbids the oscillation between a proton and an antiproton.

Thus, the superpositional states will appear if the base states are neutral and are of equal masses and an interaction between this states violates those quantum numbers that aren't their eigenvalue. This is not the case for the neutrino. Electron-type of neutrino cannot be coupled to a muon-type of neutrino, unless an interaction exists, which violates lepton numbers. This interaction would play for neutrinos the same role as weak interaction plays for kaons. But we know that lepton numbers conserve to a very high degree. Now one needs to clarify which kind of coupled states could be between two neutrino states taking into account the fact that neutrinos are fermions. The weak eigenstates of neutrinos do not coincide with the mass eigenstates, and due to that the components of weak eigenstates can be expressed in terms of the mass eigenstates as:

$$\nu_i = \sum u_{ij}^{*} \nu_j \,. \tag{1}$$

Eigenstates of neutrinos in the limit in which the neutrino mass is degenerate would be coherent and could therefore interfere. If the masses of the different eigenstates were too far apart, then the velocities would so differ that the states could lose the interference picture. The time evolution of the neutrino can be described by the coherent sum:

$$\nu_i(t) = \sum_{j=1}^{N} \exp\left((-i\sqrt{p^2 + m_\nu^2})\, t\right) u_{ij}^{*} \nu_j \,. \tag{2}$$

One does not detect the individual terms in (2) but their linear combination corresponding to certain weak eigenstates. Only eigenstates of $\nu$ and $\bar{\nu}$ preserve the interference pattern. The way to detect neutrinos and possible neutrino oscillations is through its weak interaction. So, two neutral degenerate levels of neutrino and antineutrino of definite flavour under the action of weak interaction can be described by a linear superposition of states neutrino and antineutrino. This system will continuously move from the left-handed state to the right-handed and vice versa. So, a neutrino of definite flavour, produced at $t = 0$, with respect of (1) can be expressed by a linear superposition of the left-handed neutrino and right handed antineutrino. These new states will not have a well-defined chirality, since they are linear combinations of left and right chiral projections. However, they can be eigenstates of helicity ($\sigma * \mathbf{p}/p$). Obviously, for zero mass, helicity and chirality eigenstates coincide. If the mass is non zero the chirality will differ from the helicity by the term $m_\nu^2/E^2$. In the case of Dirac type of neutrinos the opposite chirality transitions between neutrino and antineutrino are suppressed by a factor $m_\nu^2/E^2$. The suppression is related to the helicity and fermion number conservation [5]]. For the Majorana type of neutrinos there is no helicity violation because the Majorana condition requires a neutrino to consist of a left-handed 2-spinor together with a charge conjugate right-handed one. The mixing of two degenerate levels in the vacuum must result in level splitting. These new levels would have definite CP-parity.

$$\nu_1 = \frac{\nu + \bar{\nu}}{\sqrt{2}} \quad \text{and} \quad \nu_2 = \frac{\nu - \bar{\nu}}{\sqrt{2}} \,.$$

Those states after a time t will have:

$$\frac{1}{\sqrt{2}} [\nu_1 \exp(-im_1 t - \Gamma_1 t/2) + \nu_2 \exp(-im_2 t - \Gamma_2 t/2)].$$

If both states were stable ($\Gamma_1 = \Gamma_2 = 0$), then after $t = \pi/\delta m_{12}$ the beam of neutrino would consist of antineutrinos. After another time interval the beam of antineutrinos would change chirality and would consist of neutrinos. The new states thus reached could now be a new linear superposition of neutrino and antineutrino. Experiments of this type make it possible to determine the mass difference $\delta m_{12}$. Two states $\nu_1$ and $\nu_2$ are eigenstates of CP-parity. If they were both unstable, then under the action of the weak interaction they could be mixed with and violate the CP-parity. Such oscillations would be suppressed by exponential damping due to $\Gamma_{12} \neq 0$. The probability will be:

$$P_{\nu_1 \rightleftarrows \nu_2}(t) = \frac{1}{4} \{ \exp(-\Gamma_1 t) + \exp(-\Gamma_2 t) \pm 2 \exp[-(\Gamma_1 + \Gamma_2)\, t/2] \cos \delta m_{12} t \} \,.$$

The mass difference $\delta m_{12}$ does not depend on the mode of decay. Because of small phase space available for the $\nu_1$, $\nu_2$-decays, one expects the width, $(\Gamma_1 + \Gamma_2) \geq \delta m_{12}$, to enhance transition.

So, the transformation of left-handed neutrinos to right-handed antineutrinos and vice versa forms the objects having only two independent components. This transition violates lepton number by two units and conserves CP-parity. The Majorana nature of neutrino oscillation is most probable. Recently there was observed semileptonic decay of tau-lepton claimed for the Majorana type of neutrino [6].

From the foregoing consideration, it is seen that two Majorana neutrinos $\nu_1$ and $\nu_2$ probably would have a tiny mass difference as a result of $\Delta L = 2$ transition. For the detection of ν-oscillation one considers the so-called «appearance experiments» to look for the presence of antineutrinos in ν-beam or vice versa. It is obvious that the ability to detect ν-oscillations depends on the mass difference of Majorana neutrinos $\nu_1$ and $\nu_2$ and they would be stable or unstable particles. If neutrinos $\nu_1$, $\nu_2$ were stable, then after time $\pi/\Delta m_{1,2}$ two fluxes will appear: of neutrino and of antineutrino. The aim is to measure the flux of neutrino of opposite sign at different distances from the source. The mass difference can be measured directly in this case. To perform an experiment the detector has to be sensitive to both signs of neutrino. For example: if source is the source of antineutrino, then one needs to detect the flux of antineutrino at given distances via inverse beta reaction:

$$\tilde{\nu} + p \to n + e^+$$

and elastic scattering

$$\tilde{\nu} + e \to \tilde{\nu} + e.$$

If no oscillation is present, then the ratio $N\tilde{\nu}p/N\tilde{\nu}e$ will be constant for any distances. If oscillation is present, then the ratio $N\tilde{\nu}p/(N\tilde{\nu}e + N\nu e)$ would be function of $\Delta m_{1,2}$. To verify this, ν-oscillation can be detected in laboratory from high-intensity beta source or accelerator. Another possibilities are in solar neutrino detection. Antineutrinos are not predicted by any solar model, thus observation of antineutrino would be of major significance. To explain deficit of solar neutrino flux, the mass difference has to be $< 10^{-17}$ MeV–$10^{-19}$ MeV. Study of ν–$\tilde{\nu}$ oscillation can be also done with short- or long-baseline neutrino experiments. If $\nu_1$, $\nu_2$ are unstable particles, the yield of neutrinos of opposite sign would depend upon branching ratio of decay mode to different types of neutrinos and $\Gamma/\Delta m_{12}$ ratio.

This work was supported by the I.N.F.N. of Milano, Italy under contract number 003709.I would like to acknowledge Prof. G.Bellini for his kind hospitality and support. I wish to thank P.Ratcliff and V.Strakhovenko for their critical reading of the manuscript.

References

1. Cabibbo N. — Phys. Rev. Lett., 1953, 10, p.532.
2. Pontecorvo B. — Sov. JETF, 1957, 33, p.549;
   Bilenky S., Pontecorvo B. — Phys. Rev., 1978, 41C, p.255.
3. Majorana E. — Nuovo Cimento, 1937, 14, p.171.
4. Okun L. — Leptons and Quarks, North-Holland Publishing Company, 1987.
5. Bahcall J., Primakoff H. — Phys. Rev., 1978, D18, p.3413.
6. Bartelt J. et al. — Phys. Rev. Lett., 1994, 73, p.1890.

Received on September 19, 1995.

*Краткие сообщения ОИЯИ №6[74]-95* *JINR Rapid Communications No.6[74]-95*

УДК 539.1, 0.74.2;
51-72: 539.12

# SIMULATION RESULTS AND SUGGESTIONS FOR POSSIBLE DESIGN OF GASEOUS SHOWER MAXIMUM DETECTOR FOR THE ENDCAP ELECTROMAGNETIC CALORIMETER FOR THE STAR EXPERIMENT AT RHIC

*G.Averichev, S.Chernenko, E.Matyushevskiy, Yu.Minaev, Yu.Panebratsev, E.Potrebenikova, D.Razin, S.Razin, L.Smykov, G.Škoro, A.Shabunov, I.Tsvetkov, V.Yurevich, Yu.Zanevskiy*

The Monte Carlo simulation of Shower Maximum Detector (SMD) for the endcap EMC has been performed for *pp*, *p*Au and AuAu collisions. A conceptual design of gaseous SMD with a pad readout of signals is proposed.

The investigation has been performed at the Laboratory of High Energies, JINR.

## Моделирование и возможные реализации газового детектора максимума ливня торцевого электромагнитного калориметра установки STAR на ускорителе RHIC

*Г.Аверичев и др.*

Проведено моделирование детектора максимума ливня торцевого электромагнитного калориметра для *pp*, *p*Au и AuAu столкновений. Предложен газовый детектор максимума ливня с катодной плоскостью, имеющей pad-структуру.

Работа выполнена в Лаборатории высоких энергий ОИЯИ.

## 1. Introduction

In our previous report [1] we presented the results of Monte Carlo simulations of endcap EMC Shower Maximum Detector (SMD) for the STAR and experimental investigations of characteristics of the Russian tiny photomultipliers PMT in order to specify their applicability in the SMD. Our results show that the scintillator strip/fiber SMD is good option for the endcap SMD in the case of *pp* and *p*Au collisions. Application of Russian tiny PMT with low gain allows us to build relatively low-cost SMD with low number of high voltage supply channels. But, one of the most important conclusions of our previous work [1] was that this type SMD is not suited for the job in the AuAu collision case. In what follows, we present results of our MC calculations and main ideas about the conceptual design of SMD for endcap EMC with a pad readout of signals.

## 2. Monte Carlo Simulations

2.1. *SMD Parameters.* The CERN Monte Carlo program GEANT3.15 with a 1 MeV cut for $\gamma$'s and electrons was used to study EM showers for full STAR detector, and HIJING model event generator has been used for describing of proton-nucleus and nucleus-nucleus collisions.

During the MC simulations the SMD was placed at the depth of $5X_0$ in the endcap EMC and consisted of two scintillation rings (inner radius — 75 cm, outer radius — 232 cm, thickness — 6 mm).

In Fig.1 the pseudorapidity distributions of $\gamma$'s and charged hadrons in *pp*, *p*Au and AuAu collisions are presented. The distributions of energies for direct gammas and gammas from $\pi^0$ decays in acceptance of the endcap EMC are shown in the right side of this picture. The number of $\gamma$'s in the SMD acceptance is about 800 for central AuAu collision and about 10 in central *p*Au collision.

Scatter plot of shower charged particles distribution on the first SMD layer is presented in Fig.2a. In Fig.2b we show the number of this particles as a function of the distance $R$ from the SMD centre. It is seen that about 75% of showers, produced in the interactions of primary $\gamma$'s (about 600) with the calorimeter matter, lie in the central ($75 < R < 160$ cm) SMD region.

The same distributions for the primary gammas with energy above 500 MeV are presented in Fig.3. Comparison of Fig.2 and Fig.3 tells us that the contribution of showers, induced by gammas with energy lower than 500 MeV, is practically negligible, and we can conclude that the main sources of background (for observation of direct $\gamma$'s) are hadrons and gammas with energy higher than 500 MeV.

Figure 4 shows the transverse profiles of shower, induced by 15 GeV gamma on the middle part of the first and second layer of SMD at the pseudorapidity $\eta \simeq 1.5$. RMS of the shower transverse profiles is about 2.3 cm. This means that the granularity of the SMD must be better than 10—12 mm for both layers in order to identify and separate the showers. The IHEP group experimental data [2] confirm our conclusion.

To obtain a uniform deposited energy over full surface of SMD layer, we have account for dependence of deposited energy on the radius $R$ in the central SMD region ($75 < R < 160$) cm. We can see that for $R > 160$ cm deposited energy practically does not depend on the distance $R$. The data for the central SMD region were used for the fitting procedure and the fitted function was of the form $\Delta E = a + b \cdot R$. The results of the fit were used to determine the width of the inner ring strips, taking into account that the widths of outer strips are equal to $\Delta R \simeq 12$ mm. The total number of ring strips defined in such manner is 190. The total width of the central ring strip is 4 mm.

The next step was a determination of a number of strips in the azimuthal direction and, as a result, we have practically defined the pad structure of the SMD layer. In Fig.5 is shown the energy deposited in the central 6 cm width ring of SMD vs. azimuthal angle for 6°, 3° and 1° per bin for the central AuAu collision. The width of 6 cm corresponds to the full width at 1/10 th of maximum height of the shower transverse profile. The 1° azimuthal angle bin corresponds to the geometrical size of ~13 mm in the central part of SMD and using these pads we can clearly identify the single shower. Referring to Fig.5a and Fig.5b one sees that all showers are separated with the 3° azimuthal angle widths pads. Finally, the proposed pad structure of the first SMD plane gives us the possibility of separating showers

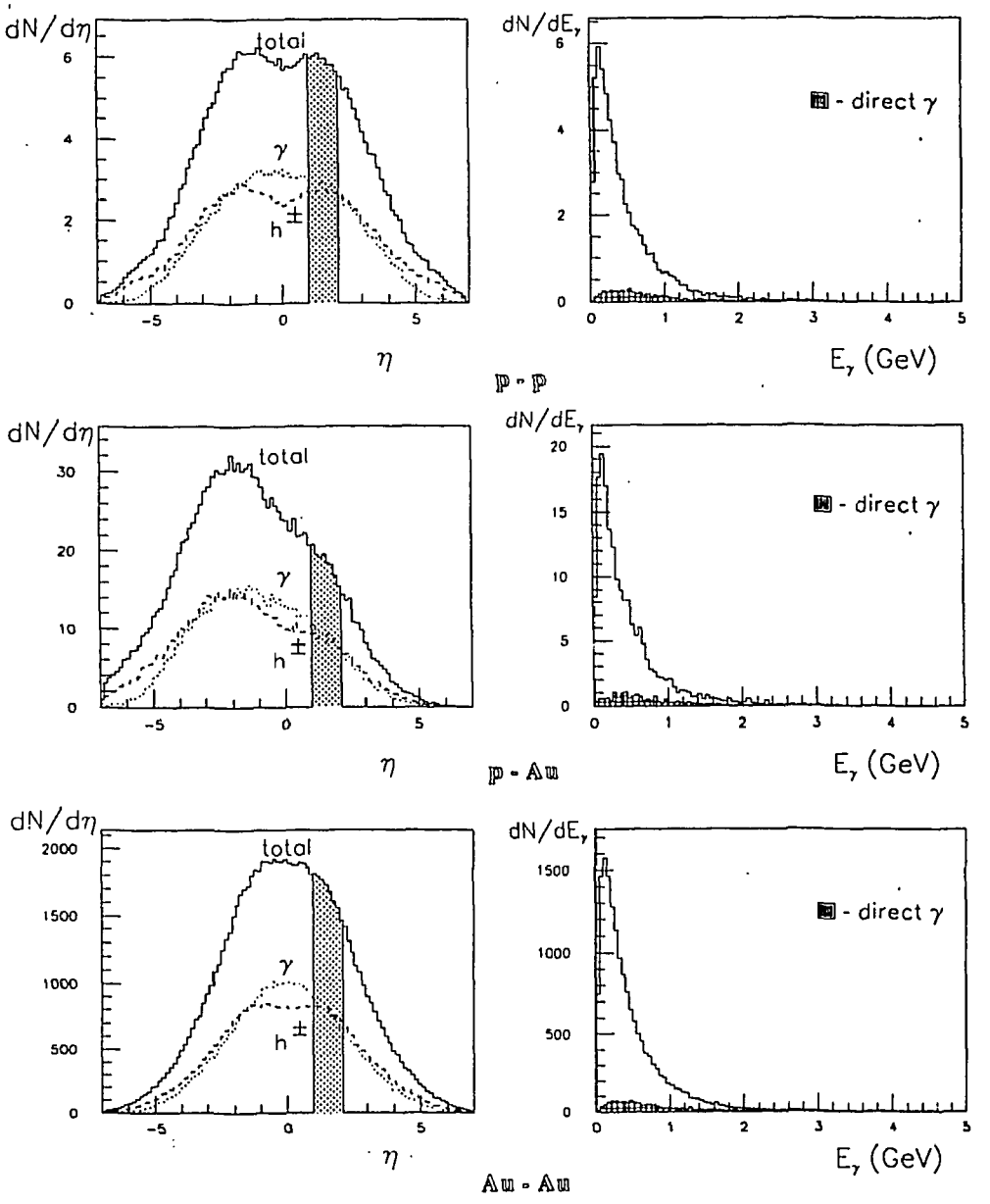


Fig.1. The pseudorapidity distribution of γ's and charged hadrons in *pp*, *p*Au and AuAu collisions at 200 GeV/nucelon

in the central SMD region using the information about two coordinates ($R$ and φ). But we would like to point out that for separating the showers in the outer part of the SMD the information about φ coordinate from the second plane (wires or strip with 10 mm step, for example) is needed.

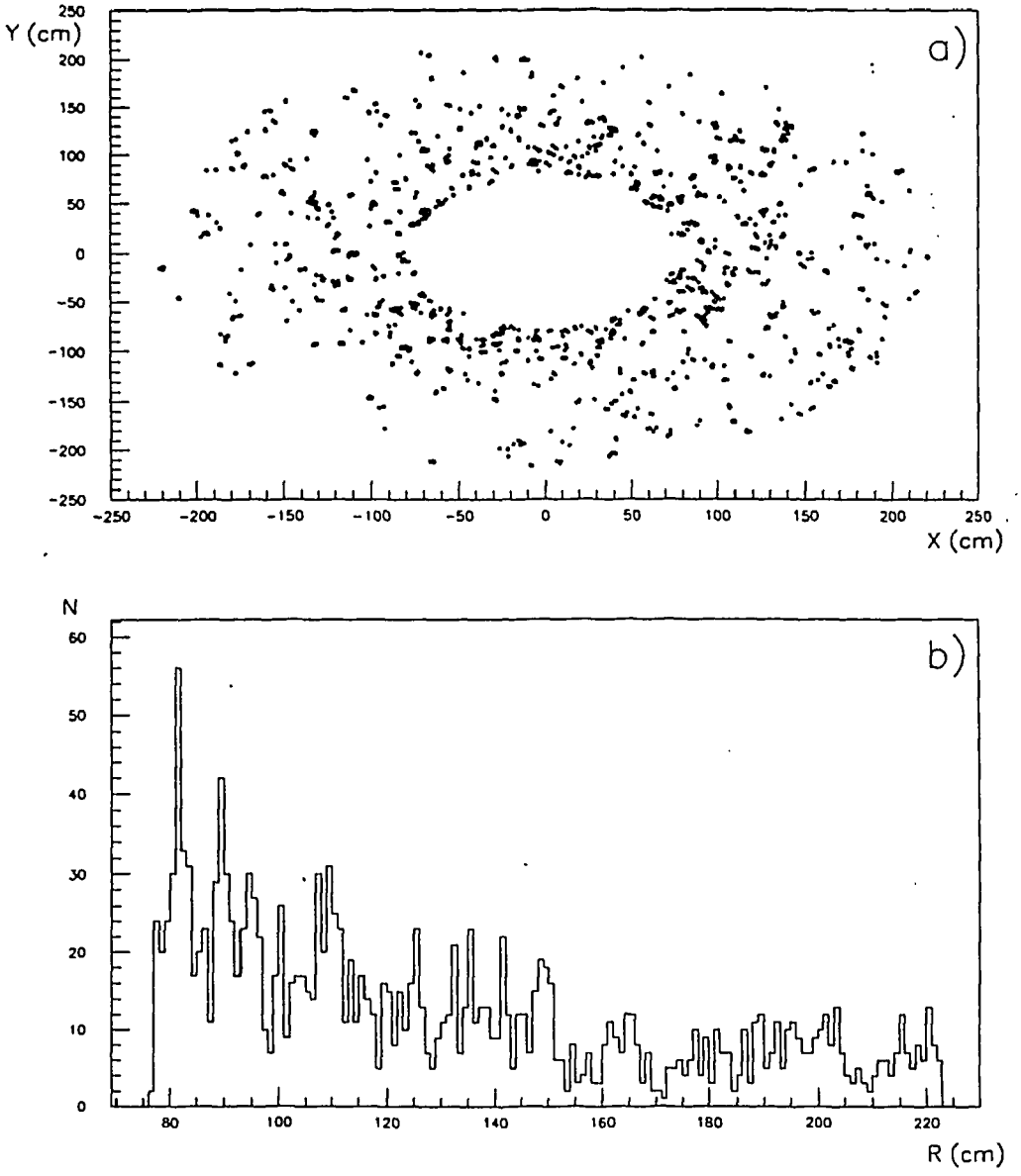


Fig.2. (a) Scatter plot of shower charged particles distribution on the first SMD layer; (b) The number of shower charge particle vs. the distance from the SMD centre

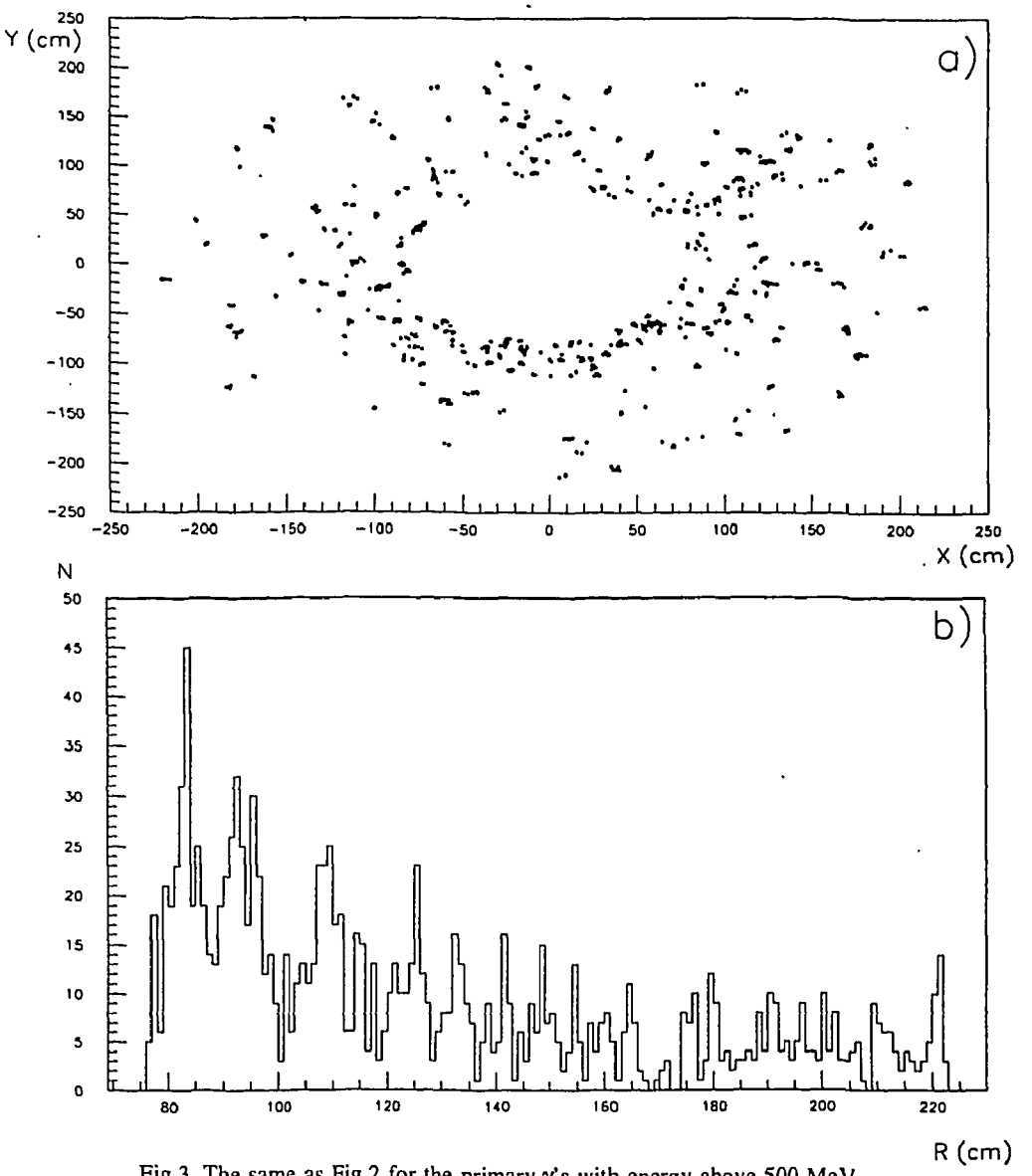


Fig.3. The same as Fig.2 for the primary γ's with energy above 500 MeV

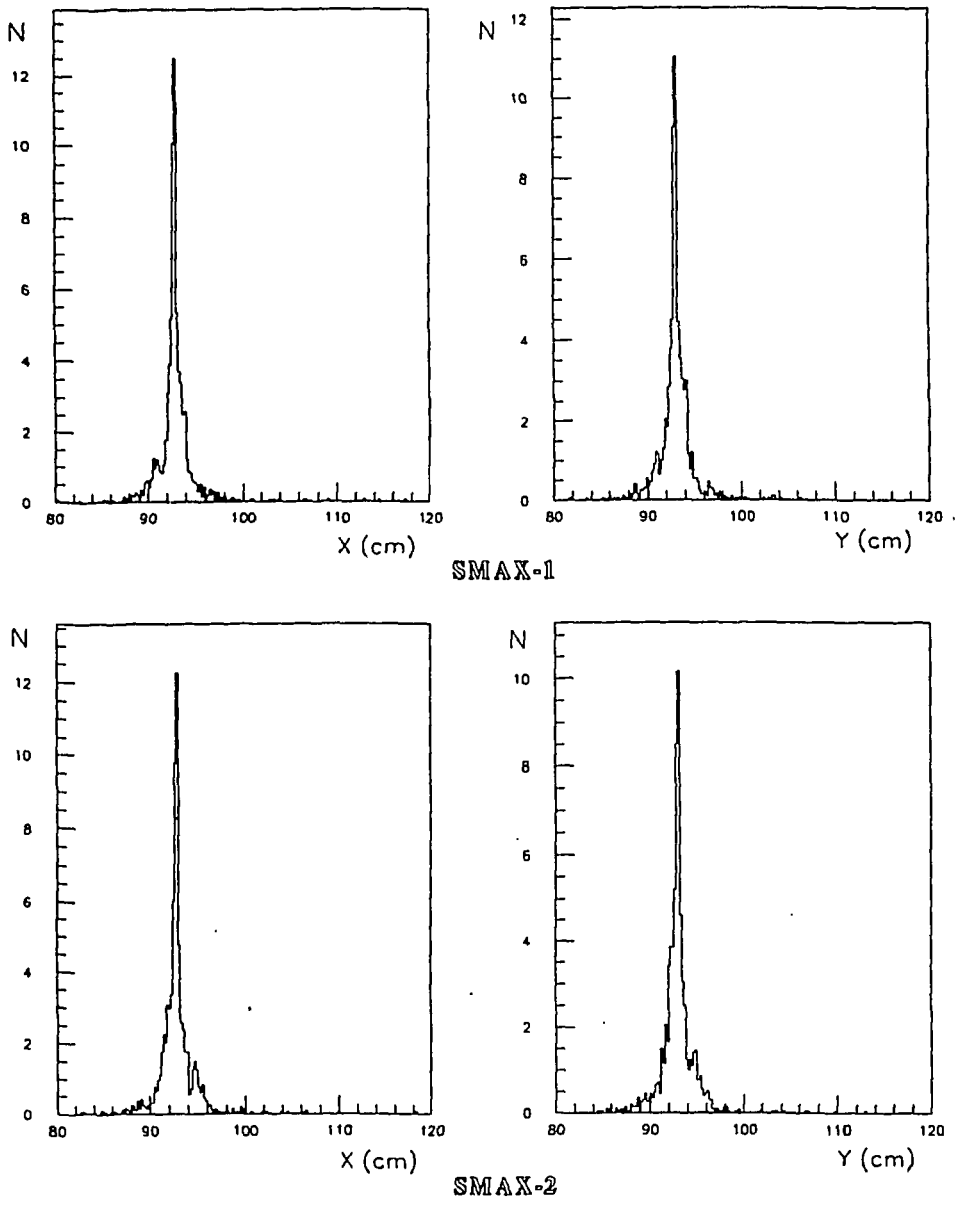


Fig.4. The transverse profiles of shower, induced by 15 GeV gamma

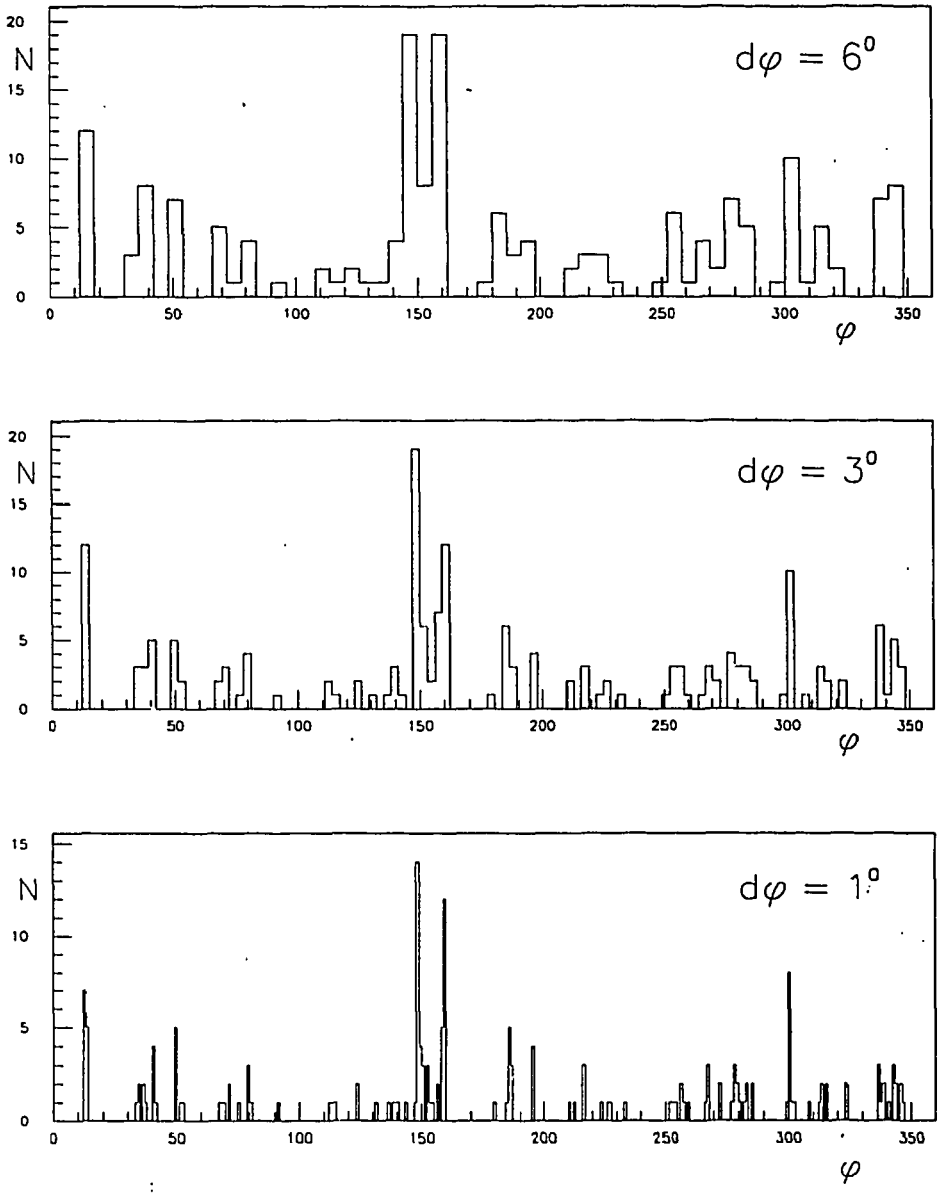


Fig.5. The energy deposited in the central 6 cm width ring of SMD vs. azimuthal angle for 6°, 3° and 1° per bin for the central AuAu collisions

2.2. $\pi^0/\gamma$ *Separation.* We have, also, carried out a study of the separation of shower coming from single $\gamma$ from those coming from a $\pi^0$ decay. In our calculation we considered a SMD with only one sensitive plane with the pad structure, described above. We used a procedure similar to the method, described in [3]. Three variables were used to find a coefficient of $\pi^0$ rejection for 90% $\gamma$ acceptance:

— $E$ — the energy deposited by the shower;

— $r$ — the energy weighted shower radius;

— $Er^2$ — the energy dispersion of the shower.

The energy weighted centre of the shower is calculated as follows:

$$X_c = \sum_i x_i / \sum_i E_i ,$$

where $E_i$ is the energy deposited in the ith pad and $X_i$ is the position coordinate of the ith pad in the pad units. The energy weighted shower radius, $r$, is calculated as:

$$r = \sum_i D_i E_i / \sum_i E_i ,$$

where $D = |X_c - X_i|$ is the distance of the ith pad from the calculated centre of the shower. The energy dispersion of the shower is calculated as:

$$Er^2 = \sum_i E_i D_i^2 .$$

Figure 6 shows the scatter plot of the energy dispersion $Er^2$ vs. the wighted shower radius $r$ for 100 showers initiated by 15 GeV $\gamma$'s and $\pi^0$'s in the middle part of the SMD ( rapidity $\eta \approx 1.5$). The energy summation was taken over 15 pads in radial and 10 in azimuthal directions from calculated centre of the shower. The marked area in Fig.6a contains 90% of the single $\gamma$ showers. In the scatter plot for $\pi^0$ initiated showers the area of 90% single $\gamma$ efficiency is marked. The showers within this area are classified as showers initiated by $\gamma$'s, while all showers outside this area — as $\pi^0$ initiated showers. The $\pi^0$ rejection efficiency is given by the percentage of $\pi^0$ initiated showers which are outside this area. In this case we have obtaned the $\pi^0$ rejection efficiency of 63%. The results of the similar calculations for the SMD with two sensitive plans consisted of 1 cm width scintillator strips are shown in Fig.7. The value of the $\pi^0$ rejection efficiency is 60% in this case. It is seen, that for the SMD with only one pad-type sensitive plane we get practically the same $\pi^0/\gamma$ separation as for the SMD with two strip-type planes.

The future investigations are needed in this direction. In our opinion the information about the $\varphi$ cooridnate from second SMD plane will significantly improve the efficiency of $\pi^0/\gamma$ separation.

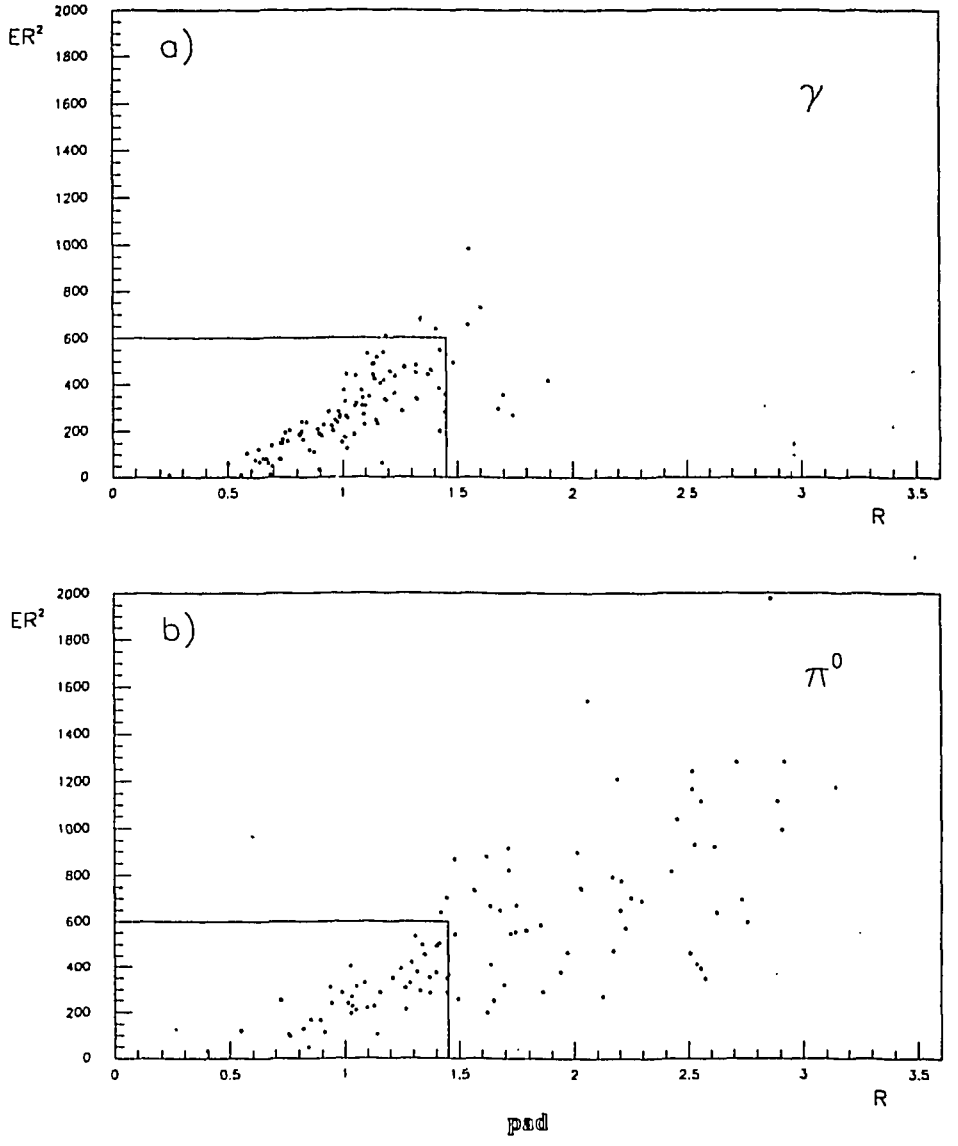


Fig.6. The scatter plot of sample of 15 GeV γ initiated showers as a function of the energy dispersion $Er^2$ and the weighted shower radius $r$ for the SMD with one pad sensitive layer

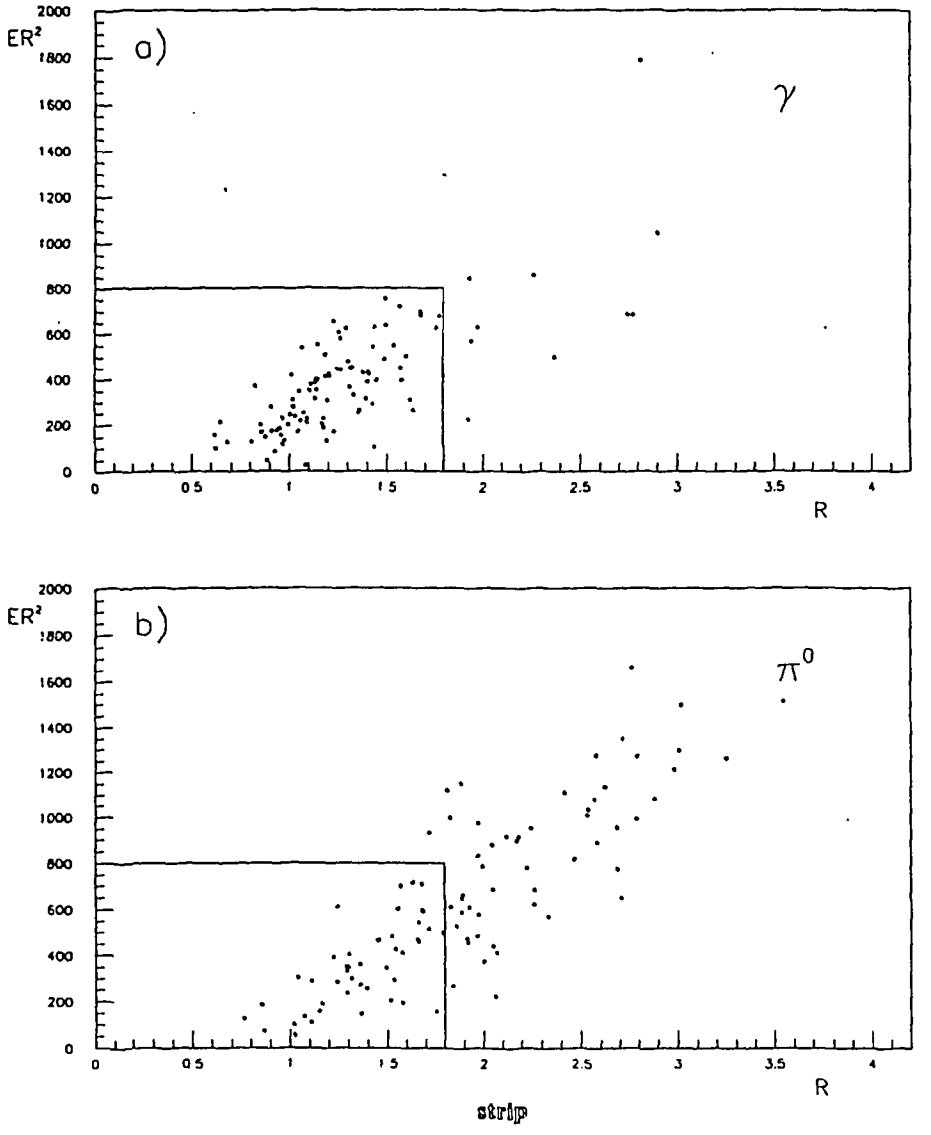


Fig.7. The same as in Fig.6 for the SMD with two strip sensitive layer

## 3. Conceptual Design

Following by the Monte Carlo calculation results we proposed to use as an option of SMD a thin multiwire gas chamber with analog readout of anode wires and of cathode pads to measure the position of EM showers. The analog readout is sensitive to the density of particles inside the shower, thus providing a localization of the shower core by a simple determination of the weighted centre in a cluster of signals. We adopt OPAL [4] and CDF [5] groups methods in our proposal. The thin multiwire gas chambers, operating in a satured mode, were used for electromagnetic presumpling in the endcaps of OPAL detector at LEP [4]. At Fermilab for the Collider Detector Facility the shower counter strip chambers were used operating with the gain of $10^4$ [5].

The proposed SMD multiwire gas chamber will be CDF or OPAL-type chamber with pad structure of cathode as followed from MC simulations.

3.1. *Description of Detector.* Space and timing restrictions are the major concern for detector design. It is proposed that the SMD will be inserted into 25 mm gap into the endcap EMC at the depth of $5 \div 7X_0$. It will consist of 12 trapezoidal sectors each of which covers 30° azimuthal angle. The geometrical dimensions are given in Fig.8. A schematic view of the cross section of two chambers is shown in Fig.9 and Fig.10.

In the OPAL-type chamber (Fig.9) the anode wire plane consists of 637 gold coated tungsten W-Re wires of 30 μm diameter rounded on the supporting frame with space step of 2 mm in the direction along the sector axes line. Groups of five wires are then ORed. The wires strung with a tension of about $80 \div 100$ g. Long wires are supported every 60 cm by spacers to avoid sagging and to provide a mechanical strength for the chamber itself. The dead space loss due to this support is less than one per cent.

The CDF-type chamber (Fig.10) has a ribbed construction. Aluminum ribs profile will be producted using the extrusious technology. The anode wires are placed at the centre of cells with the step of 1 cm by means of special supporting plates. The individual anode wire is connected to high voltage by 1 MΩ resistor and readout through capacity of $200 \div 400$ pF.

The cathode planes of chambers are 1.5 mm thin G10 sheets of whose internal faces (forward wires) copper pads are formed by chemical etching.

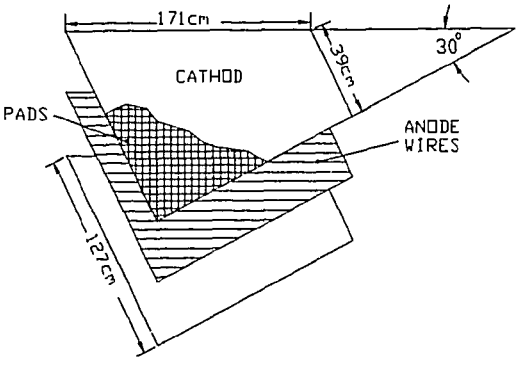


Fig.8. Layout and dimensions of the SMD multiwire gas chamber

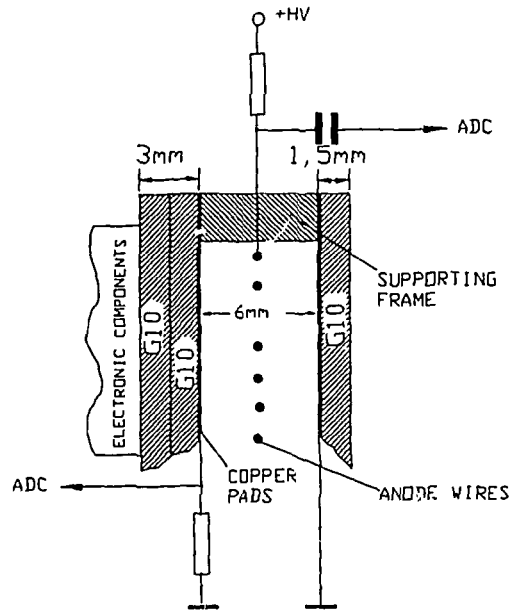


Fig.9. Schematic view of cross section of the OPAL-type SMD multiwire gas chamber

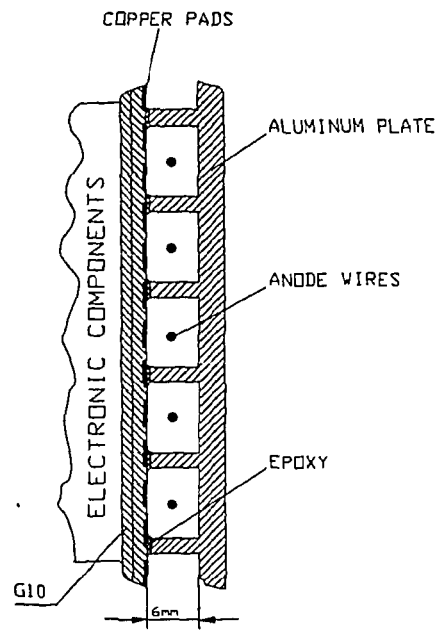


Fig.10. The same as in Fig.9 for the CDF type chamber

Following by the results of MC calculations it follows that there are 190 bins in radial and 10 bins in azimuthal directions, total — 1900 pads. The size of the pads decreases going towards the beam axes to resolve ambiguites due to increasing multiplicity. The cathode plane is placed at the distance of 3 mm from the anode wire plane.

The full cathode plane consists of a few pieces. These pieces are glued in turn to the face of G10 sheet to obtain the full cathode plane of the SMD sector. This cathode plane is glued to the ribs aluminum plate (CDF-type chamber) or pressed to the supporting frame (OPAL-type chamber). The outer face of cathode is used for readout electronics components. The gas mixture argon — DME or argon — $CO_2$ will be used.

3.2. *Readout Electronics.* The two space coordinates are provided by the simultaneous readout of wires pads. This results in a total 2027 electronic channels per sector and 24324 channels for full endcap SMD. All channels have multiplexing analog readout. The front end electronics is directly mounted onto the outer face of the cathode plane. A shielded TWP cable is used to transport the signals to the rear end. At the rear end additional multiplexing will be obtained in the ADC module. 12 bit charge sensitive ADC will be enough to cover a dynamic range from minimum ionizing particles up to showers.

## 4. Conclusion

Our Monte Carlo calculation results show that the Shower Maximum Detector with pad structure of sensitive layer has more suitable properties than the corresponding strip type especially in the case of investigation of the EM showers in the AuAu collision. Good position resolution and $\pi^0/\gamma$ shower separation are realized even with only one sensitive SMD layer used. The estimates indicate that it is possible to build the SMD as a pad multiwire chamber which will have an acceptable cost.

## 5. Acknowledgements

The authors are grateful for support by the Russian Fundamental Science Foundation under grant 95-02-05061 and the RHIC Department at BNL under contract 776746.

## References

1. Design and Study of Light Readout System for Scintillator Shower Maximum Detector for EMC Endcap. STAR Note 226, submitted to JINR Rapid Communications.
2. Akimenko S.A. et al. — IHEP Preprint 94-94, Serpukhov, 1994.

3. Grunhaus J., Kananov S., Milstene C. — Nucl. Instr. and Meth., 1995, A354, pp.368—375.
4. Beard C. et al. — Nucl. Instr. and Meth., 1990, A286, pp.117—127.
5. Nodulman L. — Nucl. Instr. and Meth., 1980, 176, pp.345—347;
Balka L. et al. — Nucl. Instr. and Meth., 1988, A267, pp.272—279.

Received on December 6, 1995.

УДК 539.128.417

# ОПРЕДЕЛЕНИЕ РАЗМЕРОВ ОБЛАСТИ ИСПУСКАНИЯ ПИОНОВ В *np*-ВЗАИМОДЕЙСТВИЯХ ПРИ $P_n = (5{,}2 \pm 0{,}16)$ ГэВ/с С ПОМОЩЬЮ МЕТОДА ИНТЕРФЕРЕНЦИОННЫХ КОРРЕЛЯЦИЙ ТОЖДЕСТВЕННЫХ ЧАСТИЦ

*В.Л.Любошиц, В.Н.Печенов, Е.Б.Плеханов, М.И.Подгорецкий, Ю.А.Троян, А.Ю.Троян*
*Объединенный институт ядерных исследований, Дубна*

*В.Н.Пенев, А.И.Шкловская*
*Институт ядерных исследований и ядерной энергетики БАН, София*

*С.Г.Аракелян*
*Физический институт им.П.Н.Лебедева РАН, Москва*

На основе метода интерференционных корреляций тождественных частиц определены размеры области испускания пионов в *np*-взаимодействиях при импульсе нейтрона $P_n = (5{,}2 \pm 0{,}16)$ ГэВ/с. При анализе использовался экспериментальный материал, содержащий 48570 пар тождественных пионов из 5-лучевых звезд, который был получен при облучении 1-метровой водородной камеры ЛВЭ пучком квазимонохроматических нейтронов. В параметризации Гольдхабера эффективный радиус оказался равным $R = (1{,}30 \pm 0{,}16)$ фм. При обработке использовались два типа фонов: комбинации нетождественных пар $\pi^+\pi^-$ и фон, построенный с помощью предложенного нами способа перемешивания с минимальным нарушением кинематических корреляций. В обоих случаях получились совпадающие результаты.

Работа выполнена в Лаборатории высоких энергий ОИЯИ.

# Determination of the Sizes of the Pion Emission Region in *np*-Interactions at $P_n = (5.2 \pm 0.16)$ GeV/c Using the Interference Correlation Method for Identical Particles

*V.L.Lyuboshitz et al.*

The sizes of the pion emission region in *np*-interactions at $P_n = (5.2 \pm 0.16)$ GeV/c were determined by means of the method of the identical particle interference correlations. The experimental material involving 48570 pairs of identical pions from 5-prong stars, which was obtained at the irradiation of 1m hydrogen chamber of LHE (JINR) by the beam of quasi-monochromatic neutrons, has been used for the analysis. The effective radius for Goldhaber's parametrization is $R = (1.30 \pm 0.16)$ fm. In processing we have used two types of the background: the combinations of non-identical pion pairs ($\pi^+\pi^-$) and the backgroud constructed by means of our method of mixing with «the minimal violation of kinematical correlations». In both the cases the identical results were obtained.

The investigation has been performed at the Laboratory of High Energies, JINR.

## 1. Введение

Первая статья об интерференции тождественных пионов в рамках статистической модели была опубликована Г.Гольдхабером и др. в 1960 г. [1]. Метод определения размеров области испускания пионов, основанный на исследовании интерференционных корреляций тождественных частиц и получивший в последние годы широкое распространение, был разработан Г.И.Копыловым и М.И.Подгорецким [2,3] и затем развит в ряде работ (см., например, [4—8]).

Проблеме определения пространственно-временных параметров области множественной генерации частиц посвящено огромное число экспериментов (см. обзоры [9—12]). Большинство из них выполнено в адрон-ядерных и ядро-ядерных взаимодействиях. Исследований, относящихся к взаимодействию элементарных частиц в области энергий в несколько ГэВ, сравнительно немного.

Предлагаемая работа — первая, где проведена оценка размеров области испускания пионов в *пр*-взаимодействиях.

## 2. Материал

Мы представляем данные с 1-метровой водородной пузырьковой камеры ЛВЭ ОИЯИ, облученной пучком квазимонохроматических нейтронов с импульсом $P_n = 5{,}2$ ГэВ/с ($\Delta P_n / P_n \approx 3\%$). Угловой рзброс пучка ничтожно мал: $\Delta\Omega \approx 10^{-7}$ ср. Средняя точность измерения импульсов треков в камере $\Delta P/P \approx 1\%$, углов — $\Delta\Theta \approx 20'$. Такие условия эксперимента дают возможность выделить и изучать в условиях $4\pi$-геометрии отдельные каналы реакций *пр*-взаимодействий [13].

Статистический материал содержит 32 тыс. 5-лучевых звезд, в которых выделены каналы реакций $np \to pp\pi^+\pi^-\pi^-$, $np \to pp\pi^+\pi^-\pi^-\pi^0$, $np \to pn\pi^+\pi^+\pi^-\pi^-$ и $np \to \pi^-\pi^-X$. Примесь одного канала в другом не превышает 5%. В результате получено для анализа 48570 пар $\pi^-\pi^-$- и $\pi^+\pi^+$-мезонов и 79435 пар $\pi^+\pi^-$. Отметим, что в наших реакциях отсутствует комбинаторный фон для пар тождественных пионов.

## 3. Методика

Интерференционные корреляции исследуются путем изучения изменения отношения числа тождественных пар к фоновым парам в зависимости от некоторого параметра.

В наиболее простой параметризации Гольдхабера это отношение имеет релятивистски-инвариантную форму:

$$S(Q^2) = \gamma(1 + \lambda e^{-\beta^2 Q^2})(1 + \sigma Q^2), \qquad (1)$$

где $Q^2 = -(P_1 - P_2)^2 = M^2_{\pi\pi} - 4m^2_\pi$. Здесь $P_1$, $P_2$ — 4-импульсы пионов; множитель $(1 + \sigma Q^2)$ введен для компенсации возможного отклонения отношения числа пар от единицы в области вне эффекта из-за несовершенства фона.

Из самой структуры формулы (1) ясно, что при изучении корреляций вопрос нахождения адекватного фона имеет первостепенное значение. В большом числе работ в качестве фона используется распределение пар нетождественных частиц — так называемый «стандартный» фон. Очевидно, что такой фон может иметь свои динамические корреляции, отличные от динамических корреляций тождественных частиц. Поэтому, в дополнение к «стандартному» фону, используется фон, полученный перемешиванием частиц из разных событий или сгенерированный на основе реальных событий с привлечением различных моделей взаимодействия.

При конструировании фона мы исходим из требования, чтобы отношение числа тождественных пар к числу фоновых было близко к единице во всей рассматриваемой области изменения $Q^2$ вне области эффекта. С этой целью нами сконструирован фон «перемешивание с минимальным нарушением кинематических корреляций», суть которого заключается в том, что в событии сохраняются импульсы обоих мезонов, а угол между ними берется случайным образом из другого события. Вся процедура производится в общей системе центра масс реакции. Перемешивание произведено отдельно для каждой из выделенных реакций, и результаты сложены.

На рис.1 показано, для сравнения, отношение $C_2$ для пар тождественных пионов ($\pi^-\pi^-$ сложены с $\pi^+\pi^+$) и фоновых пар для случая «перемешивания с минимальным нарушением кинематических корреляций» (сплошная линия) и для обычного перемешивания (пунктирная линия) с полным разрушением кинематических корреляций (в этом методе все характеристики первого пиона берутся из одного события, а второго — из другого). Видно, что полное перемешивание дает сложное поведение фона, что затрудняет его экстраполяцию в область эффекта ($Q^2 < 0{,}05$ (ГэВ/с$^2$)$^2$).

В то же время отношение числа пар $\pi^+\pi^-$ к числу пар из фона «перемешивания с минимальным нарушением кинематических корреляций» везде (за исключением первых нескольких интервалов по $Q^2$ — район $Q^2 < 0{,}004$ (ГэВ/с$^2$)$^2$) — близко к 1. Поэтому в дальнейшем мы использовали «стандартный» фон $\pi^+\pi^-$ и фон «перемешивания с минимальным нарушением кинематических корреляций».

Разрешение по $Q^2$ в области эффекта $\sqrt{\sigma^2_p} \approx 0{,}0025$ (ГэВ/с$^2$)$^2$ значительно меньше ширины интерференционного пика и не влияет на результаты аппроксимации.

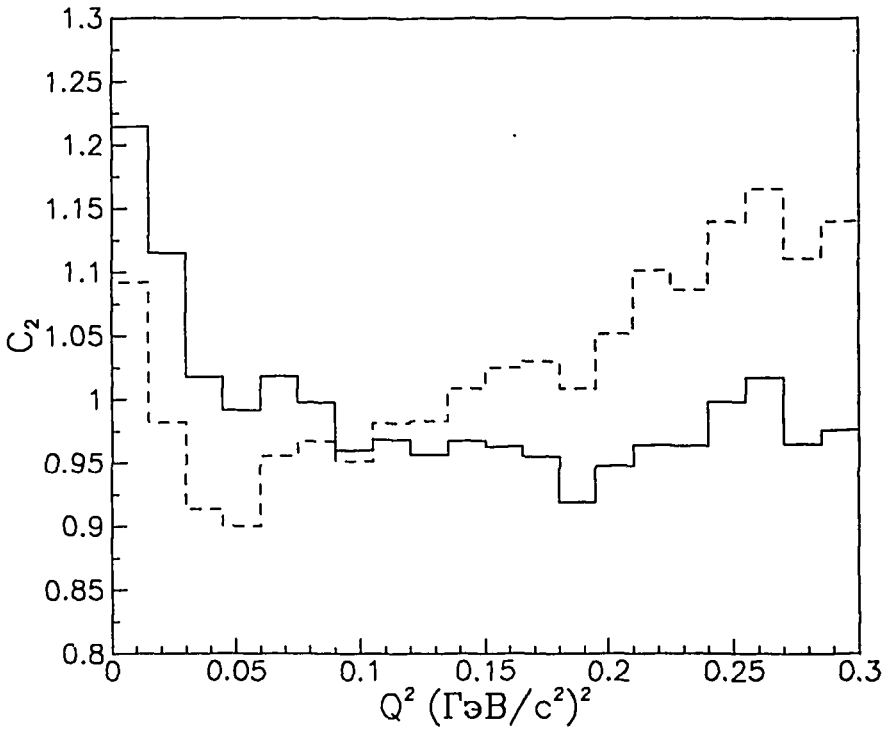


Рис.1. $C_2$ — отношение числа пар тождественных пионов к числу фоновых пар: сплошная линия — фон «перемешивание с минимальным нарушением кинематических корреляций», пунктирная — фон «перемешивание с полным нарушением кинематических корреляций»

## 4. Результаты

При аппроксимации по формуле (1) использовалась программа MINUIT. Шаг построения гистограммы при аппроксимации был выбран равным 0,001 (ГэВ/$c^2$)$^2$ (300 бинов). Результаты не меняются, в пределах ошибок, при исключении нескольких первых бинов. Параметр наклона фоновой кривой $\sigma$ в формуле (1) оказался незначимым для обоих типов фонов. На рис.2 приведено распределение $C_2$ (сумма всех каналов реакций) для шага построения 0,0075 (ГэВ/$c^2$)$^2$ вместе с аппроксимирующей кривой в случае фона «перемешивания с минимальным нарушением кинематических корреляций».

В табл.1 приведены результаты обработки с двумя видами фонов.

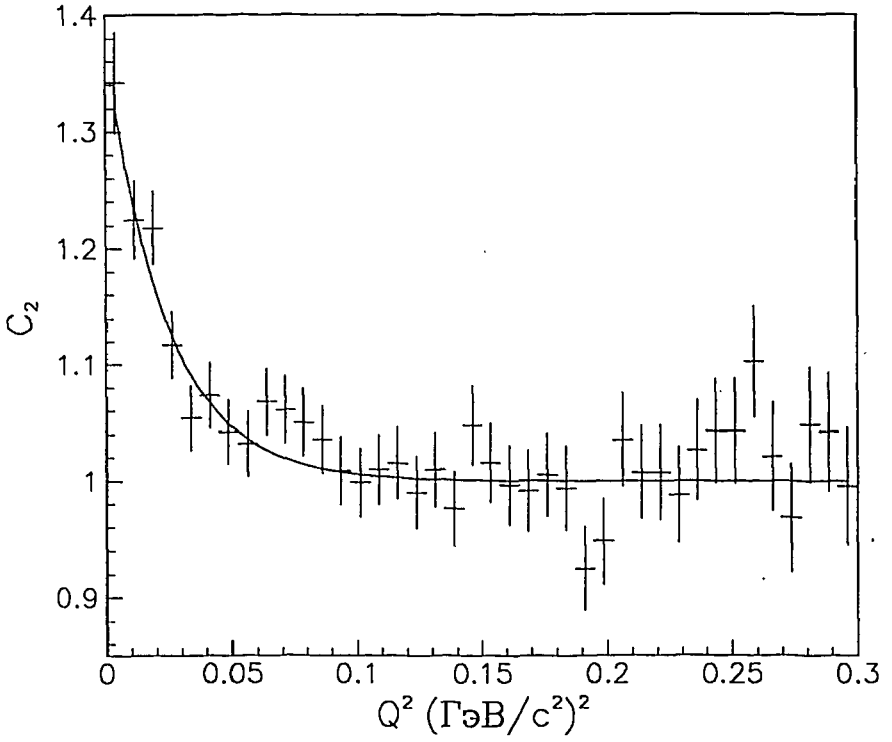


Рис.2. $C_2$ — отношение числа пар тождественных пионов к числу пар пионов, полученных методом «перемешивания с минимальным нарушением кинематических корреляций». Сплошная кривая — аппроксимирующая функция $S(Q^2)$

**Таблица**

| | β, фм | λ | $\bar{\chi}_1^2$ | $\sqrt{D_{\chi_1^2}}$ |
|---|---|---|---|---|
| $N_{\pi^\pm\pi^\pm} / N_{\text{перем. }\pi^\pm\pi^\pm}$ | 1,27 ± 0,16 | 0,37 ± 0,05 | 0,97 ± 0,08 | 1,44 ± 0,06 |
| $N_{\pi^\pm\pi^\pm} / N_{\pi^+\pi^-}$ | 1,32 ± 0,16 | 0,44 ± 0,07 | 0,98 ± 0,08 | 1,24 ± 0,06 |

В первой колонке указан вид используемого отношения, во второй — радиус области испускания пионов, в третьей — параметр λ, в четвертой — $\bar{\chi}_1^2$ описания на одну степень свободы, в пятой — корень квадратный из дисперсии $\chi^2$-распределения.

## 5. Обсуждение результатов

Представленные результаты — первые из тех, которые мы предполагаем опубликовать в ряде работ. Данная работа выполнена в инклюзивном подходе. Дальнейший анализ будет касаться, в первую очередь, влияния разного рода резонансных эффектов в обсуждаемых реакциях. В работе [14] мы сообщали о наблюдении узких маломассовых резонансов в системе $\pi^-\pi^-$ и $\pi^+\pi^-$. При этом было отмечено совпадение, в пределах ошибок, положений их центральных значений масс. Предварительный учет возможных резонансов в системе $\pi^-\pi^-$ при массах $\approx 310$, 340, 380 МэВ/$c^2$ приводит к возрастанию радиуса испускания $\pi$-мезонов примерно на 15%, что находится в пределах ошибок измерений. Этот эффект слабее сказывается при использовании «стандартного» фона.

Будет учтено также влияние изобар и других резонансов в изучаемых нами эксклюзивных реакциях.

Авторы благодарят докторов ф.-м. наук А.И.Малахова и Х.М.Чернева за помощь в проведении исследований, а также сотрудников отдела В.И.Мороза и лаборантов группы Ю.А.Трояна за помощь в получении и первичной обработке экспериментального материала.

Работа выполнена при поддержке Международного научного фонда и Правительства России (гранты NKA000 и NKA300).

## Литература

1. Goldhaber G. et al. — Phys. Rev., 1960, v.120, p.300.
2. Копылов Г.И., Подгорецкий М.И. — ЯФ, 1972, т.15, с.392; ЯФ, 1973, т.18, с.656; ЯФ, 1973, т.19, с.434.
3. Kopylov G.I. — Phys. Lett., 1974, v.50B, p.472.
4. Cocconi G. — Phys. Lett., 1974, v.49B, p.459.
5. Grassberger P. — Nucl. Phys., 1977, v.120B, p.231.
6. Gyulassy M. et al. — Phys. Rev., 1979, v.20C, p.2267.
7. Ледницки Р., Подгорецкий М.И. — ЯФ, 1979, т.30, с.837.
8. Ледницки Р., Любошиц В.Л. — ЯФ, 1982, т.35, с.1316.
9. Гришин В.Г. — УФН, 1979, т.127, вып.1, с.51.
10. Boal D.H., Gerbke C-K., Jennis B.K. — Rev. Mod. Phys., 1990, v.62, p.553.
11. Lorstäd B. — Int. J. Mod]Phys. A, 1989, v.4, p.2861.
12. Подгорецкий М.И. — ЭЧАЯ, 1989, т.20, вып.3, с.628.
13. Бешлиу и др. — ЯФ, 1986, т.43, вып.4, с.888.
14. Troyan Yu.A. et al. — Proc. of the 10 Int. Seminar on High Energy Phys. Probl. Relat. Nucl. Phys. and Quantum Chromodynamics, (Dubna, Sept., 1990), p.149; IPNO-DRE 91-18.

Рукопись поступила 13 декабря 1995 года.

УДК 539.1.074.55

# ON THE DETERMINATION OF INELASTISITY OF NUCLEUS-NUCLEUS COLLISIONS IN THE CMS EXPERIMENT

*P.I.Zarubin, N.V.Slavin*

With the aid of the HIJING generator there have been explored various options of event inelastisity characterization of nucleus-nucleus collisions in the CMS experiment at a 5·A TeV collision energy. The inelasticity estimation by the γ-quantum fraction of the total transverse energy in the very forward direction appears to be the most optimal one. Therefore, it is proposed to supplement the CMS very forward directions with electromagnetic calorimeters intended for heavy ion studies.

The investigation has been performed at the Laboratory of High Energies, JINR.

## Об определении неупругости ядро-ядерных столкновений в эксперименте CMS

*П.И.Зарубин, Н.В.Славин*

С помощью генератора HIJING исследовались различные возможности для оценки неупругости ядро-ядерных столкновений при энергии столкновения 5·А ТэВ. Оценка неупругости по компоненте гамма-квантов в направлениях малых углов представляется наиболее оптимальной. Поэтому предлагается дополнить эти направления в эксперименте CMS электромагнитными калориметрами, предназначенными для исследований с тяжелыми ионами.

Работа выполнена в Лаборатории высоких энергий ОИЯИ.

The analysis of an optimal application of the CMS experiment for high luminosity nuclear physics studies at the LHC has led to a suggestion of using beams of moderate charge nuclei ($Z < 40$) [1]. This means that an adequate luminosity level is provided to make feasible hard QCD studies in nuclear matter with observation of intermediate vector bosons, direct photons and jets [2,3,4].

In order to explore new dynamic effects in nucleus-nucleus collisions, the basic QCD process measurements in the CMS detector should be supplemented with simultaneous measurements of reaction inelasticity [5]. Therefore, it is necessary to identify appropriate CMS observables allowing to solve this problem in a practical way.

A distinctive feature of the CMS spectrometry is an optimization for observation of hard processes in proton-proton collisions. Such an approach has led to a choice of a strong magnetic field in the solenoid suppressing soft charged hadron component. As a consequence, this creates a problem for inelastisity characterization in nucleus-nucleus collision due to an effective reduction of the charged hadron contribution in the event total

**Table 1. The PYTHIA cross-section (mb) of basic subprocesses of proton-proton interactions at 5 TeV. ($f, f', \tilde{f}$ — fermions, $g$ — gluons)**

| Subprocess | Cross-section (mb) |
|---|---|
| TOTAL | 86.0 |
| $f+f' \to f+f'$ (QCD) | 19 |
| $f+\tilde{f} \to g+g$ | 0.1 |
| $f+g \to f+g$ | 15.6 |
| $g+g \to f+\tilde{f}$ | 0.5 |
| $g+g \to g+g$ | 28.2 |
| Elastic scattering | 18.1 |
| Single diffraction (XB) | 6.7 |
| Single diffraction (AX) | 6.7 |
| Double diffraction | 8.3 |

**Table 2a. The multiplicity distribution (%). HIJING, central Ca—Ca, 5·A TeV, 4T**

| | B | F | VF | UF |
|---|---|---|---|---|
| γ's | 0.9 | 5.6 | 41.5 | 19.2 |
| Hadrons | 0.0 | 0.1 | 6.8 | 25.9 |

**Table 2b. Energy distribution (%). HIJING, central Ca—Ca, 5·A TeV, 4T**

| | B | F | VF | UF |
|---|---|---|---|---|
| γ's | 0.0 | 0.3 | 6.1 | 27.7 |
| Hadrons | 0.0 | 0.0 | 3.9 | 61.9 |

**Table 2c. Transverse energy distribution (%). HIJING, central Ca—Ca, 5·A TeV, 4Y**

| | B | F | VF | UF |
|---|---|---|---|---|
| γ's | 3.0 | 7.7 | 32.1 | 12.2 |
| Hadrons | 0.0 | 0.5 | 14.5 | 30.1 |

transverse energy measured with the aid of calorimetry. Apriori, an inelasticity estimate based on γ's flux measurements seems to be more preferable.

To choose an optimal solution we have applied the widely used generator HIJING [6] for simulation of nucleus-nucleus collisions at a total energy of 5·A TeV. In the case of hard processes all resolved parton-parton scattering processes were included together with the initial and final state parton emission [7,8]. The following effects were included: multiple minijet production, nuclear shadowing of parton distribution functions and jet quenching [9] relating assumed parton energy losses with the colour screening length. The Glauber formalism was used for multiple production calculations. The nucleon density distribution was accepted in correspondance with the Woods-Saxon potential. To illustrate the importance of various subprocesses in the total proton-proton cross-section their contributions are given in Table 1.

Simulation was peformed for central collisions (zero impact parameter) of C—C (50 events), Ca—Ca (10 events), Nb—Nb (5 events) and Pb—Pb (2 events). The main single particle parameters for various generated pairs of nuclei were found to be similar. To illustrate the data we used here mainly Ca—Ca results as typical ones.

Thus, a practical way of the event characterization in the CMS consists in the measurement of the total transverse energy per event, $E_T$ which is an electromagnetic and hadron calorimetry based parameter. Our simulation has shown that an influence of the solenoid magnetic field (4T) on charged hadrons leads up to a 30% drop in $E_T$.

The CMS detector is divided by pseudorapidity on three major parts: barrel ($|\eta| < 1.6$), forward ($1.6 < |\eta| < 3$), and very forward ($3 < |\eta| < 5$), and an uncovered region — ultra forward ($5 < |\eta|$). In our analysis we have applied γ's energy cut

equal to 2 GeV and hadron one equal to 20 GeV, i.e., below lower limits of the CMS resolution curves for single particles. The gamma cut was chosen well beyond minimal ionizing particle signal. Both cuts do not seriously affect our conclusions. Tables 2*a*, *b*, and *c* show relative fractions of multiplicity, energy and transverse energy accepted by these parts. They enable us to make a conclusion about a crucial role of a very forward calorimetry for inelasticity measurements.

Figure 1 shows $\gamma$ and hadron pseudorapidiry distributions. The pseudorapidity value corresponding to the distribution maximum for $\gamma$-quantum is equal to 4.3 ($\sigma = 1.3$), i.e., most part of this distribution can be covered within the very forward calorimeter acceptance. For hadron components this value is equal to 5.6 ($\sigma = 1.1$).

The single gamma energy distribution for VF is shown in Fig.2. The mean energy and the mean transverse energy values with r.m.s. are presented in Table 3 for three major pseudorapidity regions. It can be noted that a moderate value of the VF gamma mean energy is significantly below of an operation region of presently proposed very forward calorimeter. Thus, in order to provide reliable inelasticity measurements of nucleus-nucleus collisions it appears to be necessary to include in the CMS facility a very forward electromagnetic calorimeter with suitable resolution starting from few GeV.

The multiplicity mean value for various pairs of colliding nuclei (Table 4) grows approximately linearly. Taking into account that the value of transverse energy per $\gamma$-quantum is practically the same in all

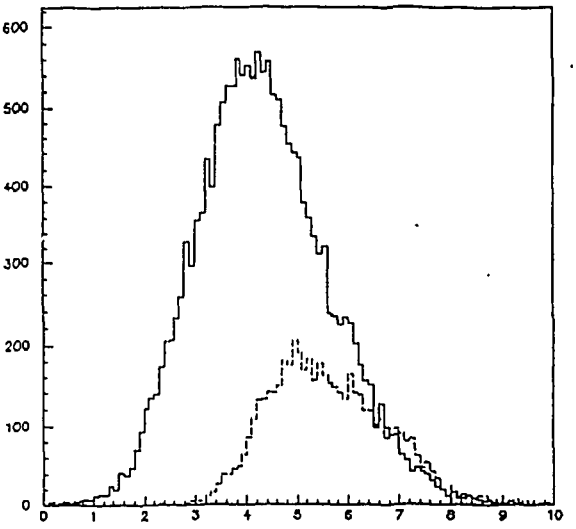


Fig.1. The effective pseudorapidity distribution of $\gamma$-guanta (upper histogram) and hadrons (lower histogram) produced in two central Pb—Pb collisions at 5·A TeV. The influence of the 4T magnetic field on charged hadrons is included. Energy cuts are mentioned in the text

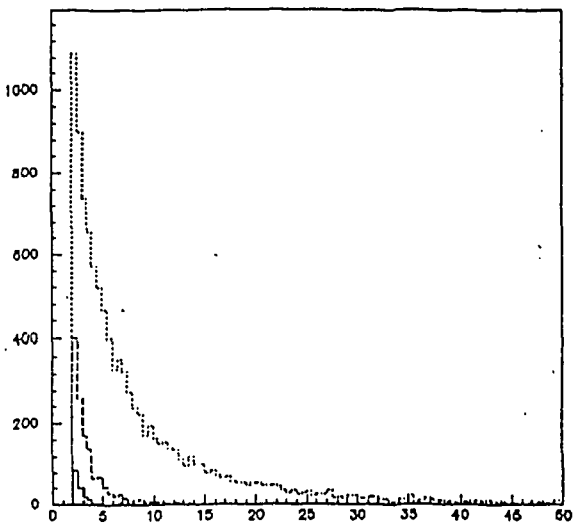


Fig.2. The $\gamma$-quantum energy distribution (GeV) in two central Pb—Pb collisions at 5·A TeV: VF — upper, F — middle, B — lower histogram, respectively. The energy cut is mentioned in the text

**Table 3. Energy and transverse energy distribution parameters (GEV) for γ's HIJING, central Ca—Ca, 5·A TeV, 4T**

| | $\langle E \rangle$ | σ | $\langle E_T \rangle$ | σ |
|---|---|---|---|---|
| B | 3.1 | 2.0 | 1.5 | 1.0 |
| F | 3.8 | 2.5 | 0.6 | 0.4 |
| VF | 8.5 | 8.0 | 0.3 | 0.3 |
| UF | 17.8 | 13.0 | 0.2 | 0.4 |

**Table 4. Energy and transverse energy distribution parameters (GEV) for γ's HIJING, central Ca—Ca, 5·A TeV, 4T**

| | p—p | | Ca—Ca | | Pb—Pb | |
|---|---|---|---|---|---|---|
| | $\langle N \rangle$ | $\sigma_N$ | $\langle N \rangle$ | $\sigma_N$ | $\langle N \rangle$ | $\sigma_N$ |
| B | 0.2 | 0.77 | 24.9 | 5.8 | 87 | — |
| F | 1.5 | 1.6 | 154.9 | 26.9 | 657 | 14 |
| VF | 17.0 | 8.0 | 1139.4 | 148.9 | 5261 | 434 |
| UF | 14.0 | 6.1 | 528.3 | 37.2 | 2646 | 51 |

the cases we are led to a linear dependence of the total $E_T$ in VF on the number of colliding nucleons.

It is imporant to mention that it is not possible to isolate single gammas from central collision on a 300 $dm^2$ area of the VF calorimeter (a shower covers of the order 1 $dm^2$). As a future step it is necessary to justify an opportunity to measure a total transverse energy by a simple summation of calorimeter cells with reasonable segmentation.

To summarize, we have carried out a simulation study aimed at a practical definition of inelasticity of nucleus-nucleus collisions in the CMS experiment case. Our major conclusion is the following: *in order to have the best estimate of an event total transverse energy the CMS very forward directions should be supplemented with an electromagnetic calorimetry intended for heavy ion studies.*

We are very grateful to our Dubna, Moscow and Sofia collaborators in the CMS experiment for stimulating and fruitful discussions, especially to Profs. L.I.Sarycheva, I.A.Golutvin, V.N.Penev, and Drs.A.I.Malakhov, V.V.Uzhinsky.

References

1. The Compact Muon Solenoid — Technical Proposal, CERN/LHCC 94-38, 15 December 1994.
2. Hilberg D., Greiner W., Kao C., Soff G. — GSI Preprint 93-57, July 1993.
3. Brandt D., Eggers K., Morsch A. — CERN AT/94-05(DI), SL/94-04(AP), LHC Note 264.
4. Zarubin P.I. — JINR NEWS Bulletin 2/95 p.15, Dubna, 1995.
5. Korotkikh V., Kodolova O., Kruglov N., Lokhtin I., Sarycheva L. — CMS Technical Note CMS TN/94-244, 20 September 1994.
6. Wang X.N., Gyuolassy M. — Phys. Rev., 1991, D44 11, p.3501.
7. Eichten E. et al. — Rev. Mod. Phys., 1984, 56, p.579.
8. Duke D.W., Owens J.F. — Phys. Rev., 1984, D30, p.501.
9. Bjorken J.D. — Preprint FNAL Pub. TH-82/59, 1982.

Received on December 13, 1995.

Редакторы: М.И.Зарубина, Э.В.Ивашкевич

Рукопись сборника поступила 12.01.96. Подписано в печать 25.01.96
Формат 70×100/16. Офсетная печать. Уч.-изд.листов 10,80
Тираж 620. Заказ 48822. Цена 7000 р.

Издательский отдел Объединенного института ядерных исследований
Дубна Московской области